Stony Brook University

Investigation of Surface Adsorption of Li^+ and Phosphate on Iron Oxyhydroxides via Solid-State NMR Spectroscopy

A Dissertation Presented

by

Jongsik Kim

To

The Graduate School

In Partial Fulfillment of the

Requirements

for the Degree of

Doctor of Philosophy

in

Chemistry

Stony Brook University

December 2009

Stony Brook University

The Graduate School

Jongsik Kim

We, the dissertation committee for the above candidate for the

Doctor of Philosophy degree, hereby recommend

acceptance of this dissertation.

Clare P. Grey – Dissertation Advisor

Professor, Department of Chemistry

Andreas Mayr - Chairperson of Defense

Professor, Department of Chemistry

Stephen A. Koch, Third Member

Professor, Department of Chemistry

Richard J. Reeder, Outside Member

Professor, Department of Geosciences, Stony Brook University

This dissertation is accepted by the Graduate School

Lawrence Martin
Dean of the Graduate School

Abstract of the Dissertation

Investigation of Surface Adsorption of Li^+ and $H_2PO_4^-$ Ions on Iron Oxyhydroxides via Solid-state NMR Spectroscopy

By

Jongsik Kim

Doctor of Philosophy

in

Chemistry

Stony Brook University

2009

Iron oxyhydroxides (α, β, and γ-FeOOHs) have been studied as effective sorbents for the removal of toxic ions from polluted water and nuclear waste streams due to their high surface areas and affinities for environmentally relevant ions. However, the adsorption mechanisms of ions on the surface of the FeOOHs at the solid/liquid interface are not clearly understood at a molecular level. Although solid-state NMR (SSNMR) is a unique and useful tool to obtain information about adsorption, iron oxyhydroxides are very challenging systems to study via SSNMR techniques due to their magnetic properties. In this work, adsorption of Li^+ and $H_2PO_4^-$ ions on iron oxyhydroxides were examined with SSNMR, opening up a new approach for characterization of ion binding on paramagnetic systems.

First, the local environments of OH groups of lepidocrocite (γ-FeOOH) were examined with ^2H MAS (magic angle spinning) NMR spectroscopy. Plausible adsorption

sites and binding modes of Li^+ on the surface of lepidocrocite were identified from the ^7Li MAS NMR results. The effects of pH and relative humidity on the local environment of the bound Li^+ ion were also investigated. Previously reported local environments of the Li^+ ion, adsorbed on the goethite surface, were reexamined. Next, local environments of OH groups in akaganeite (β-FeOOH) and adsorbed Li^+ ions on the akaganeite surface were investigated by ^2H and ^7Li MAS NMR spectroscopy, respectively. From this work, several possible Li^+ binding sites and modes were suggested as a function of pH. Finally, $H_2PO_4^-$ adsorption on the surface of goethite, akaganeite, and lepidocrocite was examined in terms of binding sites and modes via ^{31}P spin-echo mapping NMR spectroscopy as a function of pH and $H_2PO_4^-$ concentration. To interpret the acquired spectra of the $H_2PO_4^-$ adsorbed FeOOHs, several iron (pyro)phosphate compounds were examined as model systems by ^{31}P spin-echo mapping NMR spectroscopy, ^7Li and ^2H MAS NMR. The model systems include $FePO_4$ (heterosite), monoclinic $Li_3Fe_2(PO_4)_3$, rhombohedral $Li_3Fe_2(PO_4)_3$, $LiFeP_2O_7$, orthorhombic $FePO_4 \cdot 2H_2O$ (strengite), monoclinic $FePO_4 \cdot 2H_2O$ (phosphosiderite), and dehydrated phases of strengite and phosphosiderite.

Table of Contents

List of Figures

List of Tables

Acknowledgments

I would like to thank Prof. Clare P. Grey, my advisor, for her patience, encouragement, and guidance over the years. Thanks to Dr. Ulla Nielsen for showing me the ropes of experimental NMR upon joining the Grey lab. Paul Sideris, thanks for helping with my research work and for being around at the right time when I need a helper in the basement. Thanks to Dr. Sylvio Indris for fixing Chemagnetics 200 for my experiments even over the weekends. I was reassured by you whenever I had a trouble with NMR machines. Thank you to Stephen Boyd for cutting, fitting, and fixing all things in the lab and my life. Kenny Rosina for sharing his knowledge about regulations, and helping with my car woes. Thanks also to Dr. Jordi Cabana and Dr. Hailong Chen for cheering me up when I was deeply frustrated at the corner of our wet lab. Rangeet, thank you for helping me understand NMR pulse sequences and simulations and for staying around me as a generous cigarette resource. I would like also to thank my best office mates in the world, Kellie Morgan, Lucienne Buannic, Fulya Dorgan and Gunwoo Kim. I shared almost of my life in Stony Book with them. Especially, Kellie, for endless proof-reading and correcting my drafts on time. Dr. Derek Middlemiss, for proof-reading my draft and teaching me the calculation of hyperfine shifts again and again with patience. Dongli Zeng and Hua Hu, for always sparing their time to discuss everything. I would like to thank all other Grey group members, both past and present.

I appreciate Wei Li and Wenqian Xu for helping my experiments in Geoscience. I appreciate CEMS and CRC for funding my research at Stony Brook and the CEMS and CRC teams for useful discussion about my projects.

Thank you to my parents and parents in law for their endless support across the Pacific. Many thanks to Hyejin, my wife, for always being there. My daughters, Haryeong and Seryeong, I love you.

Chapter 1

Introduction

1.1 Iron Oxyhydroxides: Goethite (α-FeOOH), Akaganeite (β-FeOOH), and Lepidocrocite (γ-FeOOH)

Iron oxyhydroxides (FeOOHs) are ubiquitous in soils, rocks, and organisms and are readily synthesized in the laboratory. They have distinctive properties when used as pigments,[1] catalysts,[1, 2] semiconductors,[3, 4] electrode materials,[2, 5, 6] and precursors of magnetic recording media materials such as Fe_3O_4 and γ-Fe_2O_3.[1, 7, 8] They are particularly attractive for use as adsorbents for removing toxic ions such as Cd^{2+}, Cr^{6+}, and $As^{3+/5+}$ from polluted water and nuclear waste streams due to their strong uptake capacities, availability and low cost.[1, 9-16]

Goethite (α-FeOOH) is the most common iron oxyhydroxide in the soil. It has an orthorhombic structure with space group *Pbnm* (Z = 4), a = 9.95 Å, b = 3.01 Å, and c = 4.62 Å and is isostructural to groutite (α-MnOOH) and diaspore (α-AlOOH).[1, 17] It consists of edge-sharing FeO_6 octahedra connected to form 2 × 1 tunnels along the c axis (Figure 1.1 (a)). The tunnels have diameters of 2.5 Å across which, two hydrogen atoms are asymmetrically bonded to two oxygens.[11] These protons inside the tunnel can be exchanged with Li^+, forming goethite-type $LiFeO_2$.[18] The (101) face is the major surface plane, and the (210) face is the minor plane.[19, 20] Goethite has $Fe_3O(H)$, $Fe_2O(H)$, and $FeO(H)/FeO(H_2)$ sites on the surface. While there are slight variances in Néel temperature, T_N, of goethite, depending on structural defects and particle sizes, it is typically 393K and is therefore antiferromagnetically ordered at room temperature.[1]

Akaganeite, β-FeOOH, has been found mainly in chloride-containing environments such as hot brines and in the corrosion of iron.[1, 21, 22] Its chemical formula has been reported as $FeO_{0.833}(OH)_{1.167}Cl_{0.167}$.[23] The T_N of akaganeite is normally 290 K.[1] Akaganeite has a monoclinic unit cell with space group *I2/m* (Z = 8), a = 10.587(1) Å, b = 3.0311(2) Å, and c = 10.515(1) Å and β = 90.03(4)° (Figure 1.1 (b)),[21, 23] and is isostructural with hollandite.[1] The structure consists of double chains of edge-shared Fe-octahedra, running parallel to the pseudo fourfold symmetrical *b*-axis. The double chains share corners with adjacent chains, forming a 2 x 2 tunnel structure with a cross section of 0.5 nm^2.[1] The (100) and (001) faces represent the main surface planes.[1] The structure is stabilized by Cl^- ions, which are charge-balanced due to the extra protonation of the oxide anions associated with the iron octahedra on the inside of the tunnel structure.[24] Two different models for the extra proton sites have been proposed by Post et al.[21] and Stahl et al.[23] based on neutron powder diffraction refinements. However, definitive locations of these protons are still under debate. Post's model suggests the extra protons are placed near OH groups, forming $Fe_3O(H)$---H---Cl linkages.[21] Alternatively, Stahl' model proposes that the extra protons are placed on the inside corners of the tunnels, forming a hydrogen bonding network with the closest oxygen in the framework, i.e. Fe_3OH---O.[23] Figure 1.1 (b) shows an energetically minimized structure by Kubicki et al. with the coordinates used in Stahl's model.[25] The Kubicki model proposes that the extra protons are placed at the corner inside the tunnel structure in support of Stahl's model. However, Kubicki deviates from the Stahl model with the presence of a hydrogen bond between the extra proton and Cl^-. This is similar to Post' model. The Cl^- ions ideally occupy two thirds of the tunnel sites, but can be exchanged with other anions such as OH^-

and F^-, and partially released by washing with H_2O at neutral pH.[1, 21-23, 26] The presence of H_2O molecules in the tunnel sites not occupied by Cl anions has also been under debate for a long time.[21, 27] Akaganeite has $Fe_3O(H)$, $Fe_2O(H)$, and $FeO(H)/FeO(H_2)$ sites on its surface. The protons inside the tunnel can be replaced by Li^+ ions via an ion-exchange reaction, and by analogy with lithiated α-MnO_2, the Li^+ ions are thought to occupy vacant tetrahedral sites in the tunnels.[6, 28] In this tunnel-type $LiFeO_2$ compound, it has been assumed that the Cl^- position in the tunnel of akaganeite is filled with OH^- or O^{2-}.[6] The Li^+ ions, therefore, coordinate to one oxygen of the OH^- or O^{2-} groups at the center of the tunnel, and three oxygens of the framework structure.[6]

Lepidocrocite (γ-FeOOH) represents the second most prevalent iron oxyhydroxide in soil and is typically formed under anerobic conditions.[1] Its unit cell is orthorhombic (space group *Cmcm*, Z = 4) with unit cell parameters a = 3.072(2) Å, b = 12.516(3) Å, and c = 3.873(2) Å (Figure 1.1 (c)).[29] The mineral is isostructural with boehmite (γ-AlOOH) and is comprised of a cubic close packed array of O^{2-}/OH^- ions, with Fe^{3+} ordering to form stacked zig-zag sheets of Fe-octahedra held together by hydrogen bonding. The zig-zag sheets consist of double chains of $Fe(O, OH)_6$ octahedra which run parallel to the *c*-axis. The double chains share edges with adjacent double chains, where each chain is displaced by an octahedral unit with respect to its neighbor, forming the corrugated sheets of octahedra. These sheets are stacked perpendicular to the (100) direction and are separated by double rows of empty octahedral sites.[1] The predominant crystal plane of lepidocrocite is the (010) face, which contains doubly coordinated (Fe^{3+}-O^{2-}-Fe^{3+}) oxygen ions, and which typically accounts for 84% of the total surface area.[30] Lepidocrocite has $Fe_3O(H)$, $Fe_2O(H)$, and $FeO(H)/FeO(H_2)$ sites on

the surface and has a T_N of 77 K.[1] The protons can be replaced by Li^+ ions via an ion-exchange reaction, the Li^+ ions occupying the vacant octahedral sites between the corrugated layers to form o-$LiFeO_2$ (the "o"-indicating that this is the orthorhombic form of $LiFeO_2$).[18, 31]

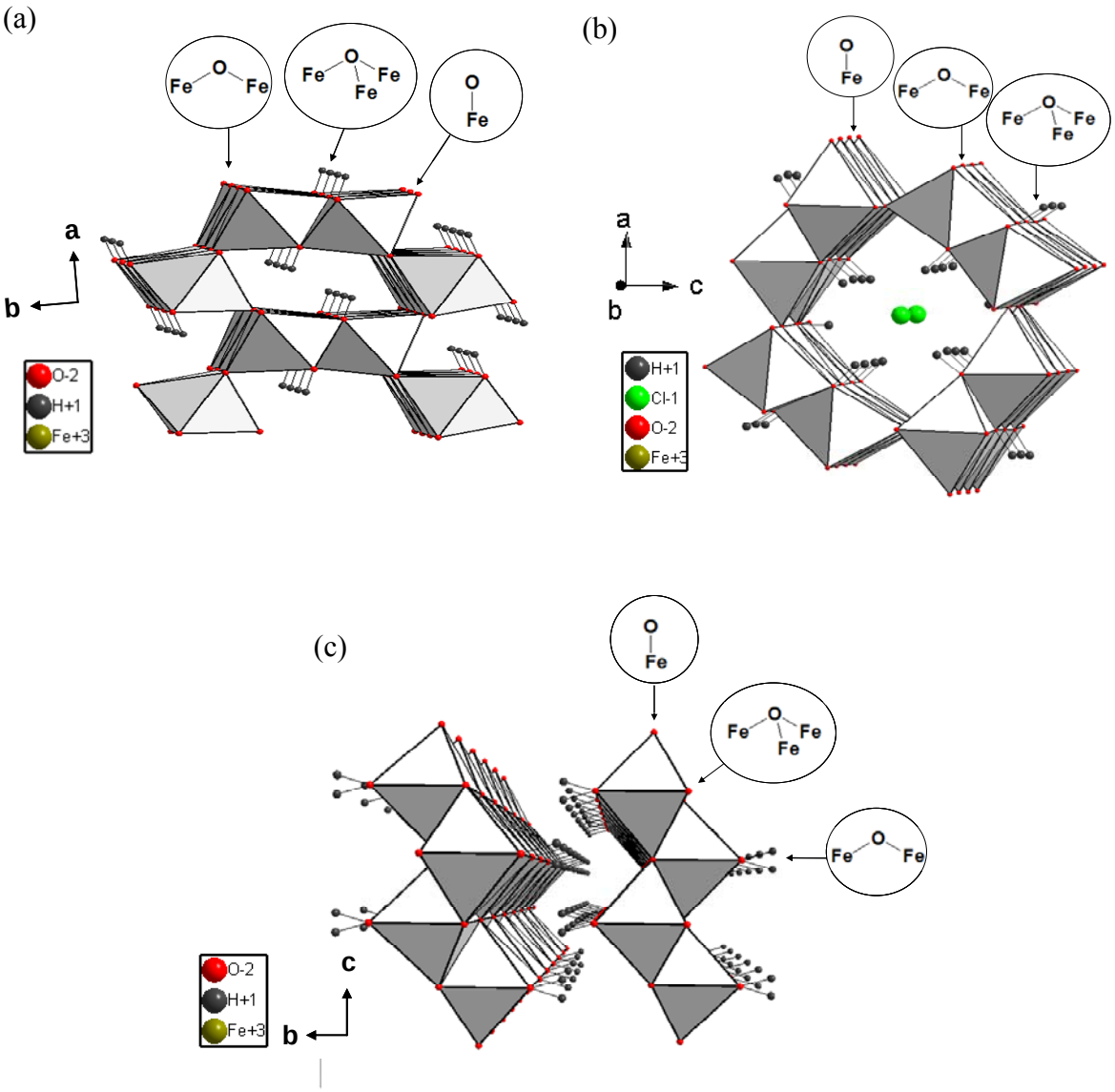

Figure 1.1. The crystal structures of (a) goethite, (b) akaganeite, and (c) lepidocrocite drawn with the reported crystallographic parameters.[1, 21, 29] Hydrogen atoms are on split positions in (b) and (c). The extra hydrogen atoms in the pocket inside the tunnel are placed at the position energetically minimized with the coordinates taken from Stahl's model in (b).[23, 25] Surface oxygen groups consist of $Fe_3O(H)$, $Fe_2O(H)$, and $FeO(H)/FeO(H_2)$. The actual number of hydrogen atoms attached to each surface oxygen group is highly pH-dependent. Cl^- is at the center of the tunnels in (b).

1.2 Adsorption of Ions on the Iron Oxyhydroxides

Adsorption is an accumulation of adsorbates, such as ions or molecules, on the surface of an adsorbent through an interaction at the interface between two components. In ecosystems, adsorption on iron oxyhydroxides influences mobility of adsorbate ions or molecules between soils and aquatic systems. Thus, the adsorption processes play a pivotal role in the transport of plant nutrients, metal ions, pollutants, etc. in groundwater. Adsorption has also been utilized in industry for processes such as water purification, flotation processes, and anticorrosion treatments.

Iron oxyhydroxides are considered to be amphoteric because their surface hydroxyl groups can be protonated or deprotonated, rendering them reactive with acids and bases (equation 1.1 and 1.2).

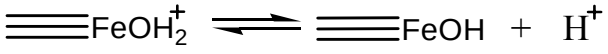

[1.1]

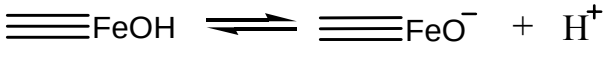

[1.2]

where ≡FeOH represents a reactive hydroxyl group bound to an Fe^{3+} ion on the surface of an iron oxyhydroxide. Therefore, the surface hydroxyl group plays a role as a functional group for surface adsorption.

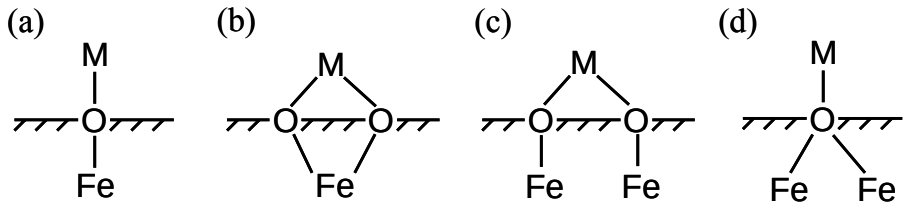

Figure 1.2. Modes of coordination of ions on the iron oxyhydroxide surface, (a) mononuclear monodentate, (b) mononuclear bidentate, (c) binuclear bidentate, and (d) binuclear monodentate.[1] M indicates an adsorbate.

Surface adsorption of ion species on an adsorbent such as an iron oxyhydroxide, as described in this work, occurs via chemisorption or physisorption. Chemisorption involves direct coordination of the adsorbing species to the surface metal (Fe^{3+}) or O^{2-} ion and results in an inner sphere complex. Thus, the interaction of a chemisorbed adsorbate with the surface occurs via the formation of a covalent bond. As a result, these adsorbates are usually strongly bound and not easily displaced. Chemisorption of cations occurs via an interaction with deprotonated surface hydroxyl groups to form various surface species such as mononuclear monodentate, mononuclear bidentate, binuclear bidentate, and binuclear monodentate complexes (Figure 1.2). Unlike cations, the adsorption of anions occurs via replacement of the surface hydroxyl groups by the adsorbing anions, resulting in several coordination modes of surface binding for phosphate, arsenate ions, etc. similar to those seen for adsorption of cations (Figure 1.2).[1] However, if ligand is monodentate e.g. F^-, only the monodentate modes in Figure 1.2 (a) are formed.[32]

Physisorption is dominated by weak attractive electrostatic forces such as Coulombic and van der Waals forces and outer sphere complexes result. Therefore, the adsorbed species generally retain their identities. Physisorbed ions can be easily replaced

by other ions. The overall charge of the adsorbent surface has a large effect on the extent of adsorption. Thus, for the physical adsorption of anions to take place, an overall positive charge of the surface is typically needed. With this adsorption mode, the adsorbing species retains their primary hydration shells, meaning that at least one water molecule is interposed between the adsorbing species and the surface functional group.

Adsorption studies on iron oxyhydroxides have been performed by three main approaches. The first one is to estimate the amount of adsorbed species on the surface. This data is useful to obtain adsorption isotherms, which are fitted to adsorption isotherm equations such as the Langmuir and the Freundlich equations. The Langmuir equation is frequently applied to anion adsorption on iron oxyhydroxides while the Freundlich equation is applied to cation adsorption. From this fitting, the equilibrium adsorption constant (K_{ads}), a measure of the affinity of the adsorbate for the adsorbent, is estimated. The adsorption data provides information about binding constants, adsorption maxima, and kinetic data but not about the mechanism of adsorption or the speciation of the surface complexes.

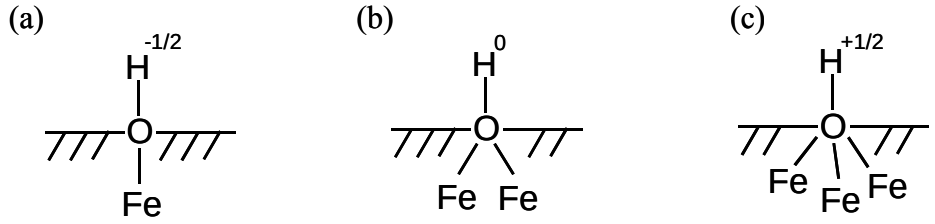

Figure 1.3. (a) Singly, (b) doubly, and (c) triply coordinated surface hydroxyl groups on the surface of an iron oxyhydroxide.[1] The number indicates the effective charge of the hydroxyl group calculated as discussed in the text.

The second method for adsorption studies is to use surface complexation models (SCMs) to describe adsorption as an interaction of an adsorbing species with well defined coordination sites such as the surface OH groups. SCMs are useful to describe the location of the adsorbed species in the electrical double layer through modeling the corresponding adsorption data. Though there are a variety of SCMs to choose from, such as the constant capacitance[33, 34] and the diffuse double layer (DDL)[35] models etc., the multisite complexation (MUSIC) model[36-38] was primarily used to analyze the adsorption of ions on the surface of iron oxyhydroxides in this work. In the MUSIC model, the hydroxyl groups can be classified as singly, doubly, and triply coordinated hydroxyl groups (Figure 1.3). The overall density and charge of the OH groups depends on the crystal structure and morphology. The MUSIC model is used to calculate a discrete acidity constant and a fractional charge for each type of surface OH group. If an Fe^{3+} ion has a sixfold coordination, a charge of +½ is assigned to each Fe-O bond (i.e. $3^{+}/6$). Therefore, the singly, doubly, and triply coordinated OH^{-} groups carry -½, 0, and +½, respectively. Thus the singly coordinated OH groups can be readily protonated, while the triply coordinated groups can be deprotonated. For example, for goethite, the singly, doubly, and triply coordinated OH groups are represented as $FeO^{-3/2}$ (or $FeOH^{-1/2}$), Fe_2OH^{0}, and $Fe_3O^{-1/2}$, respectively.[39] This information is useful to predict the surface charge curves of iron oxyhydroxides and adsorption sites in combination with other techniques[39] However, it is necessary to confirm the identity of surface speciation, which is assumed in this analysis, with experimental (preferably spectroscopic) techniques.

The third type of adsorption studies involves an investigation of the structures of the surface complexes formed through the adsorption processes by spectroscopic

techniques such as IR (Infrared spectroscopy), XPS (X-ray photoelectron spectroscopy), EXAFS (extended X-ray absorption fine structure) spectroscopy, and NMR (nuclear magnetic resonance) spectroscopy, etc. Investigating an adsorbate with spectroscopic techniques at a molecular level can provide direct information about the nature of the surface species and their mode of coordination. In addition, it can help to interpret SCM data unambiguously and directly verify the molecular assumptions used in the SCMs, for instance, only a monolayer formation at the maximum adsorption. In this work, solid-state NMR spectroscopy was mainly used to investigate the adsorption of ions on the surface of iron oxyhydroxides at a localized level.

1.3 Solid-state Nuclear Magnetic Resonance (NMR) Spectroscopy of Powder Samples

Solid-state NMR spectroscopy is a powerful technique with which to investigate the local environments and motional dynamics of both organic and inorganic materials at an atomic level. In solid-state NMR experiments, crystalline powder samples are usually measured. Because nuclei in solid samples are in a rigid motional regime, several anisotropic nuclear spin interactions such as chemical-shift anisotropy (CSA), dipolar, and quadrupolar interactions (for nuclei with spin $I > ½$) are not averaged out to zero by rapid isotropic motions of the nuclei, as they are observed to be in liquids. These anisotropic nuclear spin interactions cause line broadening for a polycrystalline sample and distinctive line shapes called powder patterns. Therefore, it is difficult to acquire high resolution solid-state NMR spectra. In order to remove these spectral broadenings

due to the anisotropic nuclear spin interactions, many solid-state NMR techniques have been developed. For example, magic angle spinning (MAS) is used to average out anisotropic interactions that can be described by second-rank tensors (e.g. CSA, dipolar, and the first order quadrupolar interactions); double rotation (DOR), dynamic angle spinning (DAS), and multi quantum MAS (MQMAS) for removing higher order interactions that are found with quadrupolar nuclei with large quadrupolar moments. These higher order interactions are not relevant to the work described here and therefore only MAS will be briefly introduced in this section.

1.3.1 Chemical-shift Anisotropy (CSA) Interactions

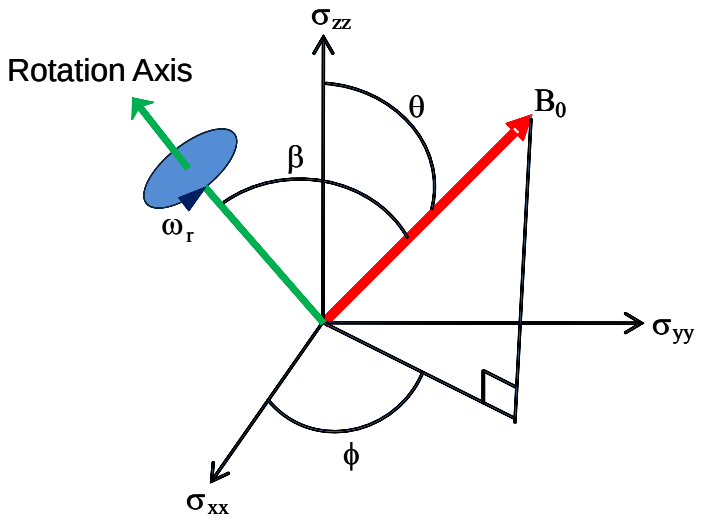

Figure 1.4. Schematic diagram of the polar angles, θ and ϕ, defining the orientation of the applied B_0 field in the principal axis (PAS) frame of the shielding or quadrupole tensor.[40] σ_{xx}, σ_{yy}, and σ_{zz} are replaced with V_{xx}, V_{yy}, and V_{zz}, respectively, for the quadrupole tensor. β defines an angle between a rotor spinning axis and the applied field B_o. ω_r denotes a spinning speed of a sample.

Even in a closed-shell (i.e. diamagnetic) material, the external magnetic field, B_0, induces circulating currents of electrons around a nucleus, resulting in a local field around the nucleus. This local field alters the effective magnetic field experienced by the nucleus, and thus the resonance frequency. This frequency shift is referred to as the chemical shift in an NMR spectrum. The chemical shift is an anisotropic interaction, producing a distinctive powder pattern in the NMR spectrum for each local environment of the nucleus (Figure 1.5).

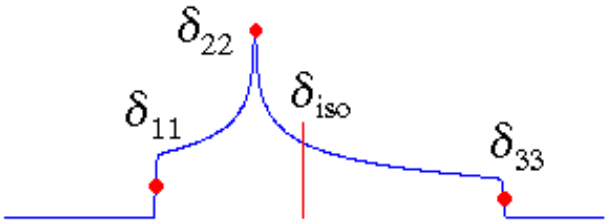

Figure 1.5. A chemical shift anisotropy powder pattern for case of a non-axially symmetric environment.[41] δ_{iso} indicates an isotropic value. The principal components are defined as $\delta_{11} > \delta_{22} > \delta_{33}$ by the common convention and in this case, $\delta_{11} \neq \delta_{22} \neq \delta_{33}$.

The Hamiltonian of the chemical-shift anisotropy interaction is:

$$H_{CS} = \gamma B_0 I_Z [\delta_{iso} + \frac{1}{2}\Delta(3\cos^2\theta - 1 + \eta\sin^2\theta\cos 2\phi)] \qquad [1.3]^{42}$$

where B_0 is the external magnetic field, I_z is the z components of the nuclear spin angular momentum operator I, γ is the gyromagnetic ratio, δ_{iso} is the isotropic value (equation [1.4]), Δ is the chemical shift anisotropy (equation [1.5]), and η is the asymmetry (equation [1.6]). θ and ϕ are defined in Figure 1.4.

$$\delta_{iso} = \frac{1}{3}(\delta_{11} + \delta_{22} + \delta_{33})$$

[1.4][42]

where the principal components are defined as $\delta_{11} > \delta_{22} > \delta_{33}$ by the common convention.

$$\Delta = \delta_{11} - \delta_{iso}$$

[1.5][42]

$$\eta = \frac{\delta_{33} - \delta_{22}}{\Delta}$$

[1.6][42]

For an axially symmetric system, $\eta = 0$ on the basis of equation [1.6]. The CSA can be removed by the magic angle spinning.

1.3.2 Dipolar Interactions

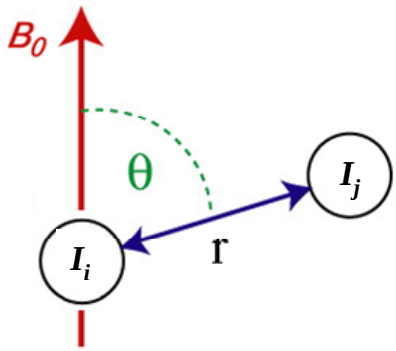

Figure 1.6. A schematic diagram of dipolar interactions. θ is the angle between the bond vector of two nuclei, I_i and I_j and the direction of the external magnetic field, B_o. r is the distance between two coupled nuclei.

The dipolar interaction results from interactions of one nuclear spin with a local magnetic field generated by the surrounding nuclear spin(s) through space (Figure 1.6). This anisotropic interaction is one of the major causes of line broadening in solid-state NMR spectra. There are three different types of dipolar coupling, i.e. heteronuclear and homonuclear dipolar coupling, and the coupling between the nuclear and electronic spins of paramagnetic ions which is very important in paramagnetic materials. Herein, heteronuclear and homonuclear dipolar couplings will be briefly introduced. Coupling between nuclear and electronic spins of paramagnetic ions will be described in detail in section 1.3.7. In the rotating frame, the Hamiltonian of the homonuclear dipolar coupling may be written as[41, 42]:

$$H_D^{i=j} = -d \cdot \frac{1}{2}(3\cos^2\theta_{ij} - 1)[3I_{iz}I_{jz} - I_i \cdot I_j] \qquad [1.7]^{46}$$

$$I_i \cdot I_j = I_{ix} I_{jx} + I_{iy} I_{jy} + I_{iz} I_{jz}$$

[1.8][46]

$$d = \hbar \left(\frac{\mu_0}{4\pi} \right) \frac{1}{r_{ij}^3} \gamma_i \gamma_j$$

[1.9][46]

The Hamiltonian of the heteronuclear case is:

$$H_D^{i \neq j} = -d(3\cos^2 \theta_{ij} - 1) I_{iz} I_{jz}$$

[1.10][46]

where γ is the magnetogyric ratio of a nuclear spin and I is the nuclear spin vector of a spin. I_{ix}, I_{iy}, and I_{iz} are x, y, and z components of the nuclear spin angular momentum operator I of a spin i. The same definition is applied to a spin j.

The strength of the dipolar interaction depends on the relative orientation of the I_i-I_j vector in the applied field, B_0, and the distance between interacting nuclei (r) (Figure 1.6). It is normally quantified via the dipolar coupling constant, d. These dipolar interactions can be reduced or averaged out to zero by magic angle spinning (MAS) due to their orientation dependence. For the heteronuclear dipolar interaction, MAS breaks up line width governed by factors other than residual dipolar coupling into spinning side

bands. However, for the homonuclear dipolar interaction, the MAS rate must be larger than the dipolar-coupling line width for significant line narrowing.

1.3.3 Quadrupolar Interactions

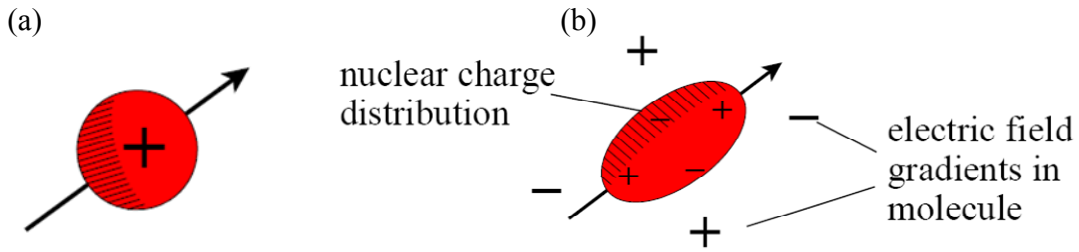

Figure 1.7. A charge distribution of (a) spin-½ and (b) quadrupolar nuclei.

Nuclei with spin I > ½ are defined as quadrupolar nuclei. They have a non-spherical nuclear charge distribution, giving rise to a quadrupole moment (Figure 1.7 (b)). This is in contrast to spin-½ nuclei, which have a spherical nuclear charge distribution (Figure 1.7 (a)). Thus, quadrupolar nuclei possess a nuclear electric quadrupole moment in addition to the magnetic dipole moment also possessed by spin-½ nuclei. The electric quadrupole moment interacts with an electric field gradient present around the nucleus, and affects the nuclear spin energy levels. That is to say, the quadrupolar nuclei have a quadrupolar interaction in addition to the chemical shift anisotropy and dipolar coupling that are found for a nucleus with I = ½. If the nuclei are at a site of lower symmetry than cubic, octahedral, and tetrahedral, the magnitude of the quadrupolar interaction becomes non-zero and line broadening is seen in the solid-state NMR spectra.

When quadrupolar interaction is involved in the nuclear spin system, the Hamiltonian of the system may be written as:

$$H = H_0 + H_Q$$

[1.11][40]

where H_0 (= $\omega_0 \hat{I}_z$) and H_Q are the Hamiltonians of the Zeeman and quadrupole interactions, respectively. The quadrupolar interaction affects the energies of the Zeeman states (Figure 1.8). The interaction between a nuclear electric quadruple moment and an electric field gradient, V, is described as in the PAS of V:

$$H_Q = \frac{eQ}{2I(2I-1)\hbar} I_i \cdot V \cdot I_i$$

[1.12][42]

where V is the electric field gradient tensor at a nucleus i, I_i is the nuclear spin vector of spin i, eQ is the electric quadrupole moment, and e is the charge of the electron.

The size of the quadrupolar interaction is given by the quadrupole coupling constant, C_Q:

$$C_Q = \frac{e^2 qQ}{\hbar}$$

[1.13][42]

where eq (= V_{zz}) is the anisotropy of the electric field gradient tensor (Figure 1.4).

The asymmetry of the quadrupole interaction is given by the asymmetry parameter, η in the principal axis frame (Figure 1.4):

$$\eta = \frac{V_{xx} - V_{yy}}{V_{zz}}$$

[1.14][42]

where V_{xx}, V_{yy}, and V_{zz} are the principal axes of the quadrupole tensor (Figure 1.4). The quadrupolar interaction can be re-written as a sum of the first and second order interactions:

$$H_Q = H_Q^{(1)} + H_Q^{(2)}$$

[1. 15][40, 42]

where $H_Q^{(1)}$ and $H_Q^{(2)}$ are the first and second quadrupolar interactions, respectively. The first order quadrupolar interaction is given as in the laboratory frame (x, y, and z):

$$H_Q^{(1)} = 1/2Q'(\theta,\phi)\{I_z^2 - I(I+1)/3\}$$

[1. 16][40, 42]

where ω_Q is quadrupole frequency, θ and φ are polar angles that define the orientation of the principal axis frame of the quadrupole tensor defined by V_{xx}, V_{yy}, and V_{zz} (Figure 1.4). Quadrupolar splitting (Q′) is written as:

$$Q'(\theta,\phi) = (\omega_Q/2)[(3\cos^2\theta - 1) - \eta_Q \sin^2\theta \cos 2\phi]$$

[1. 17][40, 42]

$$\omega_Q = \frac{3e^2qQ}{2I(2I-1)\hbar}$$

[1. 18][40, 42]

The Hamiltonian of the second order quadrupolar interaction is:

$$H_Q^{(2)} = \frac{1}{6}\omega_Q[3I_Z^2 - I(I+1) + \eta(I_x^2 + I_y^2)]$$

[1. 19][40, 42]

The second order energy corrections to the energies of the Zeeman levels from quadrupolar interaction can be described by perturbation theory like this:

$$\omega_Q^{(2)} = -\frac{\omega_Q^2}{16\omega_0}[I(I+1) - \frac{3}{4}](1-\cos^2\theta)(9\cos^2\theta - 1)$$

[1. 20][40, 42]

where ω_0 is the Larmor frequency.

The effects of the first and second order quadrupolar interactions on the energy levels of spin-3/2 and spin-1 nuclei are shown in Figure 1.18. For nuclei with I = 3/2, the first order quadrupolar interaction does not affect central transition (+½ → –½), but changes satellite transition by Q′ in equation [1.17] (Figure 1.18 (a)). However, the second order quadrupolar interaction causes a change in the frequency of the central transition by $\omega_Q^{(2)}$ in equation [1.20], but the size is much smaller than that of the first order quadrupolar interaction. For ^{7}Li (I = 3/2) here, the second order quadrupolar effect

is not observed in a NMR spectrum due to its small quadrupolar moment. Equation [1.20] shows that the size of the second order quadrupolar interaction depends inversely on a magnetic field strength (B_0). For spin-1 nucleus such as ^{2}H, ^{6}Li, and ^{14}N, the first order quadrupolar interaction affects the -1 → 0 and the 0 → +1 transition to be different in energy by Q′ in equation [1.17] like case of a spin-3/2 nucleus. For ^{2}H and ^{6}Li nuclei studied in this work, the size of the second order quadrupolar interaction is small due to their small quadrupolar moments and can be ignored in Figure 1.8 (b).

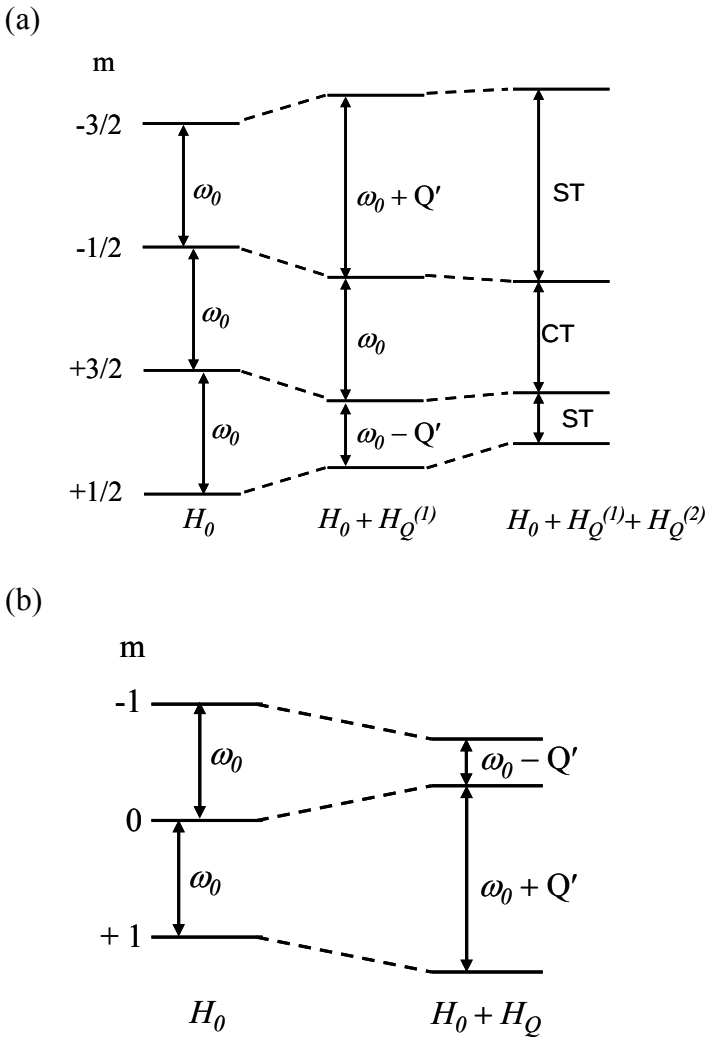

Figure 1.8 The effect of the Zeeman and quadrupolar interactions on the energy level diagrams of (a) spin-3/2 and (b) spin-1 nuclei.[40, 41] The effect of the second-order quadrupolar interaction is omitted due to its small magnitude.

1.3.4 Magic angle spinning (MAS)

Magic angle spinning (MAS) is one of the most widely used NMR techniques to narrow the broad line width due to the anisotropic nuclear spin interactions described by second rank tensors and to obtain high-resolution solid-state NMR spectra. In MAS, a sample is rapidly spun about an axis inclined at $\beta = 54.74°$ (referred to as the magic angle) relative to the external applied magnetic field B_o (Figure 1.4). If the spinning

frequency at this angle is much larger than the strength of the anisotropic interactions, the anisotropic interactions, which have the orientation dependence of $3\cos^2\theta - 1$, can be removed or partially averaged. Thus, the anisotropic tensors are averaged to their isotropic value. However, in practice, the spinning rate is not fast enough to completely average out the anisotropy, and an isotropic peak is usually accompanied with a series of peaks, referred to as spinning sidebands, spaced at integer multiples of the spinning rate from the isotropic peak in a solid-state NMR spectrum. The shift of the isotropic resonance is not affected by a spinning rate, providing an easy method to identify the isotropic chemical shift.

1.3.5 Spin-echo Mapping NMR Spectroscopy

When the line width of NMR resonance is comparable to or larger than the exciting radio-frequency (RF) field, it is hard to acquire the total NMR spectrum by applying a single irradiation pulse at a given frequency. Particularly in Fe^{3+}-containing paramagnetic materials, the NMR signals are significantly broadened due to the interactions between the unpaired electronic spins of an Fe^{3+} ion and the nuclear spin under observation. In addition, many systems investigated in this thesis are disordered and so multiple local environments are often present, resulting in additional line broadening. To circumvent this problem, the spin-echo mapping technique has been successfully used in NMR experiments of metallic or magnetic materials.[43-47]

The spin-echo mapping technique consists of recording a series of spectra using the spin echo pulse sequence, $90°_x$-τ-$180°_y$-τ-acquire, at different carrier frequencies.

The total NMR signal is then obtained by summing up all the individual spectra. The irradiation frequency is varied with a step size determined on the basis of the RF field strength (ω_1). A step size that is comparable to or less than ω_1 or $\omega_1/2$ is normally used.

In this work, ^{2}H, $^{6,7}Li$, and ^{31}P nuclei were mainly used to probe the local environments of OH groups in iron oxyhydroxides and adsorbed ions on their surfaces. The brief introduction of those nuclei and the quadrupolar effect of the ^{2}H nucleus on a NMR spectrum will be described more in the following section.

1.3.6 ^{31}P (I = 1/2) and ^{7}Li (I = 3/2) Solid-State NMR Spectroscopy

^{31}P is a spin-1/2 nucleus with 100 % natural abundance and has a resonance frequency of 81.0045 MHz at 4.7 T with the gyromagnetic ratio of 10.84015×10^{7} rad T^{-1} s^{-1}. Theses factors make it readily observable. Its chemical shifts are usually referenced to 85 % H_3PO_4. CSA can be observed in a NMR spectrum and its size depends on the structural environments.

^{7}Li (I = 3/2), which is a quadrupolar nucleus, is commonly used due to its high natural abundance (92.5 %) and favorable receptivity. However, the quadrupole moment (-4.0×10^{-30} m^2 A) and homonuclear dipolar interactions often cause line broadening in a solid-state NMR spectrum. The gyromagnetic ratio of ^{7}Li is 10.39730×10^{7} rad T^{-1} s^{-1}. It has a resonance frequency of 77.7662 MHz at 4.7 T.[48] Its chemical shifts are commonly measured with respect to aqueous LiCl.

1.3.7 ^{6}Li and ^{2}H (I = 1) NMR Spectroscopy

The quadrupolar nucleus ^{6}Li (spin = 1) has a much lower natural abundance (7.5 %) and the smaller Larmor frequency of 29.44691 MHz at 4.7 T compared to ^{7}Li nucleus. However, its small quadrupolar moment (-8×10^{-32} m^2 A) and homonuclear dipolar interactions give resonance lines with smaller line width in solid-state NMR spectra. Thus, ^{6}Li can be a preferable nucleus to resolve two close resonances when they are not resolved with ^{7}Li.

Deuterium (spin = 1) has a low natural abundance less than 0.1 %. The Larmor frequency of ^{2}H is 30.7176 MHz at 4.7 T. The relatively small quadrupole moment (3×10^{-31} m^2 A) results in a first-order quadrupolar coupling constant of the order of 100-300 kHz, which is ~10 times lower than ^{14}N (I = 1) for many environments, including OH and CH bonds.[41] Second-order quadrupolar effects are only of the order of 3 kHz in a 2.3-T magnetic field, and are rarely observed in ^{2}H solid-state NMR spectra. Here, since the quadrupolar interactions of ^{6}Li can be ignored due to its very small quadrupolar moment, the effects of quadrupolar interactions of ^{2}H nucleus on solid-state NMR spectra will mainly be introduced below.

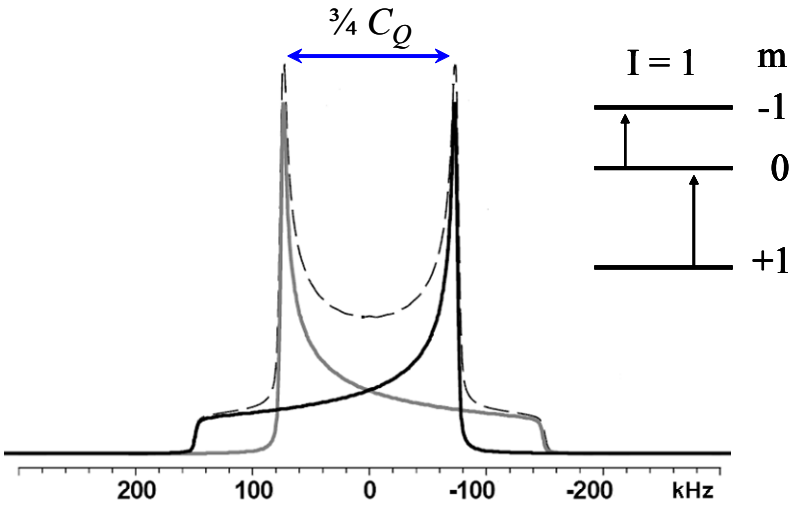

Figure 1.9. The form of a ^{2}H quadrupolar powder pattern. The doublet nature of the pattern is due to there being two allowed spin transitions.[42]

In ^{2}H NMR spectra, the two possible transitions (m = +1 → 0 and m = 0 → –1) for a spin-1 nucleus give rise to mirror image line shapes and an overall pattern referred to as a Pake-doublet, that is generally a characteristic of a rigid deuterium atom (e.g. OH) (Figure 1.9). The powder pattern line shapes are sensitive to molecular motions with correlation times of the order of 10^{-4}-10^{-6} Hz. This dynamic range is coincidentally correspond to a range of motional correlation times often found in solids in the temperature range of -150–250 °C, which is accessible by most commercial NMR spectrometers. Therefore, ^{2}H NMR can be utilized to extract molecular level information of solid compounds such as the hydrogen bonding distances and motional dynamics primarily via line shape analysis. The quadrupolar splitting, i.e. the splitting between the 2 major discontinuities or "horns" is equal to ¾ C_Q, where C_Q is quadrupolar coupling constant. From the measured quadrupolar coupling constant (C_Q), it is possible to calculate the distance of the (O-D---O) hydrogen bond via the following equation[49]:

$$C_Q\ (kHz) = 442.7 - 4882/R^3$$

[1.21][49, 50]

where "R" represents the O-O distance in Å.

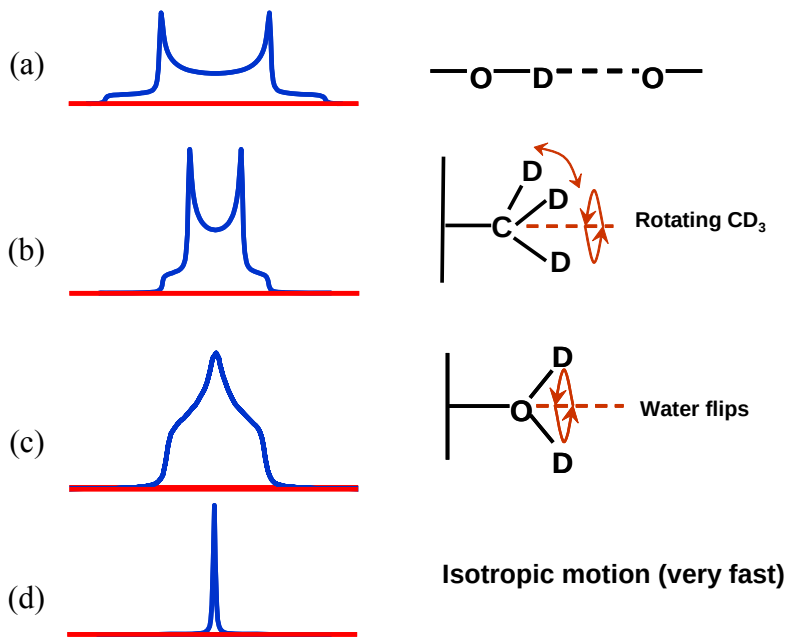

Figure 1.10. Simulated line shapes of ^2H solid-state NMR spectra for a (a) rigid -OD group, (b) rotating methyl (-CD_3) group, and (c) D_2O undergoing 180° flips.[40]

As the quadrupolar interaction depends on the molecular orientation with respect to the external magnetic field (B_0), a reorientation of the molecule reduces the width and shape of the ^2H NMR spectrum (Figure 1.10). When a –OD group is bound rigidly through a hydrogen bond, the typical Pake-doublet line shape is observed (Figure 1.10 (a)). When a rotational motion about a certain axis is involved, the line width and quadrupolar splitting of a ^2H NMR spectrum changes dramatically depending on the extent and type of the angular motion. For example, the line width and quadrupolar splitting of the spectrum decrease for a rotating methyl group (-CD_3) (Figure 1.10 (b)). The coalescence

of "horns" is observed for a D_2O molecule undergoing 180° flips (Figure 1.10 (c)). Isotropic motion involving complete averaging about three perpendicular axes, results in a single sharp isotropic resonance (Figure 1.10 (d)). Furthermore, motion on a time scale of the evolution period of the spin and quadrupolar-echo sequences (typically 20-200 μs) can cause changes in the line shape and a tremendous loss of signal intensity.[51]

1.3.8 Solid-State NMR Spectra of Paramagnetic Systems

Paramagnetic materials with unpaired electronic spins in f, d, p, and s-block orbitals show distinct properties in terms of their shifts, line broadening, and line shapes in NMR spectra. The NMR resonances of paramagnetic materials have much larger shifts and line broadening than those of diamagnetic materials. Their line shapes resemble those caused by chemical shift anisotropy (CSA). All these unique properties of NMR spectra in paramagnetic systems are caused by through-bond (Fermi-contact) or through-space (dipolar) interactions between a nuclear spin under observation and unpaired electronic spins of metal ions. These interactions are much larger than any other interactions such as CSA, dipolar, and quadrupolar interactions and can dominate the spectra of paramagnetic materials.

In the following section, Fermi-contact interaction and dipolar coupling in paramagnetic materials will be discussed in more detail.

1.3.8.1 Fermi-Contact (Hyperfine Shift) Interaction

Isotropic shifts in NMR spectra of paramagnetic materials arise from diamagnetic, Fermi-contact, and pseudo-contact shifts. The contributions of diamagnetic and pseudo-contact shifts (which can be significant in a system with an anisotropic magnetic moment) to isotropic shifts are negligible relative to Fermi-contact shift in Fe^{3+}-containing systems (high spin d^5), which have an isotropic magnetic moment. Therefore, the observed isotropic shift is dominated by Fermi-contact shift interaction.

The Fermi-contact interaction in Fe^{3+}-containing systems is a result of transferring the unpaired electron spin density of the d orbital of Fe^{3+} atom to s orbital of an nucleus under observation. The Hamiltonian for the Fermi-contact interaction is:

$$H_{cs} = -\frac{A}{h}\frac{B_0}{\mu_0 g N_0 \mu_B}\chi_M$$

[1.22][52]

$$A/h = g\mu_B\gamma_N\rho(r=0)\mu_0/3S$$

[1.23][52]

where A is the hyperfine coupling constant, h the Planck constant, B_0 the field strength, μ_0 permeability, g the electron g factor, N_0 Avogadro's number, μ_B the Bohr magneton, χ_M the molar susceptibility of the material, γ_N the gyromagnetic ratio for the nucleus under observation, $\rho(r = 0)$ the electron spin density at the nucleus, and S the total spin angular momentum quantum number. The size of the hyperfine (or Fermi-contact) shift

is directly proportional to two terms, the time-averaged value of the magnetic moment of the paramagnetic ion[52], $\overline{\mu}_e$, (which is proportional to the molar susceptibility of the material, χ_M) and the hyperfine coupling constant, A. χ_M depends on the number of unpaired electrons and the nature of any residual couplings between magnetic ions in the paramagnetic state, while the size of A is determined by the number of H-O-Fe bonds and nature of the overlap between the H s, O 2s and 2p, and Fe 3d (and 4s, 4p) orbitals that contribute to these bonds.[52, 53] (H can be replaced with ^{2}H, Li or P in this work.)

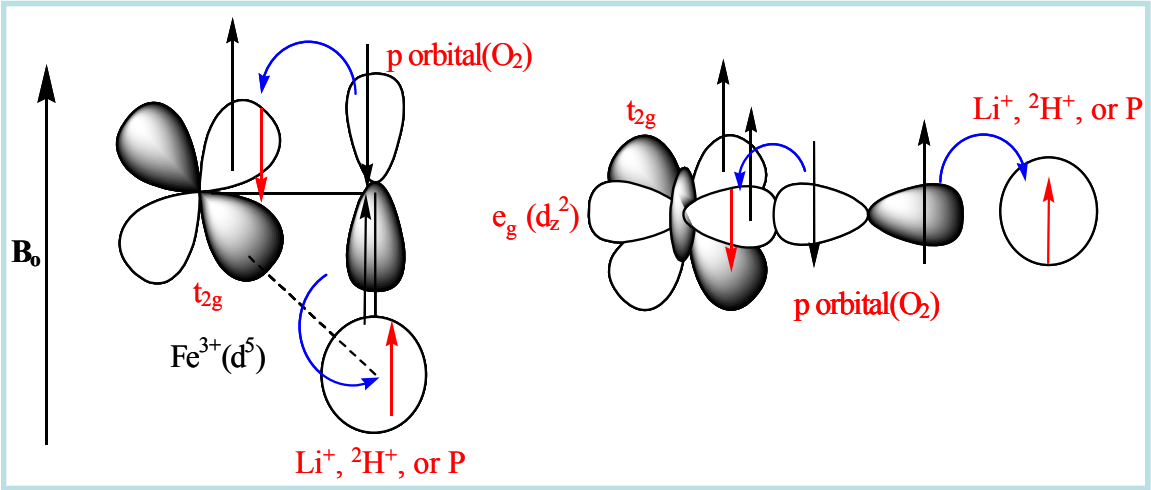

Figure 1.11. The Fermi-contact interaction for Fe^{3+} which has half-filled t_{2g} and e_g orbitals. Red arrows show the directions of transfer to and from the orbitals of the paramagnetic ions to the overlapping orbitals on adjacent atoms. The black colored arrows depict the magnetic moments of the electrons in the t_{2g}, e_g and p orbitals.

Figure 1.11 depicts the mechanism of the Fermi-contact interaction which can be used to predict the extent and sign of the shift. As shown in the Hamiltonian, only the electron density transferred from the metal ion to the s orbitals of the nucleus are considered. In the Fe^{3+} (d^5) environments, both the e_g and t_{2g} orbitals are already half-filled. At a bond angle of 90° between the Fe^{3+} ion and the cationic species via oxygen

orbital, i.e. a Fe-O-X interaction, the filled oxygen orbital should partially transfer negative spin density to the half-filled t_{2g} orbital, leaving positive spin density to be transferred to the empty s orbital of observed nucleus. The e_g orbital of Fe^{3+} has positive spin density so that, at a bonding angle of 180°, a partial transfer of negative spin density again occurs from the intervening oxygen orbital but now to the e_g orbital. This will result in the concurrent partial transfer of positive spin density from the oxygen orbital to the s orbitals of the observed nucleus, again causing a positive hyperfine shift in the NMR spectrum. The Fermi-contact shift appears to be cumulative based on a number of experimental studies[54-56], so that the observed isotropic shift is a sum of shifts induced by each contributing paramagnet transferring electronic spin density. Therefore, the Fermi-contact shift can provide useful information about the local environments around the nucleus, including the number of paramagnets coordinated to the observed nucleus.

1.3.8.2 Dipolar coupling

In paramagnetic materials, the dipolar interaction involves coupling between the observed nuclear spin and the time-averaged magnetic moment of the unpaired electronic spins. The Hamiltonian for this interaction is given by:

$$H_{en} = \frac{\mu_0}{4\pi} \bar{\mu}_e \tilde{D}_{en} \mu_N$$

[1.24][52]

where μ_0 is the permeability, $\overline{\mu}_e$ the thermally-averaged magnetic moment of the electrons, $\widetilde{D}_{en}$ dipolar coupling tensor between the unpaired electronic spin and nucleus, and μ_N the nuclear magnetic moment. This dipolar interaction is a second-rank tensor, which can normally be averaged by MAS. However, the magnitude of this interaction is often larger than MAS and is therefore not completely averaged out, resulting in a spinning sideband manifold resembling the CSA line shape. The spinning sideband manifolds have characteristic shapes depending on the local environments of the nucleus under observation and therefore can provide useful structural information concerning the local environment surrounding the observed nucleus.[52, 57]

1.4 Systems Studied / Aims of Research

The element specificity of solid-state NMR spectroscopy makes it an ideal technique to study the surface adsorption of small ions at a molecular level because it allows one to probe the sorbed ions directly and can provide information about the local environments surrounding the nucleus of interest. However, it is very challenging to study paramagnetic (Fe^{3+}-containing) systems such as iron oxyhydroxides due to the presence of unpaired electron spins on the Fe^{3+} ions, which cause large line broadening and the Fermi-contact shifts in solid-state NMR spectra. In addition, the shifts are strongly affected by magnetic properties such as magnetic susceptibility of the systems. Therefore, our primary aim in this work is to establish protocols to acquire high resolution NMR spectra of Fe^{3+}-containing paramagnetic systems and to interpret the

NMR spectra with consideration of magnetic properties of the systems. The methodology used to analyze the Fermi-contact interaction in this study is based on two assumptions.[52] One is that only the first coordination sphere significantly contributes to the observed hyperfine shift. The other assumption is that the observed shift should obey the Curie-Weiss law[1], $\chi = C/(T-\Theta)$, for temperatures where the magnetic properties follow this dependence. (C is the Curie constant and Θ is a temperature that characterizes the size of the interactions between magnetic particles.) Therefore, Θ and the experimentally measured χ or μ_{eff} were taken accounted as a scaling factor of the magnitude of the Fermi-contact shift to compare the shifts of different compounds each other. Whether the shift deviates from the Curie-Weiss law or not can be tested by variable-temperature (VT) NMR experiments. However, in order to confirm this hypothesis, more experimental data is required on several compounds with detailed structural information such as bond angles and lengths. This contribution shows how solid-state NMR technique can be applied to unveil adsorption mechanisms of the ions on the surface of the iron oxyhydroxides, especially in terms of binding sites, adsorption modes and the most reactive adsorption surface planes.

In Chapter 2, motional dynamics of OH groups and binding modes and sites of Li^+ ion on lepidocrocite were investigated with ^2H and ^7Li MAS NMR at a localized level. In addition, the effects of pH and relative humidity on the bound Li^+ ion were studied. The previously reported ^7Li MAS spectra were re-analyzed based on the ^7Li MAS NMR data of lepidocrocite. In Chapter 3, OH groups of akaganeite and binding sites and modes were examined by ^2H and ^7Li MAS NMR. pH effects on the bound Li^+ ion on akaganeite were also studied. In Chapter 4, adsorption of phosphate ions on goethite,

akaganeite, and lepidocrocite as a function of pH and phosphate concentrations was investigated with ^{31}P spin-echo mapping NMR. Based on the obtained NMR data, the binding mode and sites of phosphate on those iron oxyhydroxides were proposed. In Chapter 5, iron phosphate and pyrophosphate compounds were studied with ^{2}H and ^{7}Li MAS NMR and ^{31}P spin-mapping NMR and a periodic B3LYP hybrid density functional theory calculations. These results were used to interpret the ^{31}P NMR data in Chapter 4.

Chapter 2

Local Environments and Lithium Adsorption on the Iron oxyhydroxides Lepidocrocite (γ-FeOOH) and Goethite (α-FeOOH): a ^{2}H and ^{7}Li Solid-state MAS NMR Study

^{2}H and ^{7}Li MAS NMR spectroscopy techniques were applied to study the local surface and bulk environments of iron oxyhydroxide lepidocrocite (γ-FeOOH). ^{2}H VT (variable-temperature) MAS NMR experiments were performed, showing the presence of short-range, strong antiferromagnetic correlations, even at temperatures above the Néel temperature, T_N, 77K. The formation of a Li^+ inner-sphere complex on the surface of lepidocrocite was confirmed by the observation of a signal with a large ^{7}Li hyperfine shift in the ^{7}Li MAS NMR spectrum. The effect of pH and relative humidity (RH) on the relative concentrations of Li^+ inner and outer sphere complexes was then explored, the concentration of the inner sphere complex increasing rapidly above the point of zero charge and with decreasing RH. Possible local environments of the adsorbed Li^+ were identified by comparison with other layer-structured iron oxides such as γ-$LiFeO_2$ and o-$LiFeO_2$. Li^+ positions of Li^+-sorbed and exchanged goethite were re-analyzed based on the correlations between Li hyperfine shifts and Li local structures and two different binding sites were proposed, the second binding site only becoming available at higher pH.

This chapter is adapted from a paper that is published in Journal of American Chemical Society.[58]

2.1 Introduction

We recently reported a ^{2}H and ^{6}Li MAS NMR study of Li^{+}-sorbed and deuterated goethite (α-FeOOH).[50, 59] The Néel temperature, T_N, of goethite is above 120 °C and it is therefore antiferromagnetically ordered at room temperature. As a result, the ^{2}H MAS NMR spectrum of deuterated goethite was featureless and broad at room temperature, but a well resolved ^{2}H NMR spectra could be obtained by acquiring the spectra above T_N. Similarly, well resolved spectra could also be obtained at ambient temperatures by either doping the material with Al^{3+} or by synthesizing nanoparticles, both methods leading to a reduction of T_N and to paramagnetic materials at room temperature. In contrast, the mineral lepidocrocite has a much lower T_N of 77 K, and so in principle, it should be straightforward to investigate this material even at room temperature. Thus, NMR studies can be performed under experimental conditions that are closer to those found in real adsorption systems. In addition, typical lepidocrocite samples have large surface areas of 15 to 260 m^2/g.[60] We therefore chose lepidocrocite as our model compound for sorption studies.

In this study, ^{2}H and ^{7}Li MAS NMR spectroscopy was used to probe the local bulk and surface environments of deuterated and lithiated lepidocrocite (γ-FeOOH). ^{2}H MAS NMR is an ideal method to characterize hydroxyl groups as the ^{2}H NMR line shape is very sensitive to the dynamics of the hydroxyl groups.[42] Moreover, ^{2}H has a lower gyromagnetic ratio than ^{1}H, resulting in a reduced dipolar interaction between the nuclear spins and magnetic moments due to the unpaired electrons of the Fe^{3+} ions. ^{7}Li MAS NMR is also a sensitive technique with which to study the lithium adsorption sites and

pH and relative humidity effects on the Li binding. Li^+ was chosen as a model ion with which to study sorption, since we and others have reported the ^{6,7}Li MAS NMR spectra of various lithium-containing paramagnetic materials.[52, 59] Large ^{7}Li hyperfine shifts were observed, which could be related to both the Li local environments (e.g. the number and bond angles of the M – O – Li^+ connectivities), and the number of unpaired electrons in the e_g and t_{2g} orbitals of the transition metal (M^{n+}) ions. Li^+ NMR spectroscopy should also represent a reasonable method for identifying and quantifying the strongest sorption sites that are also likely to bind small, ionic cations such as Ag^+ and Mg^{2+}. We believe that this work should also serve as a good benchmark study allowing us to develop NMR approaches for investigating sorption on Fe^{3+}-containing systems, which should then be extendable to other NMR-active ionic ions such as Na^+ and Cs^+ and to more toxic cations such as Cd^{2+}, Pb^{2+}, etc.

This paper reports results for Li^+ sorption both as a function of pH and as function of different relative humidities. The results are compared with ^{7}Li NMR spectra of Li^+-exchanged lepidocrocite, o-$LiFeO_2$,[18] in order to distinguish between surface and bulk sorption sites and to help establish correlations between Li hyperfine shifts and Li local environments. NMR spectra of lepidocrocite were compared with the previously reported spectra of goethite,[59] allowing potential sites for binding on these materials to be identified.

2.2 Experimental Section

2.2.1 Sample Preparation

2.2.1.1 Deuterated Lepidocrocite. Lepidocrocite from Alfa Aesar, was suspended for one week in D_2O (98%, Cambridge Isotope Laboratories) to prepare deuterated lepidocrocite. The suspended lepidocrocite solution was shaken often. It was centrifuged and freeze-dried.[61]

2.2.1.2 Li^+ Adsorbed Lepidocrocite. 0.3 g lepidocrocite (Alfa Aesar) was suspended in 100ml distilled water. 100ml of a 50mM $^7LiOH{\cdot}H_2O$ (Aldrich) solution was added to the suspension. The pH was then controlled by adding appropriate quantities of either a 1M HNO_3 or 1M NaOH solution to prepare three different suspensions at pH 4.0, 8.1 and 11.4, where the pH was measured by a OAKTON pH 2100 Series with an OAKTON glass electrode. The pH values were chosen based on our measured point of zero charge (PZC), pH 7.1, for our lepidocrocite sample. The solution was stirred for a day and the Li-sorbed samples were then separated by centrifugation (5,000 rpm) and dried in air. The pH 11.4 sample was subdivided and the different parts were stored under different relative humidities of 30% and 84% for one day. The relative humidity was controlled by using saturated solutions of calcium chloride ($CaCl_2$) and potassium chloride (KCl), correspondingly.

A sample with a much lower Li^+ loading level was prepared by adding 100 ml of a 10mM $^7LiOH{\cdot}H_2O$ solution to the 0.3 g lepidocrocite suspension. The same procedures used to synthesize the sample prepared at pH 11.4 were then followed. A pH 11.4 sample was also prepared as a wet paste by using the same method as used for the pH

11.4 sample, but without the drying procedure. Just before the NMR experiment, excess water was removed by pressing the sample between two pieces of filter paper.

2.2.1.3 Li^+ Intercalated Lepidocrocite (o-$LiFeO_2$). 0.3 g lepidocrocite (Alfa Aesar) was added to the solution of 2-phenoxyethanol (Aldrich) and lithium hydroxide (monohydrate) ($^7LiOH\cdot H_2O$, Aldrich). Li/Fe =1 in molar ratio was used. The solution was magnetically stirred and heated to 135 ºC for 4h, as described previously.[18] The Li^+ for H^+ ion-exchanged product was filtered and washed with ethanol several times and then dried under vacuum at 90 ºC.

2.2.2 Characterization

2.2.2.1 X-Ray Diffraction (XRD) and Scanning Electron Microscopy (SEM). XRD data were collected for all samples on a Scintag powder X-ray diffractometer (Cu Kα radiation). All the diffraction patterns were compared with those in the Joint Committee on Powder Diffraction Standards (JCPDS). SEM images were obtained on a Leo 1550.

2.2.2.2 PZC (Point of Zero Charge) and BET (Brunauer, Emmett, and Teller) Surface Area. The particle size distribution and point of zero charge (PZC) were obtained by using a ZetaPlus (Brookhaven Instruments Corporation) for the protonated lepidocrocite sample. No attempt was made to remove the dissolved CO_2 from the solution. The BET surface area for the lepidocrocite sample was measured on a Micromeritics ASAP 2010 gas sorption analyzer using N_2.

2.2.2.3 Thermogravimetric Analysis (TGA) and Differential thermal analysis (DTA). TGA and DTA experiments were performed with a Netzsch (Germany), STA

(simultaneous thermal analysis) 449 Jupiter instrument. The temperature was increased at a rate of 10 ºC/min under an atmosphere of flowing nitrogen N_2. Weight loss was examined at temperatures ranging from ambient to 1050 °C.

2.2.2.4 MAS (Magic Angle Spinning) NMR. ^{2}H MAS NMR experiments were performed on CMX-200 and an INFINITY-360 spectrometers using a 1.8 mm Samoson probe and a 34 kHz spinning frequency (CMX-200) and a Chemagnetics 4mm MAS probe with a 14 kHz spinning frequency (INFINITY-360). A rotor-synchronized, spin-echo pulse sequence was used with a pulse delay of 0.15 s and the ^{2}H NMR spectra were referenced to D_2O at 4.8 ppm. Variable Temperature (VT) experiments were performed from -75 to 150 ºC.

^{7}Li solid-state NMR was performed on the CMX-200 and INFINITY-360 spectrometers. Chemagnetics 3.2 mm and Samoson 1.8 mm MAS probes were used on the CMX-200 spectrometer with 20 and 37 kHz spinning speeds, respectively. Chemagnetics 3.2 and 4 mm MAS probes were used on the INFINITY-360 spectrometer with a 15 kHz spinning speed. A rotor synchronized spin-echo pulse sequence was employed with an evolution period of one rotor period in the NMR experiments. The ^{7}Li NMR spectra were referenced to a 1.0 M ^{7}LiCl solution at 0 ppm. Spin-lattice relaxation (T_1) times were measured by using an inversion-recovery pulse sequence. Spin counting experiments were performed to estimate the Li^+ surface coverage, by comparing the absolute intensity of the signals of those from the lepidocrocite samples with that from solid Li_2CO_3. The absolute intensities were measured by integrating the isotropic peaks and their respective spinning sidebands for data collected with the Chemagnetics 3.2 mm MAS probe on the INFINITY-360 spectrometer. For Li^+-sorbed lepidocrocite, only the

hyperfine-shifted resonances and their spinning side bands were considered. The intensities were normalized by the sample masses and the number of scans. For solid Li_2CO_3, a pulse delay of 1500s was used to acquire four scans with a spin-echo pulse sequence. For the Li^+-sorbed lepidocrocite, a spin-echo pulse sequence with a pulse delay of 0.15 s and 352000 scans were used. In order to correct the intensities for signal loss during the spin-echo sequence, an estimate for the transverse relaxation (T_2) time was obtained by acquiring four spectra with different evolution/refocusing times.

2.3 Results and Discussion

2.3.1 Powder X-ray Diffraction (XRD), Scanning Electron Microscopy (SEM), Point of Zero Charge (PZC), BET Surface Area, Thermogravimetric Analysis (TGA) and Differential thermal analysis (DTA) of Lepidocrocite

No significant differences are seen between the XRD powder patterns of γ-FeOOH and γ-FeOOD (Figure 2.1), and both the positions and relative intensities of the reflections are consistent with those found in the JCPDS file. Based on the Scherer and Warren formulae[62], the particle sizes, determined using the more intense reflections, were calculated to be approximately 12nm. Goethite is observed as a minor impurity phase, the intensities of the reflections due to this phase increasing slightly following the deuteration process. The XRD patterns for the ^{7}Li-doped lepidocrocites obtained as a function of the pH (4.0, 8.1, and 11.4) are identical to those of the starting material (Figure 2.2), respectively, indicating that lithium adsorption does not affect the structure of lepidocrocite. In contrast, Li^+ for H^+ ion-exchange results in a noticeable shift of many

of the reflections, for example, the low angle reflections near 2θ = 14 (200) and 27° (210) moving to higher and lower angles, respectively, consistent with earlier reports that the *a*-lattice parameter increased while the *b*- and *c*-parameters decreased following the ion-exchange (Figure 2.3).[31] Therefore, the XRD data indicate that no substantial Li^+ for H^+ ion-exchange has occurred in the Li^+ sorbed samples, suggesting that the Li^+ ions are only adsorbed on the surface. Again, the goethite reflections became slightly more intense following Li^+ sorption, particularly for the high pH sample, consistent with some conversion of the metastable lepidocrocite phase to goethite, during the sorption process.

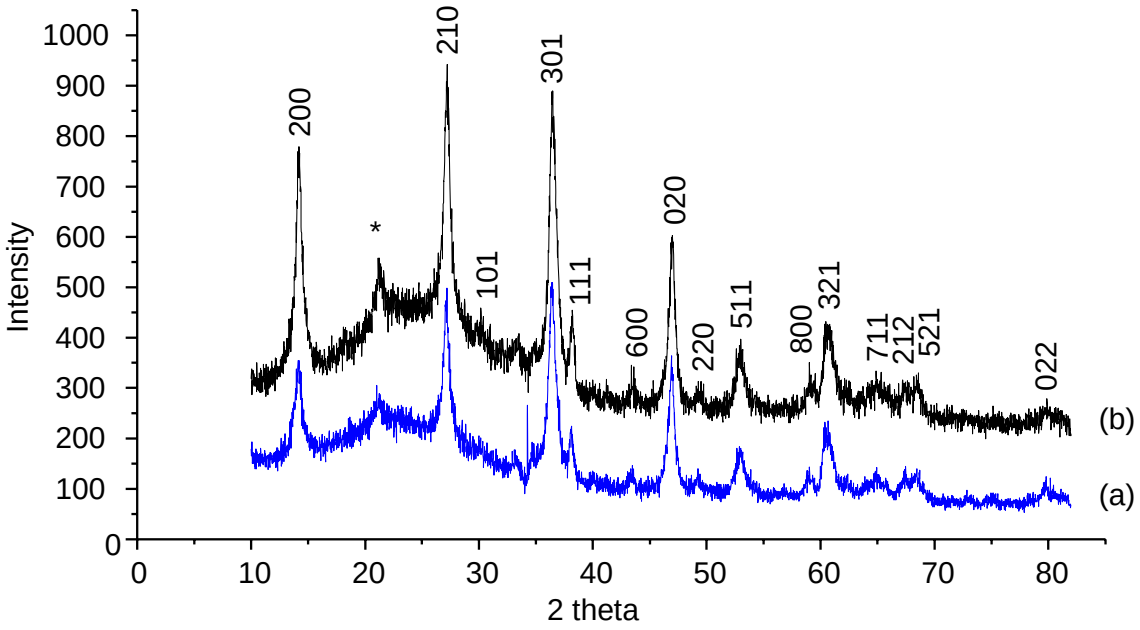

Figure 2.1. X-ray Powder diffraction for (a) γ-FeOOH and (b) γ-FeOOD. (*) denotes the reflection due to the goethite impurity. The broad feature observed at around 15-30° is due to the quartz glass sample holder. Lepidocrocite peaks were indexed by using JCPDS.

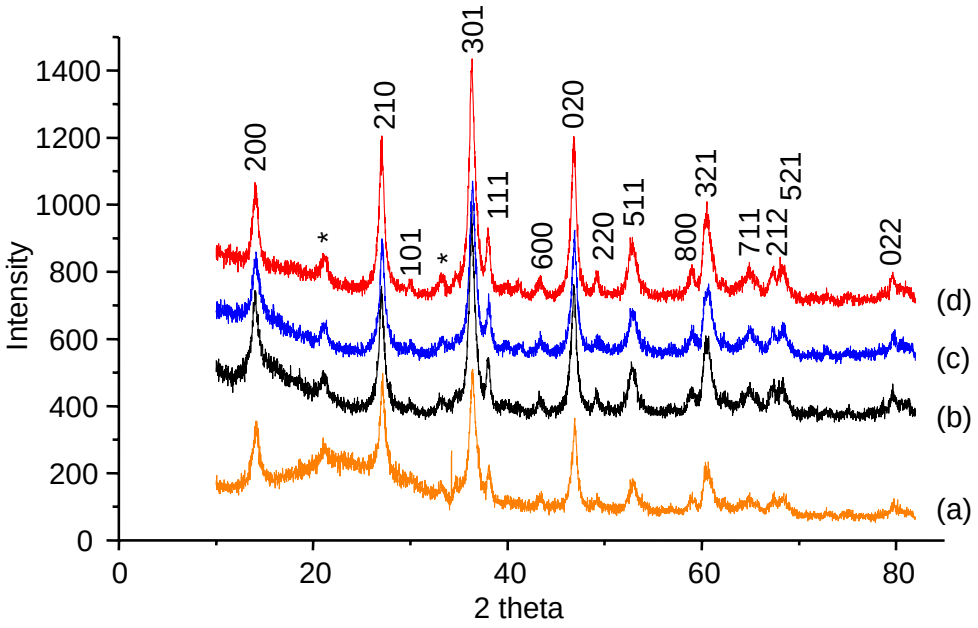

Figure 2.2. X-ray Powder diffraction for (a) γ-FeOOH and ^{7}Li-sorbed lepidocrocite at (b) pH 4.06, (c) pH 8.1 and (d) pH 11.4. (*) denotes the goethite impurity.

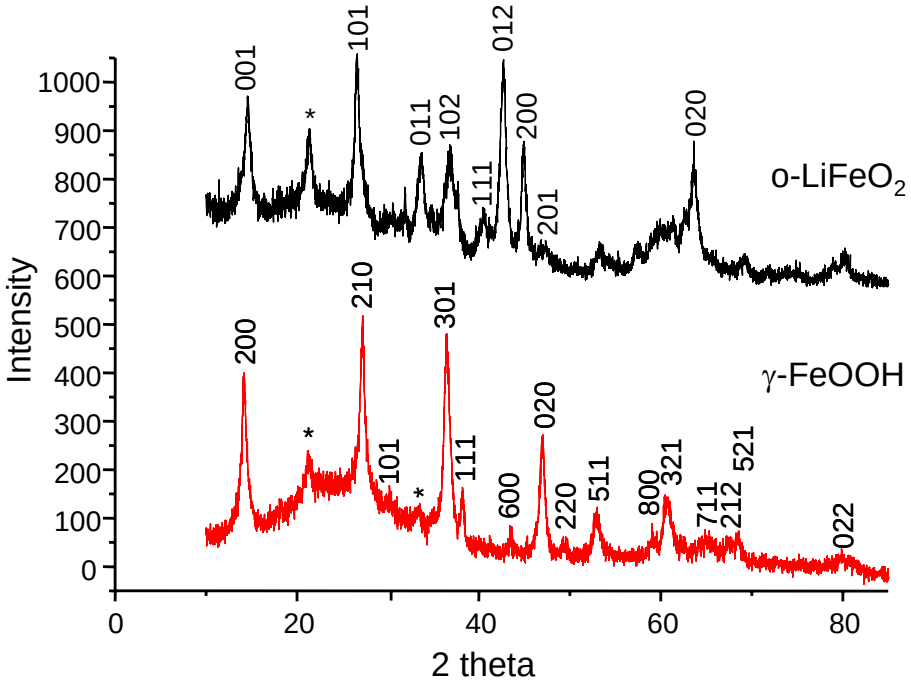

Figure 2.3. X-ray Powder diffraction for γ-FeOOH (bottom) and Li-intercalated lepidocrocite (top). (*) denotes the goethite impurity.

Based on the SEM (Figure 2.4), the lepidocrocite consists of fibrous particles with diameters and lengths of 2 and 300nm, respectively, that form aggregates of 0.5-1μm in diameter. This is one of the characteristic morphologies formed by lepidocrocite. Lath-shaped particles comprise the second most common particle morphology adopted by both natural and synthetic lepidocrocites, with the flat (010) surface representing the predominant surface.[60] The morphology adopted by lepidocrocite depends on the conditions used during the synthesis to oxidize the Fe^{2+}, slow oxidation preferentially inducing the lath-shapes.[60] Fibrous aggregates, as observed in this study, are formed from very fast oxidation at low pH. The presence of these fibers results in a decrease of the relative ratio of the (010) surface to the total surface area. Nonetheless, this surface still remains the predominant face.[1, 63]

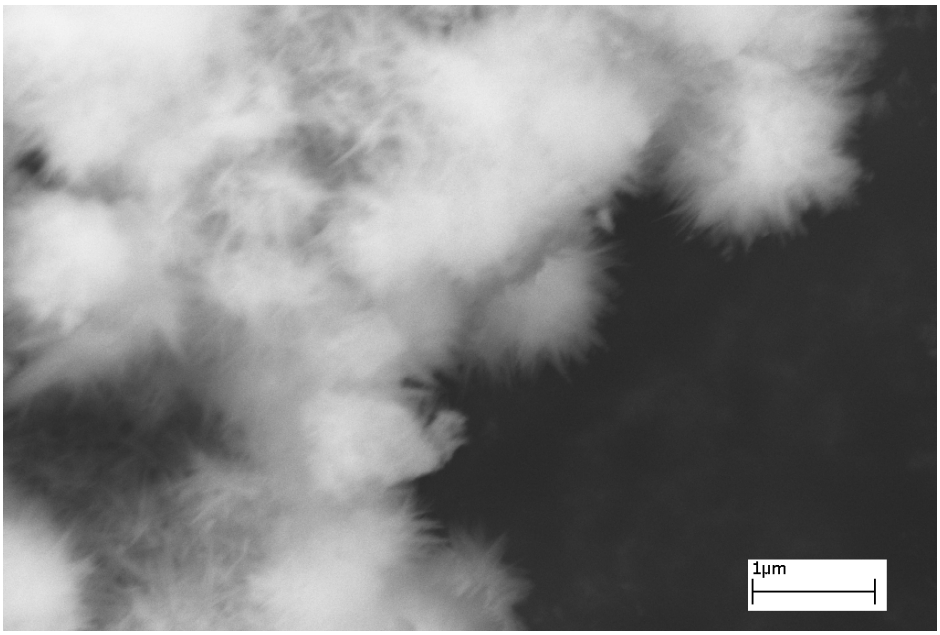

Figure 2.4. Scanning Electron Microscopy (SEM) image of lepidocrocite (γ-FeOOH).

Figure 2.5 shows the PZC measurement for γ-FeOOH. A PZC value close to neutral pH of pH 7.1 (±0.1) was determined from this data, which is consistent with the previously reported PZC data of 6.7, 7.29, and 7.45.[64-66] This result provides additional support for the predominance of the (010) surface, because the (010) face contains neutral and inert Fe_2OH groups. A BET surface area of 85 m^2/g was measured, which is consistent with previously reported values for materials synthesized by using similar methods.[60]

TGA and DTA experiments were performed to measure the water content and thermal stability of γ-FeOOH. TGA of γ-FeOOH showed a gradual weight loss of 7.5 wt % (Figure 2.6) from room temperature to 200 °C. This weight loss is assigned to the loss of surface water. On further heating, lepidocrocite showed a much more sudden additional weight loss of 9.5 wt %, indicating the formation of maghemite (γ-Fe_2O_3) via the reaction: 2 γ-FeOOH → γ-Fe_2O_3 + H_2O. When the temperature approached 400°C, an endothermic peak was seen in the DTA curve, resulting from the transformation to the more stable hematite (α-Fe_2O_3) phase; a small weight loss accompanies this process, consistent with previous reports,[67] possibly due to loss of residual proton defects in γ-Fe_2O_3. These measurements allowed us to determine the temperature range over which lepidocrocite is stable and thus the range that this material could be studied in our variable temperature NMR experiments.

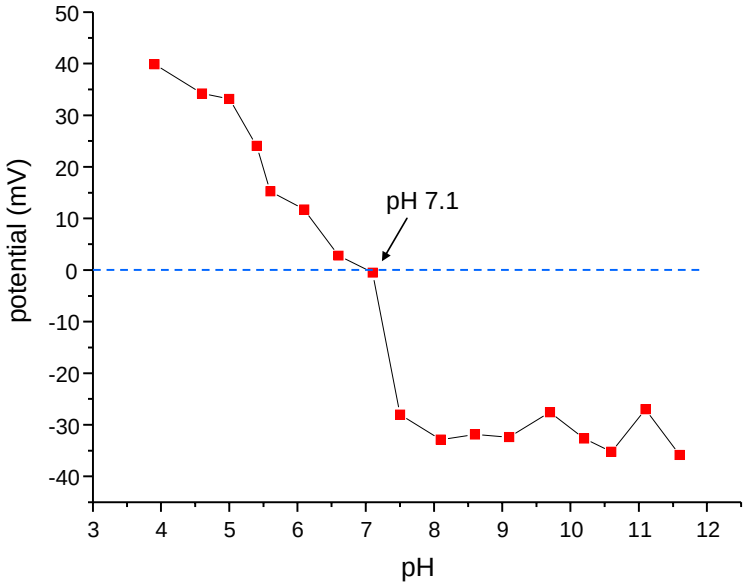

Figure 2.5. The PZC (Point of Zero Charge) analysis curve of γ-FeOOH. The highlighted region in the top curve is expanded in the bottom plot.

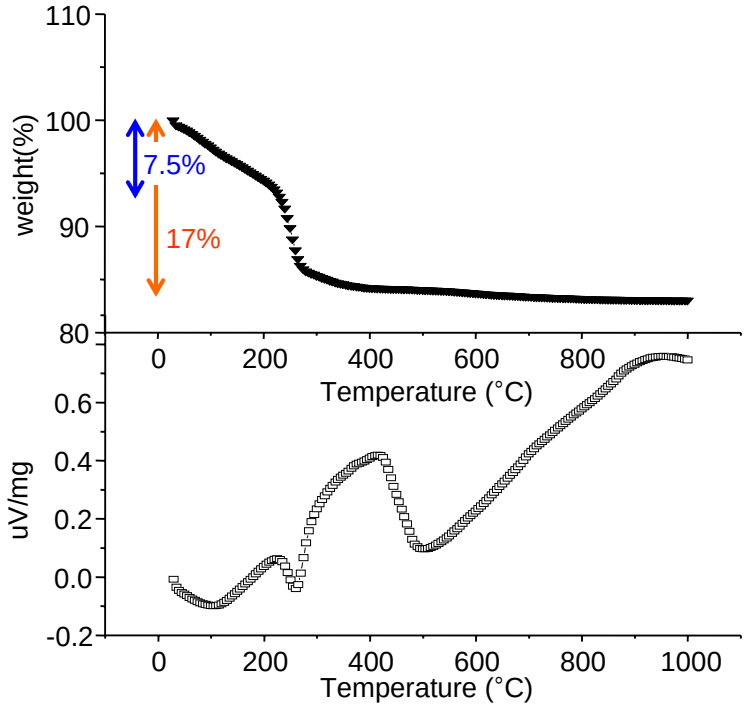

Figure 2.6. TGA and DTA curves for lepidocrocite (γ-FeOOH).

2.3.2 Solid-State NMR

2.3.2.1 ^{2}H NMR of γ-FeOOD

One local environment was detected by ^{2}H MAS NMR in the spectrum of γ-FeOOD, which gave rise to an isotropic peak centered at about 170 ppm with a large sideband manifold (Figure 2.7). This resonance is assigned to bulk sites on the (010) planes, in between the $[FeO_2]^-$ zig-zag layers. A quadrupolar coupling constant (C_Q) of 180(15) kHz was extracted from the ^{2}H MAS NMR spectrum. The C_Q can be used to calculate an O-O distance of 2.65(5) Å, by using equation [1.15]. This value is close to the value of 2.676(4) Å previously reported for the bulk structure,[29] confirming the assignment. The envelope of the ^{2}H NMR sideband manifold resembles that of a typical Pake-doublet indicating that the hydroxyl groups in the structure are rigidly bound between the layers. The large isotropic shift is ascribed to a hyperfine or Fermi-contact shift interaction due to the unpaired spin density that is transferred from the unpaired electrons of the paramagnetic Fe^{3+} ions to the empty 1s orbitals of the deuterium atoms. The signals due to the surface OD groups are presumably hidden by the much more intense resonance from the bulk environments. The line widths of the individual peaks are broader (approx. 3.5 kHz, full width at half-height, FWHH) than those seen for ^{2}H NMR spectra of various MnOOD polymorphs (0.3–1.7 kHz).[51] This is tentatively ascribed, at least in part, to the longer electronic relaxation times of the Fe^{3+}, d^5, unpaired electron spins. No shift of the isotropic resonance was observed in the variable-temperature (VT) ^{2}H NMR spectra of γ-FeOOD (Figure 2.8) on heating up to 150 ºC. This behavior deviates significantly from the Curie-Weiss law, which predicts a 1/T

dependence of the shift, but is consistent with the reported magnetic susceptibility (χ) data reported by Gehring et al.[67] where no significant change in χ was observed in the temperature range studied in this paper. A second set of variable-temperature (VT) ^{2}H NMR experiments were performed at 30, -75, and 30 ºC (Figure 2.9) and again no significant temperature dependence was observed. Furthermore, no change was observed in the NMR spectra after these VT experiments, indicating that the local environments are unaffected by the temperature treatments. The variable-temperature NMR spectra are consistent with the presence of short-range, strong antiferromagnetic (AF) couplings between Fe^{3+} ions at ambient temperature (i.e. well above the Néel temperature, 77 K for lepidocrocite).[1]

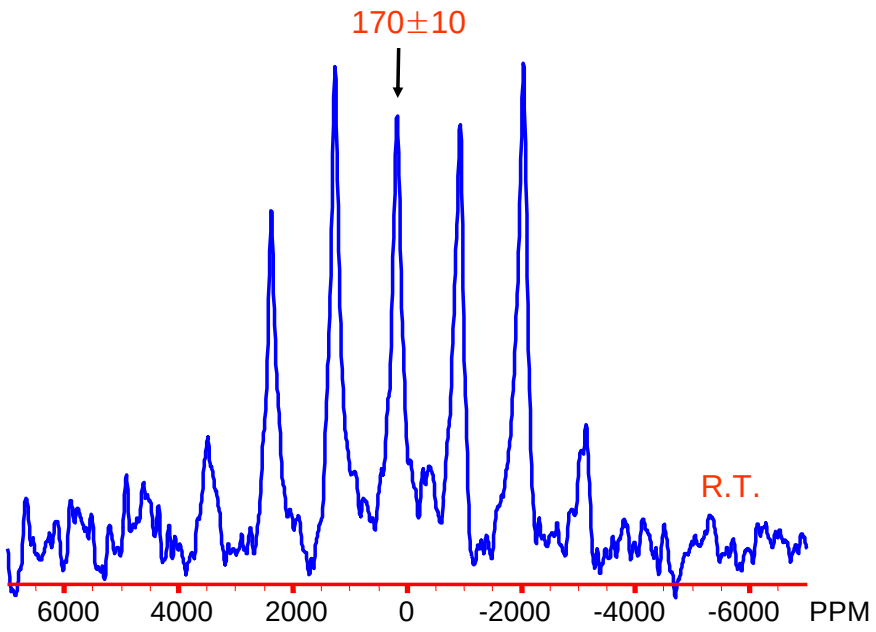

Figure 2.7. ^{2}H MAS NMR spectrum of γ-FeOOD, acquired at room temperature with a 34 kHz spinning rate at a Larmor frequency of 30.66 MHz. The isotropic resonance is labeled.

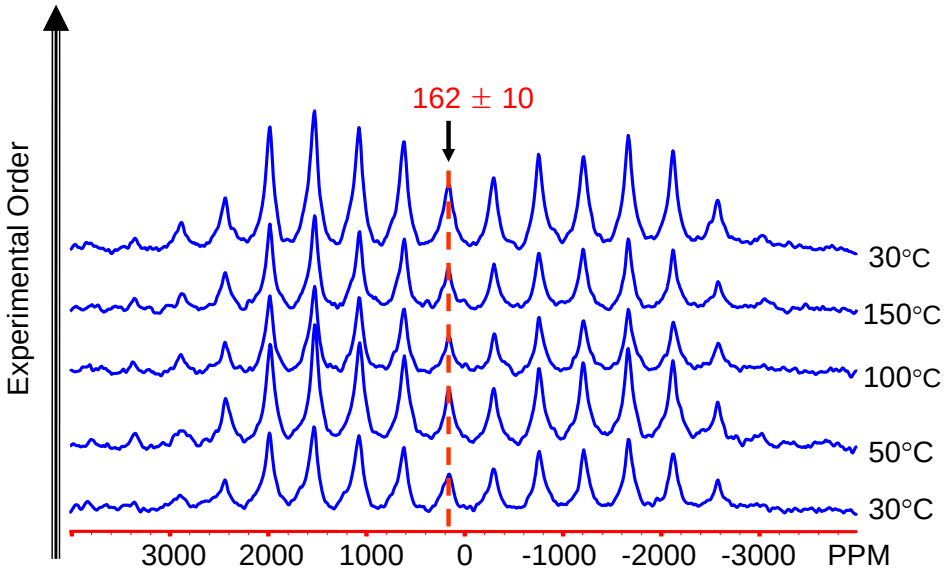

Figure 2.8. The variable-temperature ^{2}H MAS NMR spectra of γ-FeOOD at 30, 50, 100, 150, and then 30°C at a Larmor frequency of 55.27 MHz (from bottom to top). The isotropic resonance is labeled with its hyperfine shift. A MAS spinning speed of 14 kHz was used.

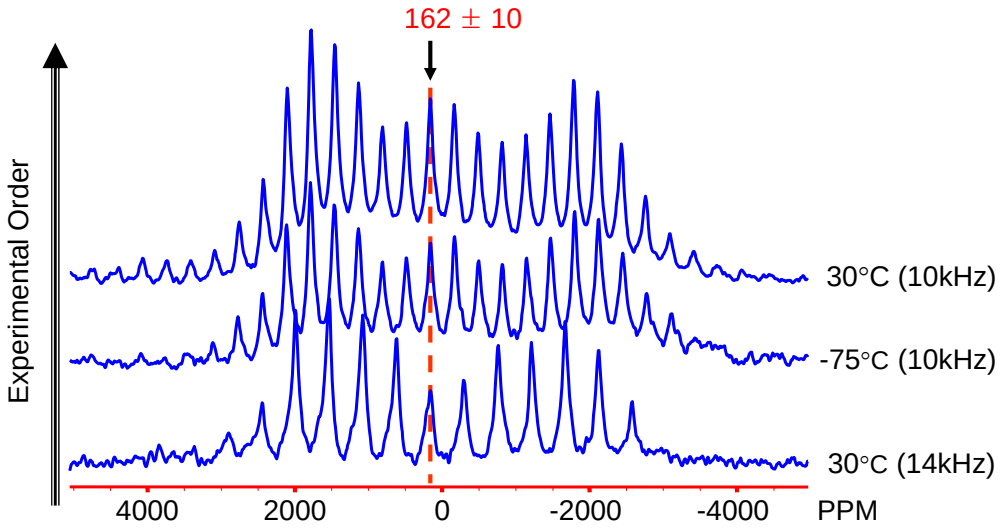

Figure 2.9. Variable-temperature ^{2}H MAS NMR spectra of γ-FeOOD at 30°C (14 kHz), -75°C (10 kHz) and then on returning to 30°C (10 kHz) at a Larmor frequency of 55.27 MHz. The isotropic resonances are labeled.

2.3.2.2 Comparison of the ^{2}H Hyperfine Shifts Seen for Goethite and Lepidocrocite: The Effect of Local Environment *vs.* χ

The size of the hyperfine shifts directly depends on χ_M on the basis of the Hamiltonian of the interaction (equation [1.16]). In order to explore the effect of χ_M on the hyperfine shifts, we now compare the ^{2}H MAS NMR spectra of the FeOOH polymorphs, lepidocrocite and goethite. (The goethite data was previously published in references[50, 59]). The ^{2}H NMR hyperfine shifts for OD groups in lepidocrocite are noticeably larger than those in goethite (170 vs. 90-140 ppm, respectively, where 90 ppm is obtained for the micron-sized goethite, and 140 ppm for the nano-particles), even though the OH groups in goethite are coordinated to three Fe^{3+} ions (Figure 2.10). NMR experiments were performed for the lepidocrocite and nano-sized goethite at 300K and for the micron-sized goethite at 400K (i.e. above its Néel transition).[50, 59] The smaller shift of goethite can, however, be rationalized if the differences in χ_M are considered.

The value for χ_M (110×10^{-6} emu/g·Oe)[68] for lepidocrocite at 300 K is approximately 2.75 and 4 times larger than those of nano-sized at 300K and bulk goethite at 400K, respectively, which are 40×10^{-6} emu/g·Oe[68] and 25×10^{-6} emu/g·Oe[69], respectively (Table 2.1). Thus, based on the lepidocrocite shift of 170 ppm, a shift of $170 \times 3/2 \times (40/110)$, i.e. 93 ppm is calculated for nano-sized goethite, where we have accounted for both the larger number of H-O-Fe connectivities for goethite (3 vs. 2), and the susceptibility. For bulk goethite, a smaller shift of 58 ppm ($170 \times 3/2 \times (25/110)$ ppm) is calculated, consistent with the smaller experimental value seen for this sample (90 ppm). The differences between experimental and calculated values are at least in part

ascribed to the noticeable variations in χ_M measured for nominally similar samples. This result suggests that a similar correction will be required when comparing the Li shifts for Li sorption on the goethite and lepidocrocite materials. A second correction may also be required to account for the strength of the O-D bonds (and thus the extent of the H, 1s – O, 2p overlap) for different types of Fe_nO-D groups. Stronger OD groups will be formed in lepidocrocite (containing Fe_2OD groups) than in goethite (Fe_3OD), which should also lead to larger values of A, and thus hyperfine shifts for lepidocrocite.

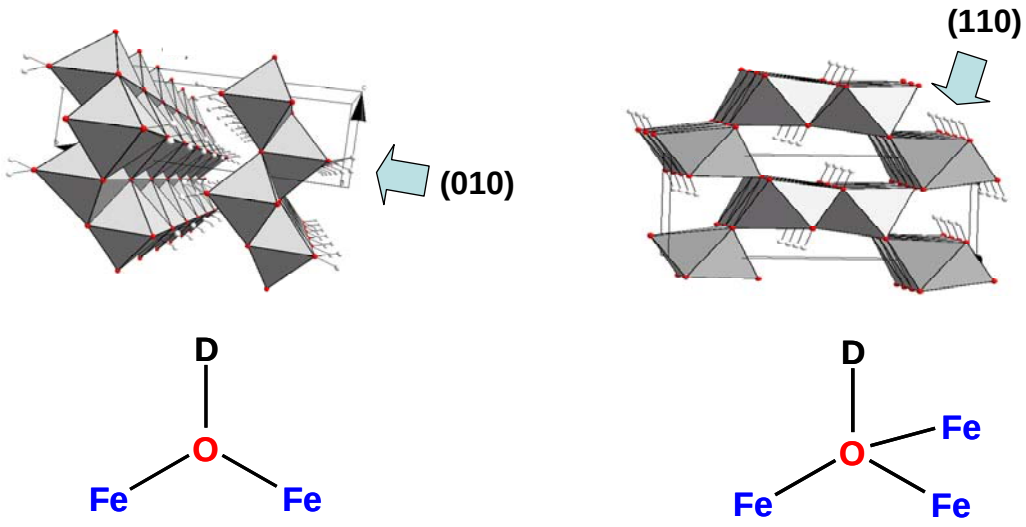

Figure 2.10. The coordination environments of $^2H^+$ ions in lepidocrocite and goethite. Arrows indicate the major faces.

	χ_M (emu/g·Oe)[68, 69]	ppm (^{2}H)	ppm (^{6,7}Li)
γ-FeOOH	110×10^{-6}	170(10)	60
α –FeOOH (micron)	25×10^{-6}	90[50]	
α –FeOOH (nano)	40×10^{-6}	140[59]	140[59]

Table 2.1. Comparison of magnetic susceptibilities and NMR shifts (^{6,7}Li and ^{2}H) of goethite and lepidocrocite. NMR[50, 59] and susceptibilities[68, 69] were extracted from data collected at 300 K (γ-FeOOH and α-FeOOH (nano-sized)) and 400K (micron-sized). Li data are those obtained for sorption at pH 11.4.

2.3.2.3 ^{7}Li NMR of Lepidocrocite

Lithium cation sorption on lepidocrocite was examined by solid-state ^{7}Li MAS NMR spectroscopy as a function of pH (Figure 2.11). Two main ^{7}Li resonances were observed with isotropic shifts of about 53–60 and 0 ppm, where the positions of these isotropic resonances were confirmed by performing experiments at different spinning speeds of 18 and 20 kHz. As the pH is increased from 4.0, 8.1 to 11.4, the relative intensity of the higher frequency resonance increased noticeably (by a factor of 16 from pH 4.0 to 11.4) and the resonance position shifted from 53 to 60 ppm. This indicates that more lithium cations are bound more strongly to the surface of lepidocrocite above its PZC, pH 7.1, than at lower pH. In contrast, no significant change in the intensity of the resonance at 0 ppm was observed as a function of pH. The 53–60 and 0 ppm peaks are assigned to inner-sphere and outer-sphere complexes on the lepidocrocite surface, respectively, based on three main reasons. First, the large shifts of the 53–60 ppm resonances are ascribed to the Fermi-contact shift mechanism in which the unpaired spin-density due to the Fe^{3+} ions is partially transferred to the empty 2s orbitals of the Li^+ ions

through direct Fe-O-Li bonds. A large hyperfine shift is not predicted for the resonance of the outer-sphere complex since it has no direct Li-O-Fe bonds (i.e. the Li^+ ion has no Fe^{3+} ions in the cation first coordination shell). Second, the intensity of the resonance assigned to the inner-sphere resonance is much more sensitive to the pH changes than the intensity of the resonance assigned to the outer-sphere complex. Third, the spectrum of the low loading sample prepared with a 10 mM LiOH solution (not shown here) also contained a resonance with the same large hyperfine shift as that seen for samples prepared with a 50 mM LiOH concentration solution. This allows us to rule out the possibility that the 53–60 ppm resonance is due to the formation of a Fe^{3+}-containing precipitate. An adsorption density for the inner-sphere complex at pH 11.4 was calculated based on the signal intensity of the inner-sphere resonance obtained in the ^7Li MAS NMR spin-counting experiments and the BET surface area of 85 m^2/g. The intensity of the signal was corrected for the short T_2 (approx. 0.2 ms), of the inner-sphere resonance, which leads to approximately 29 % of signal loss during the 2 rotor periods (approx. 0.11 ms) of the spin-echo experiment, resulting in a corrected adsorption density of 3.1 x 3.1 nm^2 per Li ion (i.e. one Li^+ occupies, on average, a surface area of 9.6 nm^2 or 0.1 Li^+/nm^2). [N.b., the short T_2 of this resonance is not due to the short spin-lattice relaxation time (T_1) for Li^+ in this environment, since a T_1 value of 3.5 ms was measured, and further experiments are in progress to identify some of the causes of the short T_2. We note, however, that it is not due to broadening due to the anisotropic bulk magnetic susceptibility.[70]]

The resonance at ≈ 0 ppm is assigned to a Li^+ outer-sphere complex. To confirm this assignment and to ensure that the resonance does not arise from only diamagnetic

impurities such as lithium carbonate (Li_2CO_3) or lithium bicarbonate ($LiHCO_3$), due to incomplete ion exchange or washing, a series of relative humidity (RH) experiments was performed. These experiments were also performed so as to explore the effect of RH on the relative concentrations of the inner and outer-sphere complexes (Figure 2.12). The intensity of the 0 ppm peak increased as a function of increasing relative humidity (0, 30, and 84% RH). An even larger change was seen between the ^7Li MAS NMR spectrum of the wet paste and the dried sample (Figure 2.13), the ratio of the 60 to 0 ppm peak intensity decreasing from approximately 6 to 1 on hydration, as determined by peak integration. This was associated with a decrease in the absolute intensity of the 60 ppm resonance by a factor of two. The increase of the peak intensity of the 0 ppm resonance is ascribed to the increased hydration of the Li^+ inner-sphere complexes, and the formation of outer-sphere complexes (Figure 2.14). This result confirms that the 0 ppm resonance is due to an outer-sphere complex and not solely a diamagnetic impurity or precipitate on the particle.

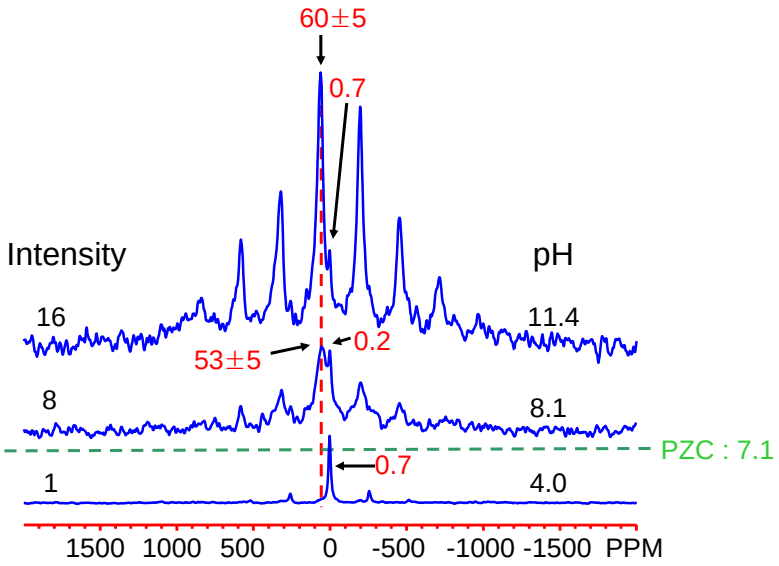

Figure 2.11. ^{7}Li MAS NMR spectra of lithium-ion sorbed lepidocrocite as a function of the pH, collected at a spinning rate of 20 kHz at a Larmor frequency of 77.76 MHz. The integrated intensities of the higher frequency (53-60 ppm) resonance (normalized to the intensity of the resonance of the pH 4.0 sample) and the pH of the solutions are shown on the left and right hand sides, respectively.

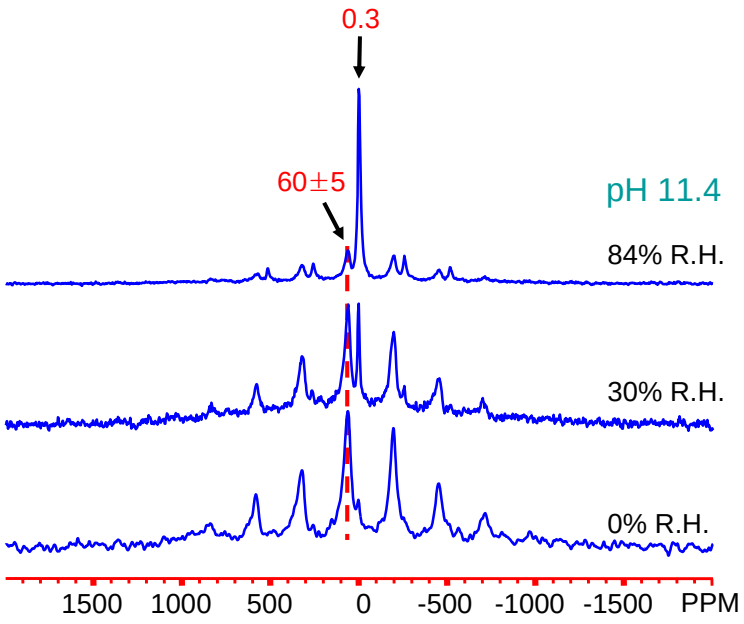

Figure 2.12. Effect of relative humidity on the ^{7}Li MAS NMR spectra of lithium sorbed lepidocrocite at pH 11.4, collected at a spinning rate of 20 kHz at a Larmor frequency of 77.76 MHz.

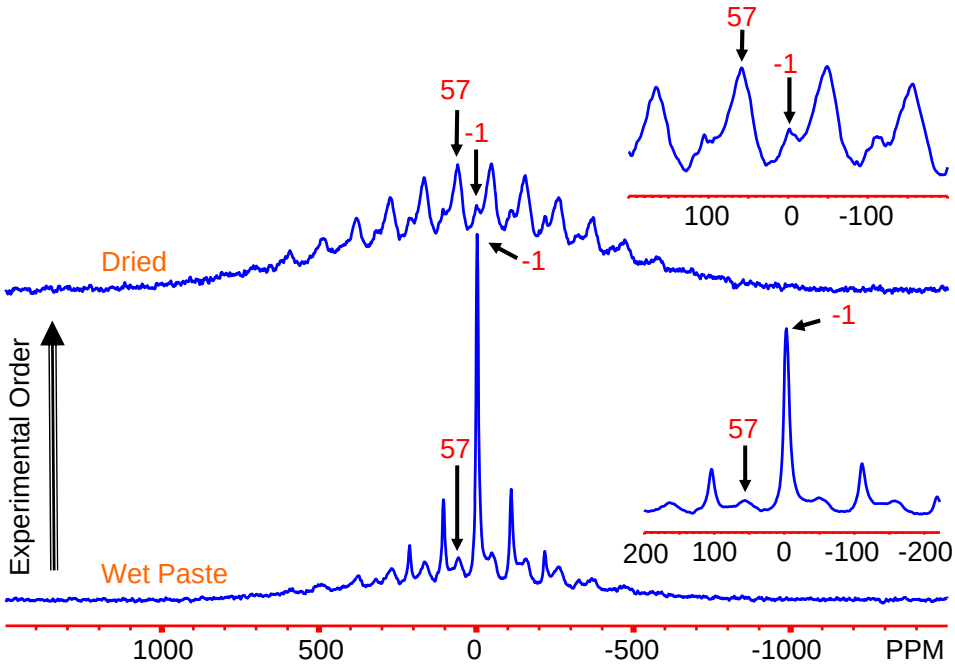

Figure 2.13. ^{7}Li MAS NMR spectra of the wet paste and the dried sample of Li^{+} sorbed on lepidocrocite at pH 11.4, collected at a spinning rate of 15 kHz at a Larmor frequency of 140 MHz.

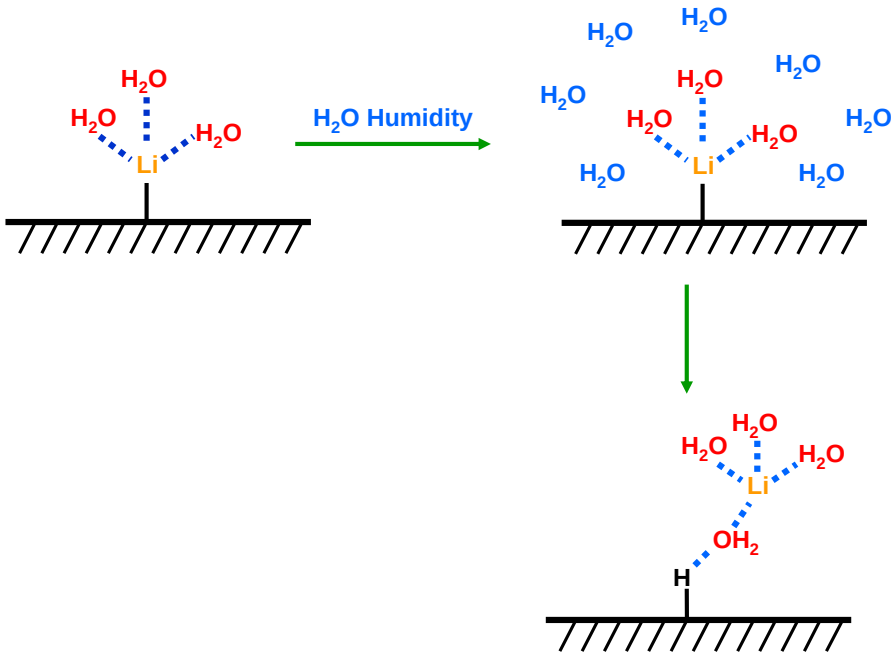

Figure 2.14. A schematic showing the effect of humidity on Li^{+} binding to the lepidocrocite surface.

2.3.2.4 Assigning the Li Hyperfine Shifts to Specific Surface Sites: A ^{6,7}Li NMR Investigation of a Model Iron (III) Oxides

The size of the Fermi-contact shift (i.e. hyperfine) interaction is strongly dependent on the number of Li-O-Fe bonds. Thus, to assign the ^{7}Li NMR resonance at 60 ppm to specific surface site(s), we synthesized the Li-intercalated layered compound o-$LiFeO_2$, which is derived from lepidocrocite via Li^+ for H^+ ion-exchange. In principle, this material should serve as a model compound to allow us to estimate the contribution per Li-O-Fe(III) bond to the overall hyperfine shift, because the position of Li^+ in this material is well characterized.[18, 31] The ^{7}Li MAS NMR spectrum of o-$LiFeO_2$ contains one resonance with an isotropic resonance of about 317 ppm, which is assigned to Li^+ in an octahedral site between the layers (Figure 2.15). The resonance at -1.8 ppm is assigned to diamagnetic impurities such as Li_2CO_3 or $LiHCO_3$ due to its small chemical shift. This result additionally confirms that the resonance at 60 ppm, seen in the Li^+-sorbed samples, is not due to Li^+ ion-exchanged in between the lepidocrocite layers.

Li^+ in the octahedral site between the $[FeO_2]^-$ layers of o-$LiFeO_2$, contains 6 Fe^{3+} ions in its 1st cation coordination shell which are connected to Li^+ via 12 Li-O-Fe^{3+} bonds with bond angles of approximately 90°.[31, 71] Four Fe^{3+} ions are located in the 2nd cation coordination shell resulting in four Li-O-Fe bonds, with bond angles of approx. 180° (Figure 2.16), forming a total of 16 Li-O-Fe connectivities. If the surface-bound Li^+ was located in the same octahedral site, but now on the (010) surface, then the Li^+ ion is connected to 7 Fe^{3+} ions via 10 Li-O-Fe 90° bonds and two 180° bonds. Given that this environment contains more than half the total number of Li-O-Fe connectivities of the

octahedral Li site in o-$LiFeO_2$, and thus should be associated with a shift of greater than (317/2 =) 159.5 ppm, it is immediately clear that the 60 ppm resonance cannot be assigned to this environment. Thus, a more detailed analysis of the hyperfine shift mechanism is required.

As discussed above for the ^2H spectra, the size of the hyperfine shift will depend on the number and nature of Li-O-Fe bonds and the molar susceptibility of the material, χ_M. We assume that χ_M is very similar for lepidocrocite bulk and surface sites which, given the nature of the termination of the surface, appears reasonable (Figure 1.1 (c)), but this is an assumption that will require testing in future studies. Based on our previous investigations of Li^+ hyperfine shifts and the high-spin electronic configuration for Fe^{3+} of $t_{2g}^3e_g^2$, both Li-O-Fe 90° and 180° interactions will result in positive contributions to the hyperfine shift, the former via an interaction between the t_{2g} half-filled d-orbitals and the adjacent 2p O orbitals, and the latter via an e_g (Fe) and 2p (O) interactions. At this point, it is difficult to determine the relative importance of each contribution, but we note that 90° interactions involving ½-filled t_{2g} orbitals in Li-O-Mn^{4+} bonds give rise to similar sizes of shifts as Li-O-Ni^{2+} 180° interactions involving ½-filled e_g orbitals.[52, 53] Thus, as a first approximation, we assume that they result in similar contributions to the overall hyperfine shift. Given a hyperfine shift of 317 ppm for the Li^+ ions in the octahedral site of o-$LiFeO_2$, a contribution to the hyperfine shift of 20-22 ppm per Li-O-Fe connectivity can be estimated. This estimate is slightly lower than that obtained based on the ^6Li NMR shifts observed for the α- and γ-$LiFeO_2$ polymorphs. These materials contain a total of 20 Li-O-Fe bonds in the first and second cation coordination shells, and ^6Li shifts that range from 471-543 ppm[72], giving rise to an average shift of 23-27 ppm per

Li-O-Fe bond. Differences between the shifts calculated for the two sets of compounds presumably arise from variations in χ, Li-O-Fe bond-angles and the degree of Li-O and Fe-O overlap. At this point, it seems reasonable to assume a lower limit of 20 ppm for a Li-O-Fe bond and an upper limit of 30 ppm, for compounds (and local environments) with similar values of χ_M.

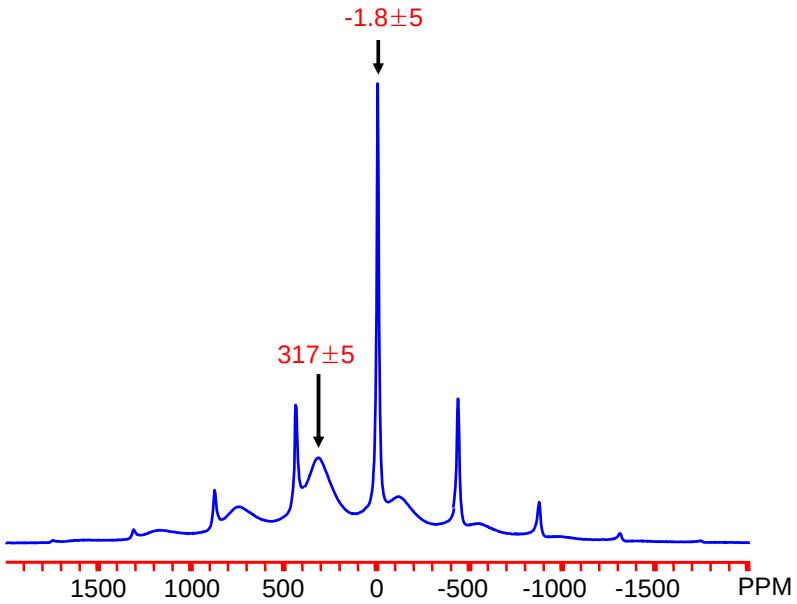

Figure 2.15. ^{7}Li MAS NMR spectrum of lithium intercalated o-LiFeO2, collected at a spinning rate of 37 kHz at 77.76 MHz.

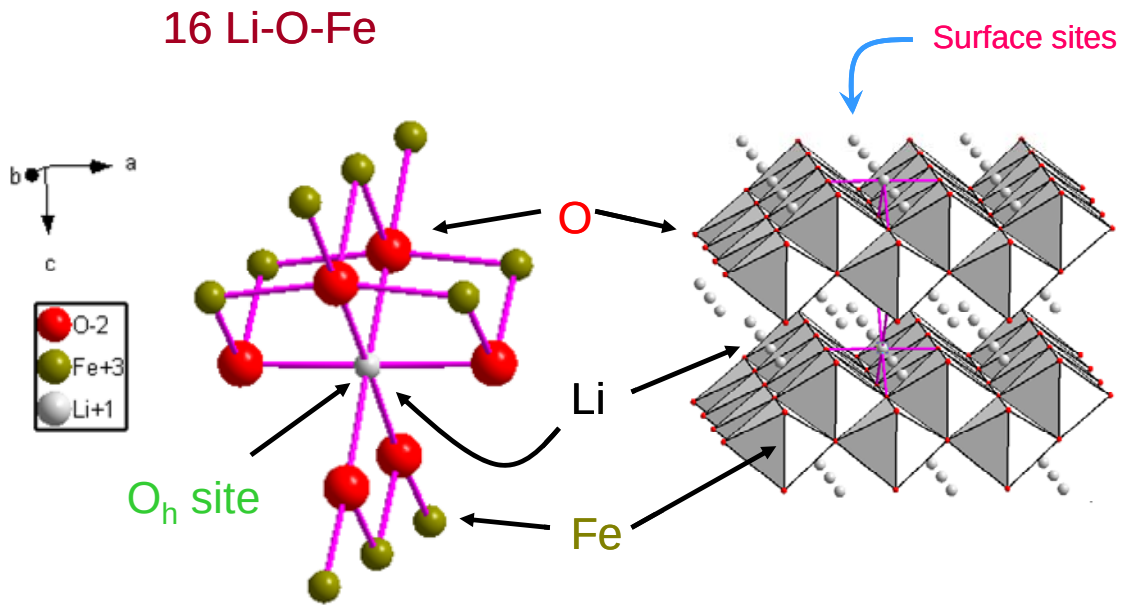

Figure 2.16. Structure of o-$LiFeO_2$ showing the local coordination environment for Li^+ (left-hand side).

2.3.2.5 Locating the Li^+ positions on the surface of lepidocrocite

The lepidocrocite surface is dominated by three faces, (010) (major), and (100), and {001} (minor).[1, 39, 73] The major (010) face is terminated via inert Fe_2OH groups, which are not readily deprotonated. Both the {001} and (100) faces of lepidocrocite have two reactive (proton-terminated) sites, FeO and Fe_3O.[39] Based on a semiempirical model (the MUSIC model), which assigns to partial charges to the various O sites, according to bond valence sums calculated from the number and lengths of the Fe-O bonds and coordination environments of the Fe and O ions,[1, 39] the pK_as for the two groups are predicted to (i) be different for the two surfaces, and (ii) depend quite sensitively on H-bonding to other nearby oxygen atoms, complicating the analysis. The FeOH groups are expected to be only present at high pH while $FeOH_2$ groups will be formed at neutral pH;

the $FeOH_2$ groups are more readily deprotonated than the Fe_3OH groups. The {001} face can be further sub-divided into the (001) and (00$\bar{1}$) faces. The PZC of the (001) face is predicted to be lower than that of the (00$\bar{1}$) face, again according to the MUSIC model.[39]

The shift of 20–30 ppm per Li-O-Fe connectivity, estimated based on the model compounds, suggests that Li^+ ions on the lepidocrocite surface should be coordinated to oxygen atoms in the $[FeO_2]^-$ sheets that are bound to a total of no more than two or three Fe^{3+} ions (Table 2.2). Based on this hypothesis, six possible surface adsorption sites (A1 – A6) for Li^+ among the many potential adsorption sites can be identified (Figure 2.17). These can then be further reduced to a binuclear bidentate (A4) and a monodentate complex (A6), based on the following reasons. The edge-sharing bidentate complexes, A2 and A5, are excluded, because there are no known edge-sharing structures involving $Fe^{3+}O_6$ octahedral and tetrahedral oxyanions in crystalline solids.[74] The monodentate complex, A1, is less favorable because Fe_2OH groups on (010) faces are expected to be inert and will not be deprotonated at the pH ranges studied here.[1, 39] In addition, the monodentate A1 site on the (010) surface is entropically less favorable than the bidentate sites, A3 and A4, because of the chelate effect.[74] The monodentate Fe_3O (A6) site is located on the (00$\bar{1}$) face. Since it can only be deprotonated at high pHs it will likely only contribute to the 60 ppm resonance observed in the pH 11 spectrum. The O-O distances for the double corner sharing binuclear A3 and A4 complexes on the {001} and (100) faces, respectively, are very different, the two faces having (un-relaxed) O-O distances of 3.07 and 3.88 Å, respectively, based on the distances of the bulk material.[29] Given a typical Li-O distance of about 1.7–2 Å, (the exact value depending on the Li coordination number) the O-O (A3) distance on the (100) face is too long for a Li^+ ion to bind

simultaneously to both oxygen atoms, unless a close-to-linear O-Li-O linkage is formed. In this case, there will also be a very short contact with a third oxygen atom (coordinated to three Fe^{3+} ions), and much larger hyperfine shifts are predicted. Consequently, we propose that only the A4 site on the {001} faces plays a major role in adsorbing Li^+ at pH 8 and higher, via the formation of corner sharing binuclear complexes involving the FeOH binding sites. This site must remain a major sorption site until pH 11, because there is only one major local environment for Li^+ from pH 8.1 to 11.4 in our ^7Li NMR spectra (Figure 2.11). The increase in intensity of the ^7Li resonance from pH 8.1 to 11.4 is consistent with the increased deprotonation of the $FeOH_2$ sites (to form FeOH and thus more basic, under coordinated, oxygen sites), and the availability of additional sites such as the Fe_3O, A6 site. These observations are consistent with our measurement of a very low loading level for Li^+ on the surface of lepidocrocite ($0.1 Li^+/nm^2$) based on the spin counting experiments, since all these sites lie on the minority (001)/(00$\bar{1}$) faces.

Our model for Li^+ adsorption on lepidocrocite is similar to models suggested for binding of other small ions such as Cu^{2+} and Cd^{2+}, which have also been proposed to form bidentate corner-sharing complexes on the {001} face.[75, 76] However, Cd^{2+} also forms an edge-sharing complex on the octahedral site of the (010) surface. We do not see any evidence for Li^+-binding to this site in our hydrated samples.

Sites	Number of Li-O-Fe Bonds	NMR Shift (ppm)
A1	2	40-60
A2	3	60-90
A3	2	40-60
A4	2	40-60
A5	2	40-60
A6	3	60-90

Table 2.2. Calculated hyperfine shifts for different possible sites for Li^+ adsorption.

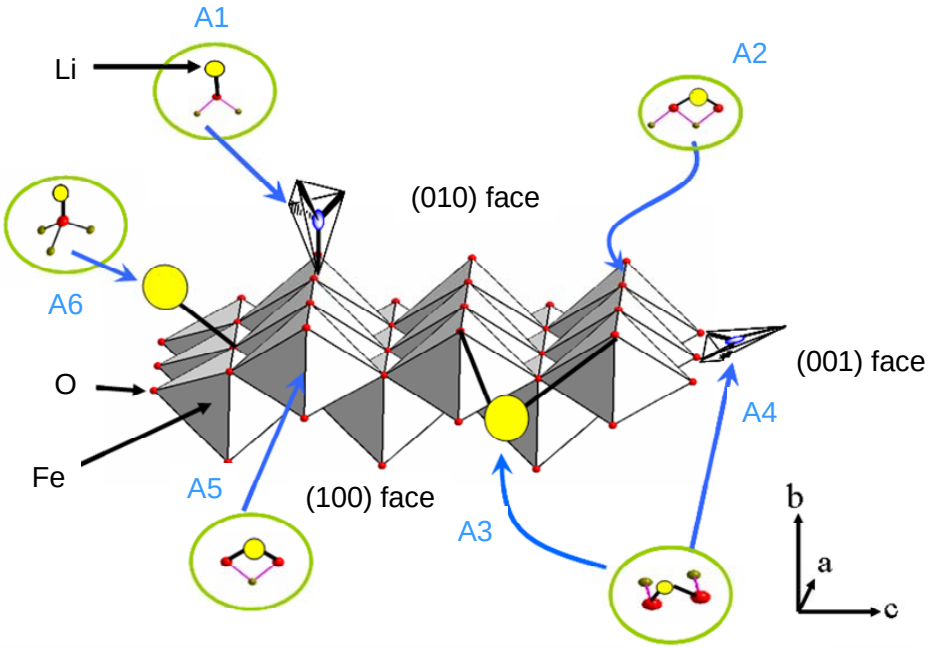

Figure 2.17. Possible positions for the lithium cations on the surface of lepidocrocite.

Finally, based on our additional NMR data for lepidocrocite we can re-analyze the positions for Li^+ on goethite, taking in account the dependence of the hyperfine shift on the bond connectivities between Li^+ and Fe^{3+}. We previously reported ^7Li NMR shifts of 55 and 140 ppm for Li^+ sorbed on goethite at neutral and high pH, respectively, and 289 ppm for Li^+ exchanged inside the tunnels of goethite.[59] The number of binding sites at high pH is noticeably higher than that at close to neutral pH and much higher than the numbers seen for lepidocrocite, when the intensity is normalized to both Fe content and surface area. This implies that Li^+ sorbs on a major goethite surface, i.e. the (101) surface, at high pH. The increased hyperfine shift indicates that Li is binding to multiple oxygen ions. Furthermore, the larger shift, 140 ppm, is now ½ that seen for Li^+ in the tunnels of goethite (289 ppm), suggesting that Li^+ on the surface is coordinated to Fe via approximately ½ the number of Li-O-Fe bonds that are available to the Li^+ ions in the tunnels. The similarity between the hyperfine shift seen in goethite at low pH (55 ppm) and that for lepidocrocite indicates that similar local environments are involved, i.e. bidentate linkages on edges, involving deprotonated $FeOH_2$ groups (Figure 2.18 (a)). That these $FeOH_2$ groups can be deprotonated at neutral pH is consistent with this statement. At high pH, the Fe_3OH groups will also be deprotonated, leaving a large number of undercoordinated oxygen atoms on the (001) face. A higher coordinate site for Li^+ is now present in the pockets that are formed when the tunnels are sliced to expose the (101) plane (Figure 2.18 (b)). This site is similar to the site for Li in the tunnels except that binding to only two tunnel walls is now possible. This site will allow binding to more Fe^{3+} ions and is consistent with the large shift seen at high pH.

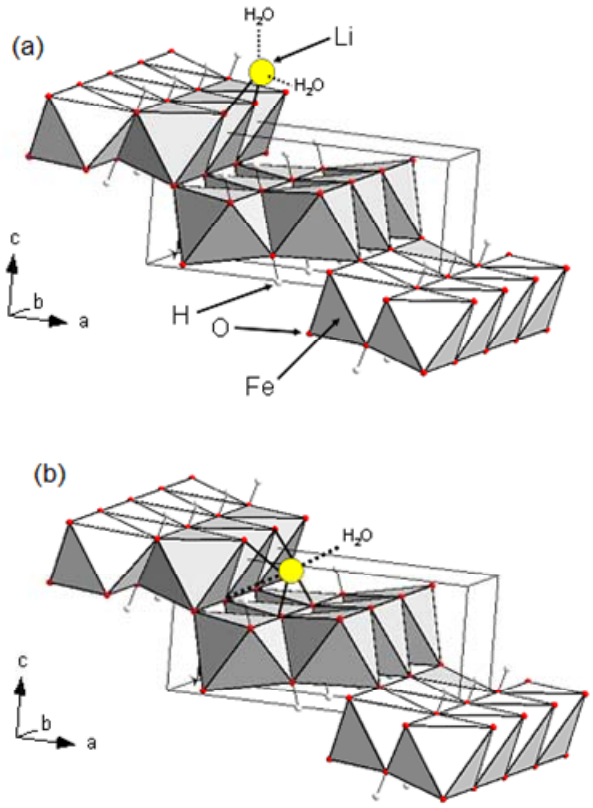

Figure 2.18. Predicted positions for the lithium cations on the surface of goethite at (a) neutral and (b) high pH.

2.4 Conclusion

High resolution NMR spectroscopy of the paramagnetic, iron oxyhydroxide polymorph lepidocrocite has been used to determine hydrogen-bonding distances (^{2}H MAS NMR) and quantify and characterize lithium binding sites (^{7}Li MAS NMR). The large hyperfine shift interactions seen in this system were exploited to distinguish between inner-sphere complex and outer-sphere complexes, and two possible adsorption sites of Li^{+} were proposed based on the sizes of the hyperfine shifts. Li^{+} forms a bidentate complex, on the minor (001)/(00$\bar{1}$) faces (i.e. the edges) of lepidocrocite by

binding to two FeOH oxygen atoms at just above the PZC (7.1). At higher pHs, Fe_3OH sites on the (00$\bar{1}$) face become deprotonated and the formation of second monodentate complex is also likely. Much lower binding concentrations were seen on lepidocrocite, in comparison to the Li binding concentrations seen in our previous study of goethite.[59] Two binding sites for Li^+ on goethite are proposed, both on the major (101) face. Goethite contains tunnels that run down the [001] direction and the (101) face is formed by slicing the tunnels, exposing pockets and edge sites the latter comprising Fe_2OH and FeOH sites. Just above the PZC, Li^+ binds to a bidentate site that is similar to that seen for lepidocrocite, involving two FeOH groups. At pH 11, again the Fe_3OH sites become deprotonated and a site involving both Fe_3O and FeOH oxygen atoms, in the pockets, is occupied by Li^+.

Iron (oxy)hydroxides are ubiquitous in the environment and major sorption sites for toxic ions, and are thus used as cheap sorbents in remediation. The work presented in this paper clearly demonstrates that MAS NMR spectroscopy can used to study ion binding on these classes of materials, opening up new approaches for characterizing and understanding function in these environmentally-relevant systems. The approach can be extended to investigate other paramagnetic systems and to study binding of other, more environmentally relevant sorbents. The water-solid interface represents one of the more poorly characterized systems, particularly in systems where no single crystals are available, yet its structure and dynamics are relevant to the understanding of a wide range of materials and applications, from water splitting catalysts to alkaline batteries. The application of similar NMR approaches to investigate binding in a much wider range of materials can be readily envisaged.

Chapter 3

^{2}H and ^{7}Li Solid State MAS NMR Study of Local Environments and Lithium Adsorption on Akaganeite (β-FeOOH)

Iron oxyhydroxide akaganeite (β-FeOOH) is a common soil mineral and has large surface areas and strong uptake capacities for toxic cation and anions such as Cd^{2+}, Hg^{2+}, and AsO_4^{3-} in the natural environment and in industrial and nuclear wastes. Understanding of the molecular level mechanism of the adsorptions is essential to predict the fate of the adsorbed toxic cation and anions and to design better adsorbent systems. ^{2}H (VT) MAS NMR spectroscopy was applied to characterize surface and bulk hydroxyl groups of this material, which play a role in immobilizing adsorbates. ^{7}Li MAS NMR spectroscopy was used to study Li^{+} sorption itself. The formation of an inner-sphere complex on the surface of akaganeite was confirmed by the observation of a signal with a large ^{7}Li hyperfine shift in the ^{7}Li MAS NMR spectrum. The site specific concentration of the complex was measured. The binding modes and sites of Li^{+} were discussed as a function of pH in detail on the basis of the ^{7}Li hyperfine shifts.

3.1 Introduction

As an extension of these studies of ^{2}H and $^{6,7}Li$ MAS NMR studies of Li^{+} adsorption on goethite (α-FeOOH) and lepidocrocite (γ-FeOOH)[50, 58, 59], we report Li^{+} adsorption on the third FeOOH polymorph akaganeite (β-FeOOH) in this work. Goethite has a Néel temperature, T_N, of above 120 °C when its particles are micron-sized, and it is therefore antiferromagnetically ordered at room temperature.[1] Therefore, in order to obtain well-resolved ^{2}H MAS NMR spectra at room temperature, we needed to reduce the Néel temperature by either cation-doping or by synthesizing nanoparticles.[50] However, akaganeite has a T_N of about 17 °C and very similar Li^{+} binding sites, such as $Fe_3O(H)$, $Fe_2O(H)$, and $FeO(H)/FeO(H_2)$, to those of goethite (Figure 1.1 (b)). (The actual number of hydrogen atoms attached to each surface oxygen group is highly pH-dependent.) Therefore, by choosing akaganeite as a Fe^{3+}-containing model system, we can avoid the issues related to the antiferromagnetic ordering of spins accompanied with goethite, allowing characterizing Li^{+} adsorption under the experimental conditions that are closer to those found in real adsorption environments. Additionally, akaganeite typically has large surface areas of 30 to 280 m^2/g and a tunnel structure which may result in different sorption models.[60, 77, 78] Nonetheless, there have been no studies that identified adsorption modes and sites of any cations on the surface of akaganeite so far, to our knowledge.

In this study, ^{2}H and ^{7}Li MAS NMR spectroscopy was used to probe the local bulk and surface environments of deuterated and Li^{+}-sorbed akaganeites (β-FeOOH). ^{2}H MAS NMR can provide unique insights into the nature of the hydroxyl groups as the ^{2}H

NMR line shape is sensitive to the dynamics of the hydroxyl groups.[42] Moreover, ^{2}H has a lower gyromagnetic ratio than ^{1}H, resulting in a reduced dipolar interaction between the nuclear spins and magnetic moments that arise from the unpaired electrons of the Fe^{3+} ions. ^{7}Li MAS NMR is a direct probe of the lithium adsorption sites and the effect of pH on the Li binding. Li^{+} was chosen as a model ion with which to study sorption, because we and others have reported the [6, 7] ^{7}Li MAS NMR spectra of various lithium-containing paramagnetic materials.[52, 58, 59] The previously observed large ^{7}Li hyperfine shifts could be related to both the Li local environments (e.g. the number and bond angles of the M – O – Li^{+} connectivities), and the number of unpaired electrons in the e_g and t_{2g} orbitals of the transition metal (M^{n+}) ions.[52, 53, 58] ^{7}Li NMR spectroscopy also represents a reasonable method for identifying and quantifying the strongest sorption sites that are likely to bind small and ionic cations such as Ag^{+} and Mg^{2+}.

This contribution reports results for Li^{+} sorption as a function of pH on akaganeite. The results are compared with ^{7}Li NMR spectra of a tunnel-structured $LiFeO_2$,[6] to establish correlations between Li hyperfine shifts and its local environments. The Li^{+} binding sites on the surface of akaganeite are then compared with the previously reported those of goethite and lepidocrocite.[58, 59]

3.2 Experimental Section

3.2.1 Sample preparation

3.2.1.1 Akaganeite: Micron-sized akaganeite (Am). 8.1 g of $FeCl_3$ (Alfa Aesar) was dissolved in 150 ml of distilled water, followed by adding 9.0 g of Urea (Adrich). The

pH was adjusted to 1.5 with a 1M NH_3 solution. The solution was refluxed for 6 h and then cooled down to room temperature. The akaganeite was separated by centrifugation, washed with water several times, and dried at 60 °C.[22, 30]

3.2.1.2 Nano-sized akaganeite (An). 2.7 g of $FeCl_3 \cdot 6H_2O$ was hydrolyzed with 1.4 g of urotropin (Aldrich) at 90 °C for 5 h in 100 ml of distilled water. The pH of the solution was 3.4. The solid product was separated from the mother liquor by centrifugation, washed with water several times, and then freeze dried.[77, 78]

3.2.1.3 Deuterated Akaganeite. As-synthesized akaganeite (Am or An) was suspended for one week in D_2O (98 %, Cambridge Isotope Laboratories) to prepare deuterated akaganeite. The suspended akaganeite solution was shaken regularly during this period and then it was centrifuged and vacuum-dried.[61] The pH of the suspension for Am was around 2.0.

3.2.1.4 Li^+ Adsorbed Akaganeite. 0.3 g of akaganeite (Am) was suspended in 100ml distilled water. 100 ml of a 50 mM $^7LiOH \cdot H_2O$ solution was added to the suspension. The pH was then controlled by adding appropriate quantities of either a 1M HCl or 1M NaOH solution to prepare three different samples at pH 3.6 (Am-3.6), 7.8 (Am-7.8) and 11.9 (Am-11.9), where the pH was measured by a OAKTON pH 2100 Series with a OAKTON glass electrode. Li sorption on the nano-sized samples was also performed with An in the same way at pH 8.2 (An-8.2) and at pH 11.3 (An-11.3). The pH values were chosen on the basis of the measured point of zero charge (PZC), pH 7.4, for Am. The solution was stirred for a day and the Li-sorbed samples were then separated by centrifugation (5,000 rpm) and dried at 80 °C in air.

3.2.1.5 Tunnel-structured $LiFeO_2$. 0.25 g of as-synthesized akaganeite (Am) was added to the solution of 50 ml of ethyl ether phenyl (Aldrich) and lithium hydroxide (monohydrate) ($^7LiOH\cdot H_2O$, Aldrich). A Li/Fe = 5 in molar ratio was used. The solution was stirred with a magnetic stir bar and heated to 110 ºC for 10 h, as described previously.[6] The reaction product was centrifuged and washed with ethanol several times and then vacuum-dried at room temperature for one week.

3.3 Characterization

3.3.1 X-Ray Diffraction (XRD) and Scanning Electron Microscopy (SEM) Transmission Electron Microscope (TEM)

XRD data were collected for all samples on a Rigaku Miniflex XRD bench top X-ray diffractometer (Cr Kα radiation). The measured XRD patterns were converted to the 2Θ values corresponding to Cu Kα radiation. All the diffraction patterns were compared with those in the Joint Committee on Powder Diffraction Standards (JCPDS). SEM images were obtained on a Leo 1550. TEM images were taken on a FEI BioTwinG^2 Transmission Electron Microscope.

3.3.2 PZC (Point of Zero Charge), BET (Brunauer, Emmett, and Teller) Surface Area, and Elemental Analysis. Point of zero charge (PZC) was measured with a ZetaPlus (Brookhaven Instruments Corporation)

No attempt was made to remove the dissolved CO_2 from the solution. The BET surface areas for akaganeite samples (Am and An) were obtained on a Micromeritics ASAP 2010 gas sorption analyzer using N_2. Chloride contents of akaganeite (Am and Am-11.9) were analyzed commercially by a MCC-TOX-100 analyzer (Galbraith Laboratories).

3.3.3 Thermogravimetric Analysis (TGA)

TGA experiments were carried out on a Netzsch (Germany), STA (simultaneous thermal analysis) 449 Jupiter instrument with a temperature ramp of 10 ºC/min from ambient to 1050 °C under nitrogen as a carrier gas. Samples were dried at 80 ºC under vacuum for 12 hours before TGA measurements.

3.3.4 MAS (Magic Angle Spinning) NMR

^{2}H MAS NMR experiments were performed at a Larmor frequency of 55.27 MHz on an INFINITY-360 spectrometer equipped with a Chemagnetics 4mm HX MAS probe, at spinning speeds of 15 and 16 kHz. A rotor-synchronized, spin-echo pulse sequence was used with a pulse delay of 0.15 s and the ^{2}H NMR spectra were referenced to D_2O at

4.8 ppm. Variable-temperature (VT) experiments were carried out from -50 to 120 ºC. Isotropic resonances were confirmed by additional experiments performed with a different spinning speed of 13 kHz.

^{7}Li solid-state NMR was performed on a CMX-200 spectrometer equipped with a Samoson 1.8 mm MAS probe at 34 and 37 kHz spinning speeds. A rotor-synchronized, spin-echo pulse sequence was employed with an evolution period of one rotor period in the NMR experiments. The ^{7}Li NMR spectra were referenced to a 1.0 M ^{7}LiCl solution at 0 ppm. Spin-lattice relaxation (T_1) times were measured by using an inversion-recovery pulse sequence. Spin counting experiments were carried out to estimate the Li^+ surface coverage, by comparing the absolute intensity of the signals from the Li^+-sorbed akaganeite samples with that from solid Li_2CO_3. The absolute intensity was measured by integrating the isotropic peaks and their respective spinning sidebands for data collected at a 37 kHz spinning speed. For the Li^+-sorbed akaganeites, only the hyperfine-shifted resonances and their spinning side bands were considered. For solid Li_2CO_3, a pulse delay of 1500 s was used to acquire four scans with a spin-echo pulse sequencse. For the Li^+-sorbed akaganeite, a spin-echo pulse sequence with a pulse delay of 0.15 s and 70000 scans was used. (The pulse delay was chosen so as to be longer than $5T_1$ times ($T_1 \approx 6$ ms)). The intensities were normalized by the sample masses and the number of scans. In order to correct the intensities for signal loss during the spin-echo sequence, the transverse relaxation (T_2) time was obtained by acquiring six spectra with different evolution/refocusing times, and fitting the intensities as a function of time to an exponential decay.

3.4 Results and Discussion

3.4.1 Powder X-ray Diffraction (XRD), Scanning Electron Microscopy (SEM), Transmission Electron Microscope (TEM), Point of Zero Charge (PZC), Brunauer, Emmett, and Teller (BET) Surface Area, Elemental Analysis, and Thermogravimetric Analysis (TGA) of Akaganeite.

The XRD powder patterns of as-synthesized akaganeites (Am and An) were unambiguously indexed on the basis of JCPDS file #34-1266 (Figure 3.1). No significant structural modification was observed in the XRD during the deuteration of β-FeOOH (Figure 3.1). The XRD patterns for the ^{7}Li-sorbed micron-sized akaganeites at pH 3.6, 7.8, and 11.9 are also identical to that of pristine Am, indicating that lithium adsorption did not cause any structural changes of the akaganeite (Figure 3.2). The XRD patterns of the ^{7}Li-sorbed nano-sized akaganeites are the same as that of An (not shown here). The XRD patterns after the ion exchange reaction to form the tunnel-structured $LiFeO_2$ indicated a significant loss in crystallinity. No significant shifts were, however, seen for most of the reflections, consistent with previous reports (Figure 3.3),[6] except for a notable shift of the 002 peak near 61°, 2θ, indicating a shrinkage of the *c*-axis parameter due to the ion exchange of H with Li.[6]

(i) Micron-sized akaganeite

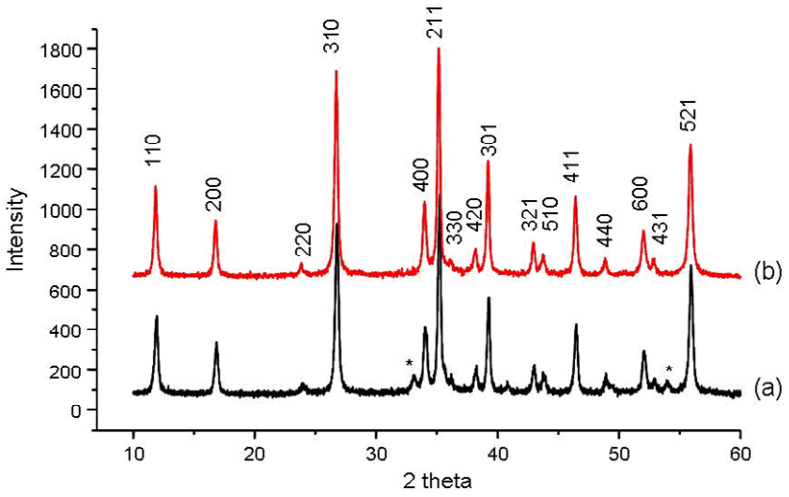

(ii) Nano-sized akaganeite

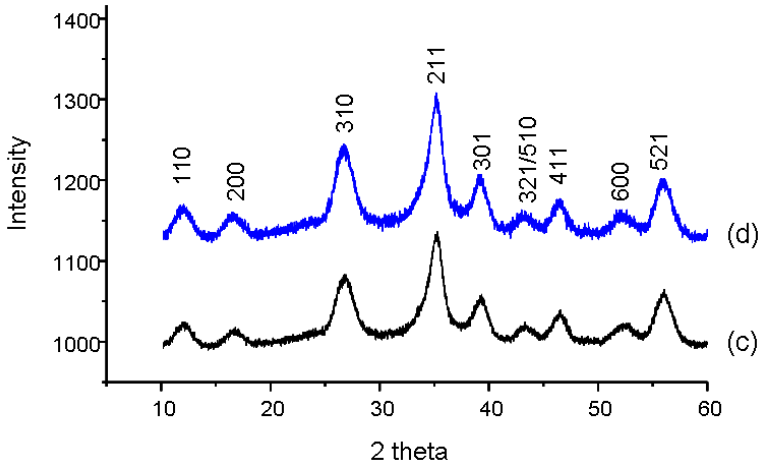

Figure 3.1. X-ray powder diffraction of (a) FeOOH (micro-sized, Am), (b) FeOOD (from Am), (c) FeOOH (nano-sized, An), and (d) FeOOD (from An). (*) denotes salt impurities which were removed after deuteration and re-washing. Akaganeite peaks were indexed by using JCPDS.

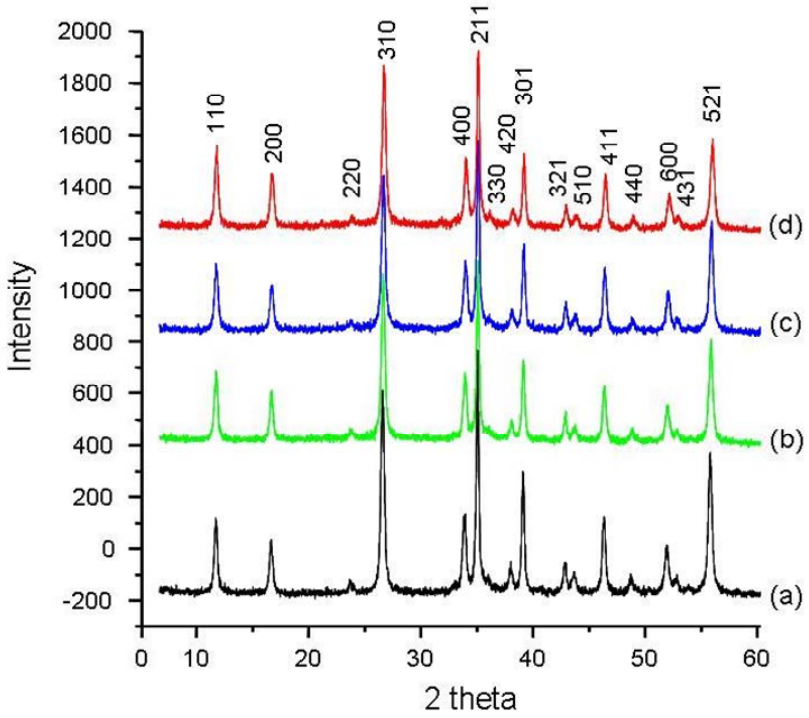

Figure 3.2. X-ray Powder diffraction for (a) β-FeOOH (Am) and (b) ^{7}Li-sorbed akaganeite at pH 3.6 (Am-3.6), (c) pH 7.8 (Am-7.8), and (d) pH 11.9 (Am-11.9).

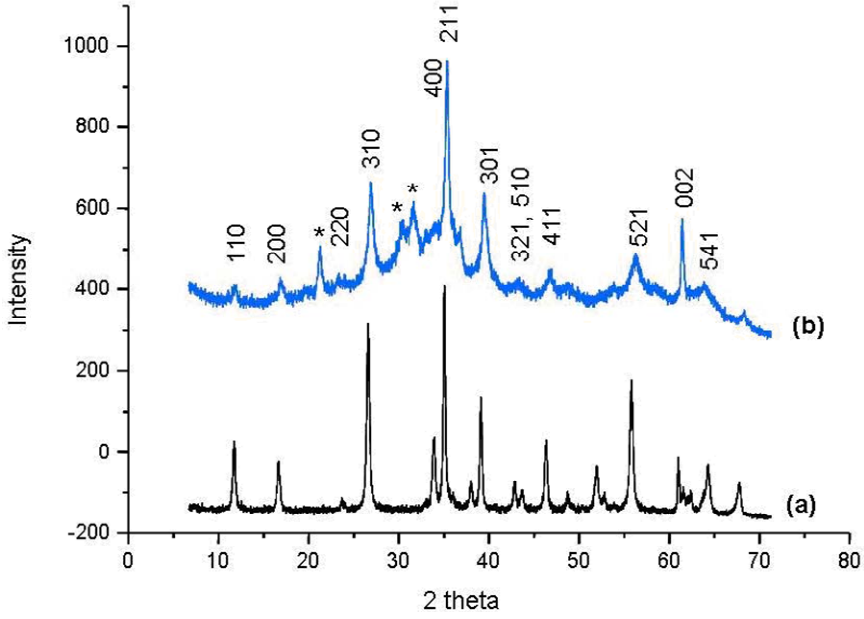

Figure 3.3. X-ray Powder diffraction of (a) β-FeOOH (Am) and (b) tunnel-structured $LiFeO_2$. (*) denotes Li_2CO_3 impurity.

In principle, the morphology adopted by akaganeite can be varied, from somatoids to rod-like crystals by altering the acidity and temperature of synthetic conditions.[60, 79] On the basis of the SEM (Figure 3.4 (a)), our as-synthesized akaganeite (Am) showed cigar-like shapes, 400 nm in length and 10 nm width, which is a typical akaganeite morphology.[22] A TEM image of An contained rod shapes with 5-10 nm length and 5 nm width, which is again consistent with the previously reported data for small particles (Figure 3.4 (b)).[77] The PZC measurement for β-FeOOH (Am) shows a PZC value of pH 7.4 (±0.3), consistent with the reported PZC value of pH 7.3 (Figure 3.5).[9, 13, 80] On the basis of this value, pH conditions for preparing Li^+-sorbed akaganeite samples were established. The measured BET surface areas for Am and An were 33 and 180 m^2/g, respectively, which are consistent with previously reported values for materials synthesized by using similar methods.[22, 30, 60, 77]

In the TGA measurement of Am, there were three main regions of weight loss (Figure 3.6 (a)). A 3% loss was observed from 30 to 150 °C, indicating the loss of water from the surface of akaganeite. The second region is between 150 to 660 °C, over which the complete structural transformation of akaganeite occurs. From 150 °C, a gradual weight loss was observed up to about 230 °C, suggesting that part of the internal water in the tunnel of the akaganeite and most likely some more tightly bound surface water are lost. Around 250 °C, an abrupt weight loss is seen, implying structural decomposition of the akaganeite by loss of HCl and further water, which is consistent with decreasing peak intensities in the previously reported in-situ X-ray diffraction studies.[21, 23, 81] The release of HCl and water inside the tunnel initiates a structural transformation to hematite (α-Fe_2O_3). During the structural transformation, about 19 % weight loss was observed,

consistent with the previously reported data.[82] This transformation continued until 660 °C. Above 660 °C, no further significant weight loss occurred, supporting the formation of the stable phase, hematite. The total loss of water is about 22 %. On the basis of these measurements, the experimental conditions used for the variable temperature (VT) NMR experiments were determined. Am-11.9 showed about 34 % weight loss from room temperature to 660 °C and more complex series of weight losses, possibly due to H_2O bound to Li^+ (Figure 3.6 (b)). Elemental analyses of the Cl^- contents of Am and Am-11.9 show that these materials contain 0.78 weight % and 0.11 weight % of Cl^-, respectively. On the basis of the TGA and elemental analyses, molecular formulas for Am and Am-11.9 were estimated to be $FeOOH{\cdot}0.577H_2O{\cdot}0.022Cl$ and $FeOOH{\cdot}1.836H_2O{\cdot}0.003Cl$, respectively. From this data, it is obvious that the Cl^- content of our materials is low and that it is further reduced during the Li^+ sorption reactions performed at pH 11.9.[22] Nano-sized akaganeite (An) showed 19.8 % weight loss from room temperature to 850 °C (Figure 3.6 (c)) and features that are qualitatively similar to Am, but less pronounced.

(a)

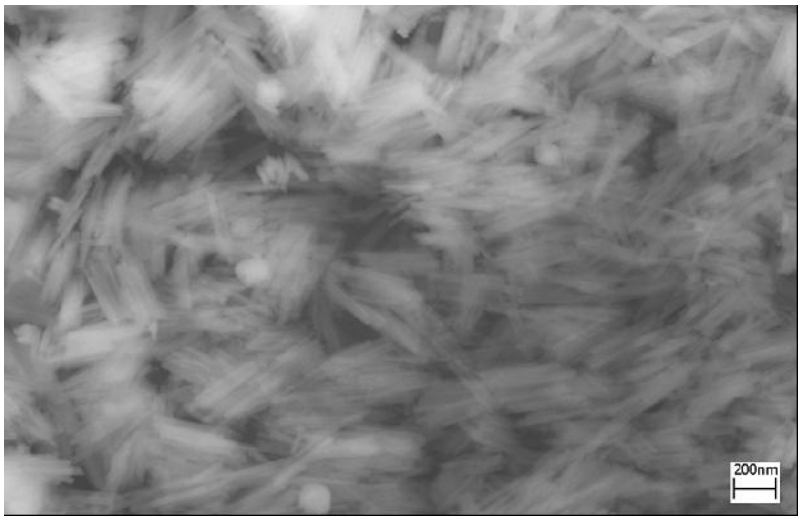

(b)

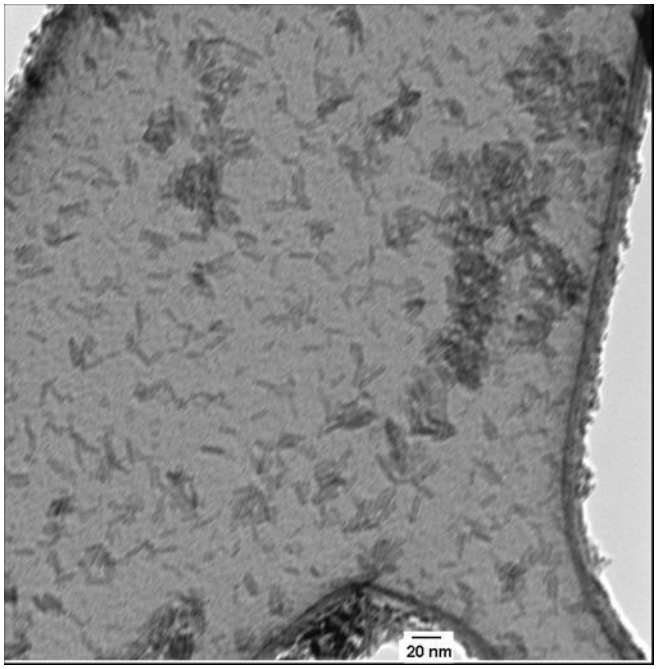

Figure 3.4. (a) Scanning Electron Microscopy (SEM) image of micron (β-FeOOH, Am) and (b) Transmission Electron Microscope (TEM) image of nano (β-FeOOH, An) akaganeite.

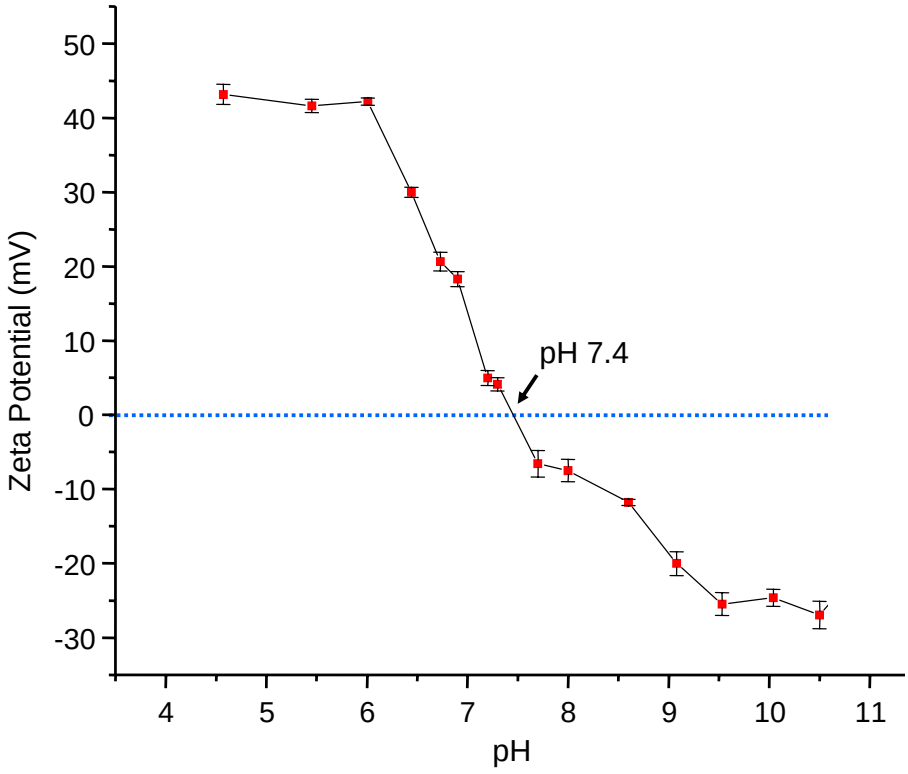

Figure 3.5. The PZC (Point of Zero Charge) analysis curve of β-FeOOH (Am).

(a)

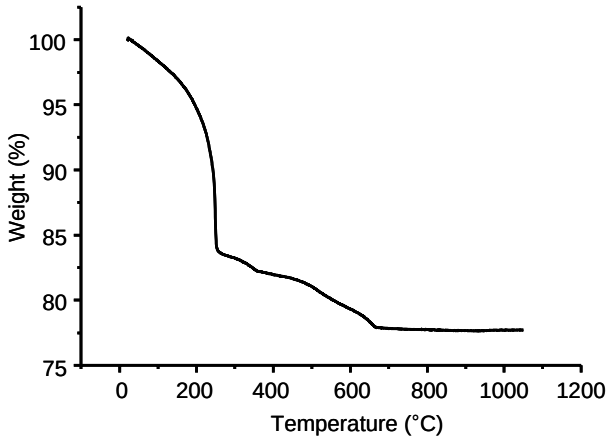

(b)

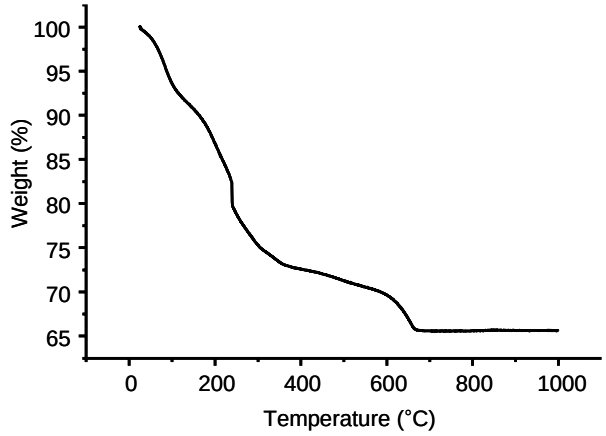

(c)

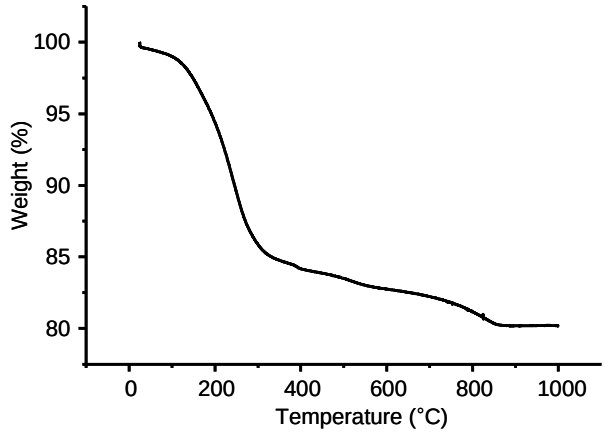

Figure 3.6. TGA curves for (a) Am and (b) Am-11.9 and (c) An.

3.4.2 Solid-State NMR

3.4.2.1 ^{2}H NMR of β-FeOOD (Am and An)

The envelope of the ^{2}H MAS NMR spectrum of β-FeOOD (Am and An) corresponds to a typical Pake-doublet, indicating that there are rigidly bound hydroxyl groups in the structure. (Figure 3.7-3.9). The slight asymmetric envelope of the spectra is attributed to the anisotropic interactions between the ^{2}H nuclei and unpaired electron spins of Fe^{3+} (d^5, high spin), which contributes to the overall sideband manifolds. In the spectra of Am, two local environments were observed with isotropic resonances at 27 and 84 ppm (Figure 3.7 and 3.8). The signal intensity of the 84 ppm resonance was larger than that of the 27 ppm resonance by a factor of approx. 10, indicating a higher concentration of the 84 ppm local environment. (The third resonance at 4.8 ppm is assigned to surface water.) The large isotropic shifts are ascribed to the Fermi-contact shift (hyperfine shift) interaction. The magnitude of hyperfine shift depends on local structure and molar magnetic susceptibility, χ_M, as explained in our previous work.[58] The isotropic peak at 84 ppm is assigned to Fe_3OH sites on the surface (Figure 1.1 (b)) and inside the tunnels (major). These Fe_3OH local environments are very similar to those found in goethite. In our previous work, a peak at 90 ppm was observed for the Fe_3OH local environment for micron-sized goethite. Micron-sized goethite has a very similar χ_M of 24×10^{-6} emu/g·Oe[50, 69] to that of akaganeite, $\chi_M = 30 \times 10^{-6}$ emu/g·Oe.[83] When the structure of akaganeite is cleaved along the (100) or (001) plane, this exposes the Fe_3OH sites inside the tunnel as surface sites (Figure 1.1 (b)). The resonance at 27 ppm is tentatively

assigned to the extra proton site in the pocket inside the tunnel (Figure 1.1 (b)).[23] This assignment is consistent with its weaker intensity and smaller shift because the occupancy of the extra proton site is low and is more weakly bound to the akaganeite framework. However, the relative intensity of the 27 ppm peak to the 84 ppm peak is higher than that expected on the basis of the Cl^- content determined by elemental analysis. This can probably be ascribed to a longer T_2 relaxation time of the extra proton due to the less effective bond overlapping with oxygen p orbital of O-Fe groups. When the particle size of akaganeite was reduced to about 5 nm, the intensity of the 27 ppm resonance decreased dramatically (Figure 3.9). This is most likely due to a decreased amount of the extra protons in the tunnel due to the higher pH used in the synthesis of An (pH 3.4) in comparison to that used for Am (pH 1.5). Further investigations are necessary to confirm this assignment. The increased intensity of the 6 ppm peak was ascribed to the higher surface area of the An sample which increased sorption of water on the surface (Figure 3.9).

In the variable-temperature (VT) experiments of Am, no shift in the ^2H isotropic resonances were observed on heating up to 120 ºC (Figure 3.7). This result is not consistent with the 1/T dependence of the shift expected for a system obeying the Curie-Weiss law. However, it is not surprising since there is no significant change in the magnetic susceptibility (χ) in this experimental temperature range due to the existence of residual antiferromagnetic couplings between Fe^{3+} ions even above 17 ºC, the Néel temperature (T_N) of akaganeite.[1, 8, 84, 85] The heating caused the 4.8 ppm resonance to increase in intensity, most likely by releasing water from the tunnels, which is then bound

to the surface on cooling. The water in the tunnel was not observed in the ^{2}H NMR spectra (Figure 3.7) likely due to its motional dynamics on the MAS NMR time scale (τ_c ≈ 20-200 μs). This would suggest that the 27 ppm environment is somehow involved. The ^{2}H NMR spectrum at -50 ºC showed a featureless resonance with poor signal-to-noise due to antiferromagnetic ordering of akaganeite below its T_N value (Figure 3.8). This phenomenon was previously observed in our study of goethite.[50] No significant modification of the local environments was observed in the NMR spectra before and after heating.

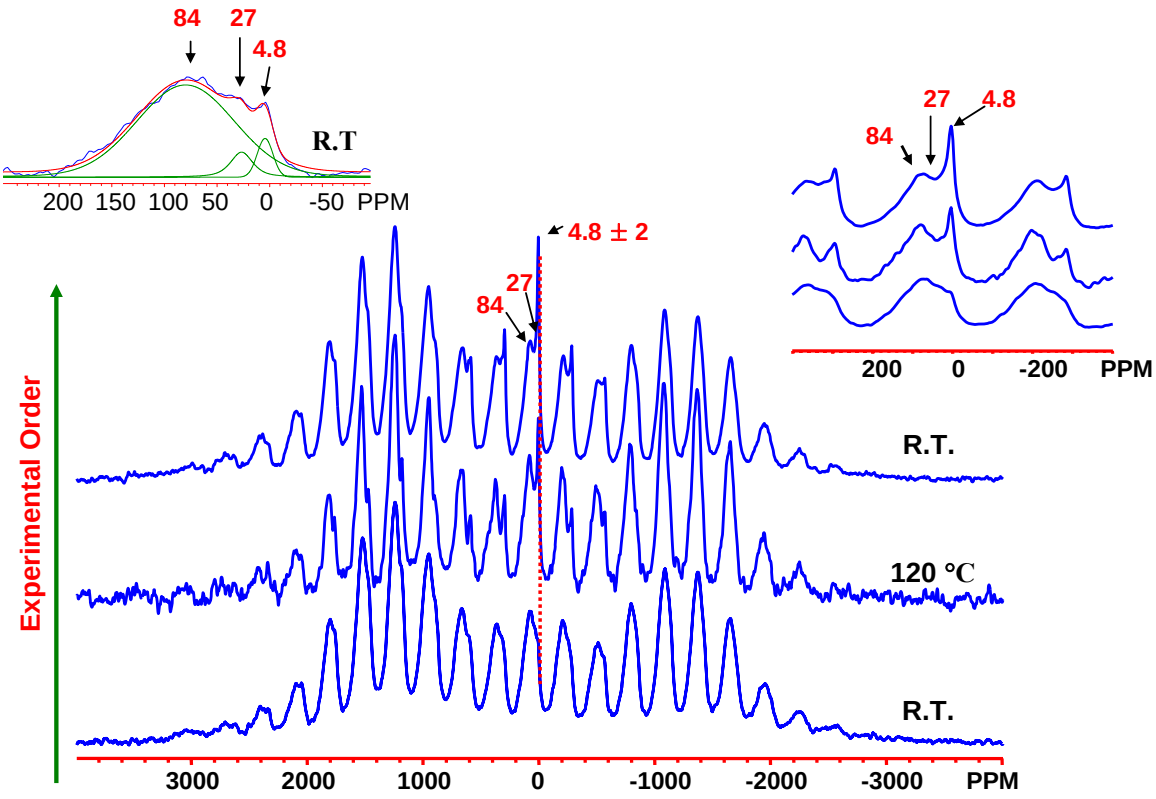

Figure 3.7. Variable-temperature ^{2}H MAS NMR spectra of β-FeOOH (Am) at RT, 120°C, and then upon returning to RT at a Larmor frequency of 55.27 MHz (from bottom to top). The isotropic resonances are labeled with their hyperfine shifts. A MAS spinning speed of 16 kHz was used. Left upper corner inset: Deconvolution of the spectrum acquired at room temperature before heating the sample (peaks (green line) and sum (red line)).

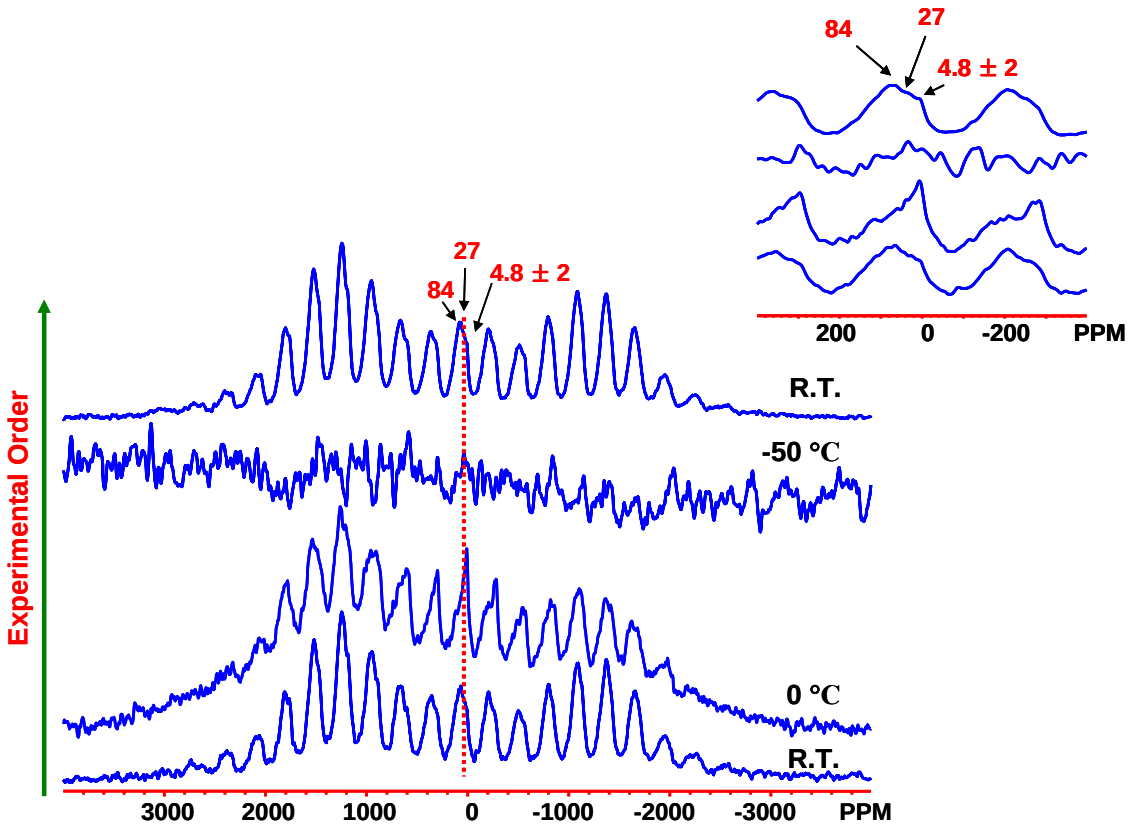

Figure 3.8. Variable-temperature ^{2}H MAS NMR spectra of β-FeOOH (Am) at RT, -50°C and then upon returning to RT at a Larmor frequency of 55.27 MHz. The isotropic resonances are labeled. A MAS spinning speed of 16 kHz was used.

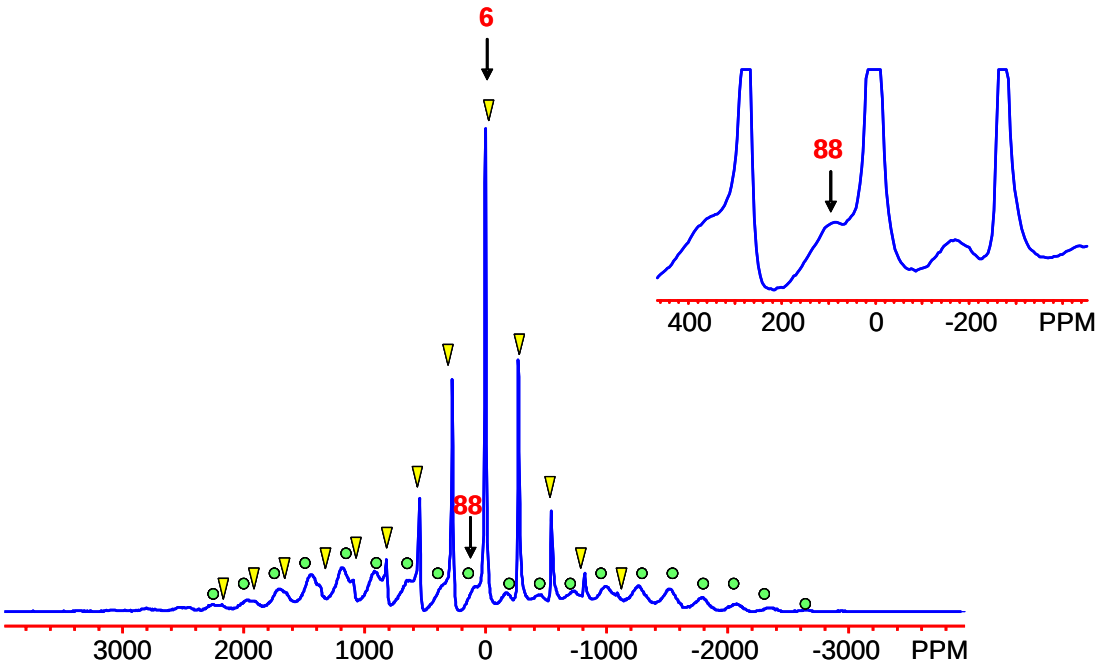

Figure 3.9. ^{2}H MAS NMR spectrum of β-FeOOH (An) acquired at room temperature with a 15 kHz spinning rate at a Larmor frequency of 55.27 MHz. The main isotropic resonances are labeled.

3.4.2.2 ^{7}Li NMR of Li-sorbed β-FeOOH

Lithium cation sorption on akaganeite (Am and An) was investigated by solid-state ^{7}Li MAS NMR spectroscopy as a function of pH. In the case of Am, two isotropic peaks at about 0 and 30-36 ppm (major) were observed at lower and neutral pH and three peaks at about 0, 41 (major), and 74 ppm at pH 11.9, respectively (Figure 3.10). These experiments were repeated three times to confirm the results. The ratio of the 41 to 74 ppm peaks is 1.8 for Am-11.9. (The very small 74 ppm peak in the spectrum of Am-3.6 is from weak adsorption of Li^{+} even at acidic pH.) As the pH increased from pH 3.6 to pH 7.8, which is above the PZC value of akaganeite, the intensity of the peak at about 30-36 ppm increased noticeably by a factor of 5.5. When the pH was adjusted to 11.9, two

new resonances at 41 and 74 ppm were surprisingly observed with intensities that were approximately 30% weaker, compared to that of the 36 ppm peak at neutral pH, indicating a different strength and mode of binding. The peaks at 30-36, 41, and 74 ppm are assigned to Li sites in inner-sphere complexes having direct Li-O-Fe interactions with the surface of akaganeite. This assignment is based on the much larger shifts of these peaks, in comparison to those of diamagnetic lithium compounds such as Li_2CO_3 or $LiHCO_3$ (≈ 0 ppm), larger shifts from the Fermi-contact shift mechanism which involves direct transfer of spin density through the bonds.[58] The general increased peak intensities and shifts seen for the resonances above the PZC value of akaganeite are in agreement with this assignment because more sites are deprotonated, exposing more binding sites as pH increases. Unlike Am, a pronounced increase in intensity of the 77 ppm resonance was observed on going from pH 8.2 to 11.3 for An samples (Figure 3.11). A new resonance at 138 ppm was also observed. The intensity ratio of 138 ppm to 77 ppm is 1.2 on the basis of peak deconvolution (Figure 11).

The adsorption density of Li^+ inner-sphere complex sites was calculated for micron-sized akaganeite on the basis of the integration of the signal intensity and the BET surface area of 33 m^2/g. For Am-7.8 and Am-11.9, adsorption densities of 0.6 × 0.6 nm^2/Li^+ (2.7 Li^+/ nm^2) and 0.72 × 0.72 nm^2/Li^+ (1.9 Li^+/nm^2), respectively, were obtained. This analysis took account into the 24 % signal loss due to transverse relaxation during two rotor periods (39 μs) of the spin-echo pulse sequence. (The transverse relaxation time, T_2, of the isotropic resonances of Am-11.9 was approx. 0.14 ms. The T_2 of the isotropic resonance of Am-7.8 was assumed to be very similar to that of Am-11.9) The decrease of the adsorption density from pH 7.8 to pH 11.9 is ascribed to the formation of

a $LiFeO_2$ precipitate at very high pH. To test this hypothesis, we prepared a ^{6}Li-sorbed sample in the same manner as Am-11.9, but with a longer sorption equilibrium time. A very broad 550 ppm peak was observed in the ^{6}Li NMR experiment, which is a typical shift for the α-$LiFeO_2$ peak[72] (Figure 3.12), confirming our hypothesis. The ratio of the 550 ppm peak to 70 and 130 ppm peaks in intensity was 1.5. The formation of a significant amount of precipitate is not surprising, as akaganeite is a less stable form of iron oxyhydroxides than lepidocrocite and goethite.

0 ppm resonances were assigned to an outer-sphere complex due to their small shift, and much shorter T_1 time (≈ 0.1 s) than that of diamagnetic Li-containing compounds (> 250 s). This assignment is consistent with our recent work on lepidocrocite (γ-FeOOH) where the intensity of the 0 ppm peak was monitored as a function of relative humidity.[58] The 0 ppm peak intensities increased as a function of pH, though the changes are less significant than those of the hyperfine shifted peaks.[58] The increase of the outer-sphere complex was attributed to the increase of weak negative charges on the inert FeO_2(H) sites on the surface of akaganeite as a function of pH.[39]

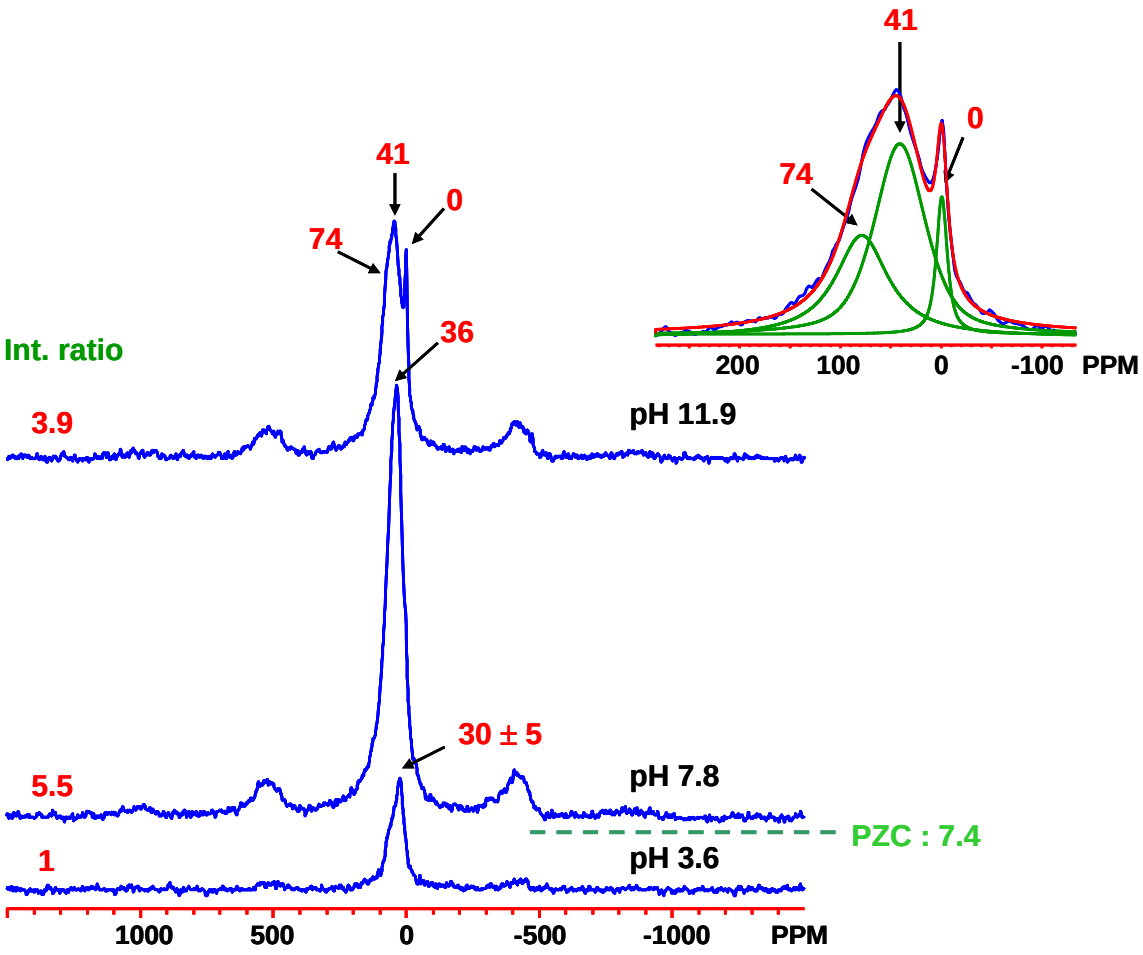

Figure 3.10. ^{7}Li MAS NMR spectra of lithium-ion sorbed micron-sized akaganeite (Am-3.6, 7.8, and 11.9 from the bottom) as a function of the pH, collected at a spinning rate of 37 kHz at a Larmor frequency of 77.76 MHz. The integrated intensities of the higher frequency (30-74 ppm) resonances (normalized to the intensity of the resonance of the pH 3.6 sample) and the pH of the solutions are shown on the left and right hand sides, respectively. Right upper corner inset: Deconvolution of Am-11.9 spectrum (peaks (green line) and sum (red line)).

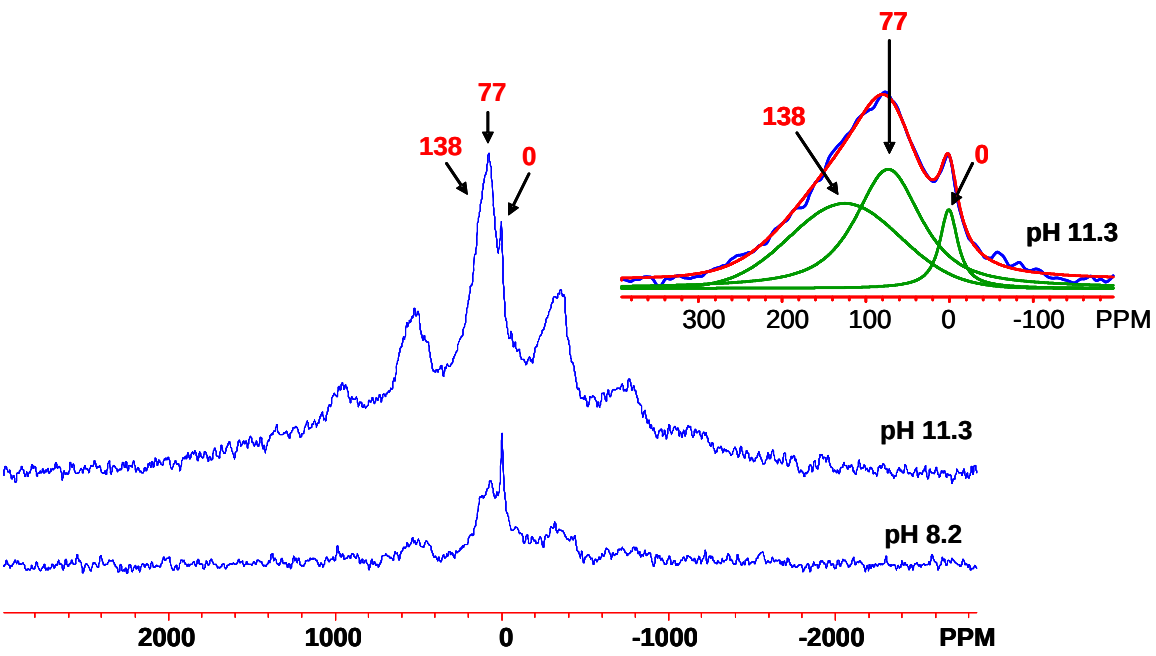

Figure 3.11. ^{7}Li MAS NMR spectra of lithium-ion sorbed nano-akaganeite (An-8.2 and An-11.3 from the bottom) as a function of the pH, collected at a spinning rate of 34 kHz at a Larmor frequency of 77.76 MHz. The pH of the solutions are shown on the right hand side. Right inset: Deconvolution of An-11.3 spectrum (peaks (green line) and sum (red line)).

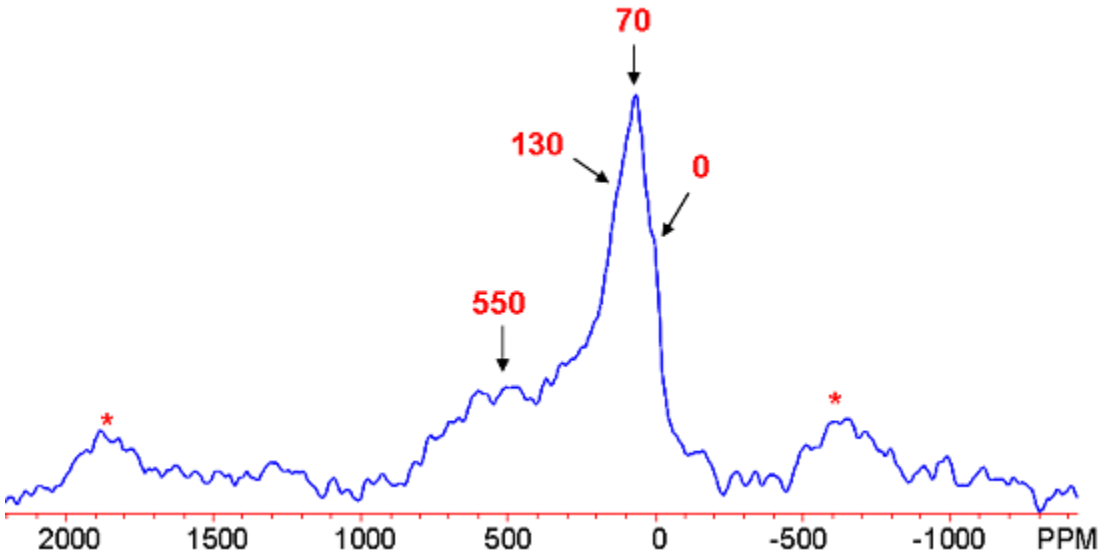

Figure 3.12. The ^{6}Li MAS NMR spectrum of ^{6}Li-sorbed Am at 37 kHz at a Larmor frequency of 29.45 MHz. The isotropic resonance is labeled. (* indicates spinning sidebands.)

3.4.2.3 A ^{7}Li NMR of Tunnel-structured $LiFeO_2$ and Identification of the Li^+ Positions on the Surface of Akaganeite

The size of the Fermi-contact shift (i.e. hyperfine) interaction is strongly dependent on the number of Li-O-Fe bonds and can therefore be used to help assign the resonances to specific surface sites.[52, 58] In order to aid in the assignments, we acquired a ^{7}Li NMR spectrum of the $LiFeO_2$ tunnel structure, observing a very broad resonance of 137 ± 3 ppm (Figure 3.13). The Li^+ ions occupy the vacant tetrahedral sites in this model compound (Figure 1.1 (b) and Figure 3.13).[6] Since the Li^+ ions are bound to three framework O sites, each O atom being bound to 3 Fe^{3+} ions, using the same approach adopted in our earlier paper[58], we estimate an average contribution per Li-O-Fe(III) connectivity to the overall hyperfine shift of 15 ppm per Li-O-Fe (III) connectivity (Figure 3.13).

The akaganeite surface is dominated by two faces, (100) and (001).[1] We presume that these faces represent the main adsorption planes on the surface. In acidic conditions, these faces are terminated via two reactive groups, Fe_3OH and $FeOH_2$, and one inert Fe_2OH group, which has been shown to be difficult to deprotonate on the basis of a semiempirical model that has been used to calculate the oxygen partial charges (Figure 1.1 (b) and 3.14).[39] Using the data from the model compound (the shift of about 15 ppm per Li-O-Fe connectivity), it is possible to estimate the hyperfine shifts associated with Li in for several possible adsorption sites (Figure 3.14 and Table 3.1). This information can then be used to assign each resonance in ^{7}Li NMR spectra to specific local environments. The 30-36 ppm resonances seen at low and neutral pH and 41 ppm peaks seen at high pH

are assigned to Li^+ ions that are coordinated to oxygen atoms that are bound to only two Fe^{3+} ions. The peak shift from 30-36 ppm to 41 ppm was ascribed to the formation of stronger binding of the Li^+ ion at high pH or to the formation of a third Li-O-Fe interaction. Similarly, the resonances at 75 and 138 ppm are due to 5 and 9 Li-O-Fe interactions. The most plausible surface adsorption site on the surface at each pH condition can then be proposed (Figure 3.14). The resonances at 30-36 ppm and 41 ppm are assigned to binuclear bidentate site, L1, which consists of $FeOH_2$ groups (Figure 1.1 and 3.14). This assignment is based on the fact that the $FeOH_2$ groups are deprotonated at lower pH than the Fe_3OH groups. However, Li^+ adsorption at L3 site, which has only Fe_3OH groups, may also contribute significantly to the intensity of the 41 ppm peak because the less acidic Fe_3OH oxygen atom is deprotonated in very basic conditions (e.g. pH 11.9) which would allow Li^+ to adsorb on this site. The peak at 74-77 ppm was assigned to L2. When the Fe_3OH oxygen atom is deprotonated at high pH, a significant amount of Li^+ can be bound to oxygens at both the L1 and L3 sites, giving rise to the L2 site and resulting in peaks at 74-77 ppm due to the increased number of Li-O-Fe connections. The 138 ppm peak of An-11.3 was assigned to L6 rather than L4, even though both sites have 9 Li-O-Fe interactions.[58] Nano-sized particles are expected to have an increased number of easily accessible L6 sites to adsorb Li^+ within the tunnel due to the shorter length of the tunnel along the (010) plane compared to micron-sized particles. The sites, L5 and L7, were ruled out in our assignment because the estimated hyperfine shifts of these sites do not match with any observed shifts (Table 3.1). In addition, the sites of L5 and L8 are not predicted to form strong binding with Li^+ due to the involvement of the inert Fe_2OH sites (Figure 1.1 and 3.14). That the (100) and (001)

faces of akaganeite represent major adsorption planes is consistent with the increased loading level of Li^+ on the surface of akaganeite (Am) (1.9 - 2.7 Li^+/nm^2 above its PZC) by a factor of about 20 compared to that of lepidocrocite (0.1 Li^+/nm^2)[58] in the spin counting experiments. Therefore, this implies that akaganeite is a better system for adsorption of small cations than lepidocrocite due to having more $FeOH_2$ and Fe_3OH sites.

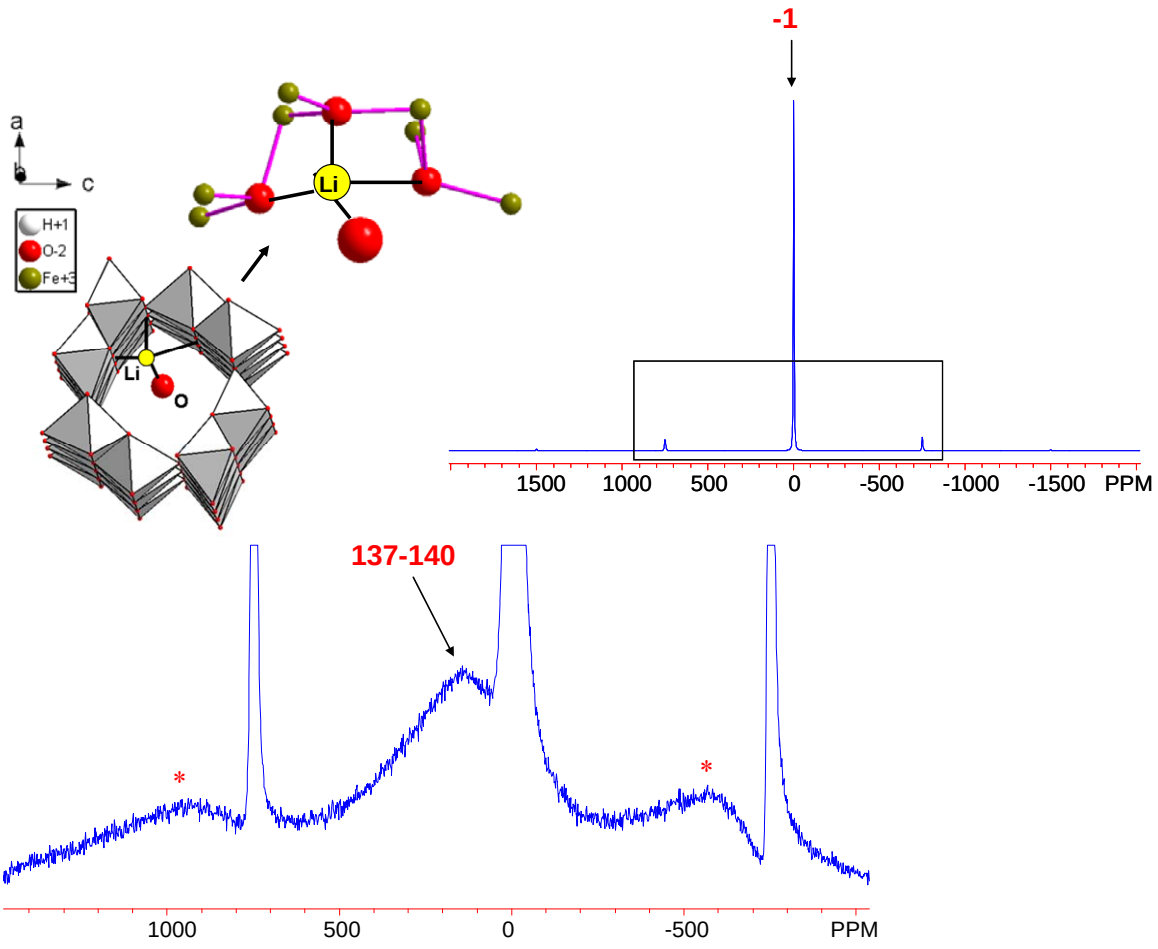

Figure 3.13. Zoom of the ^7Li MAS NMR spectrum of the tunnel-structured $LiFeO_2$ acquired at a spinning speed of 58 kHz at a Larmor frequency of 77.76 MHz. The isotropic resonance is labeled. (* indicates spinning sidebands.) Upper right corner inset: Full spectrum; black rectangular box indicates the zoomed region. Upper left corner inset: Li^+ ions in the vacant tetrahedral sites inside the tunnel of the $LiFeO_2$. The OH groups in the structure have been removed for clarity.

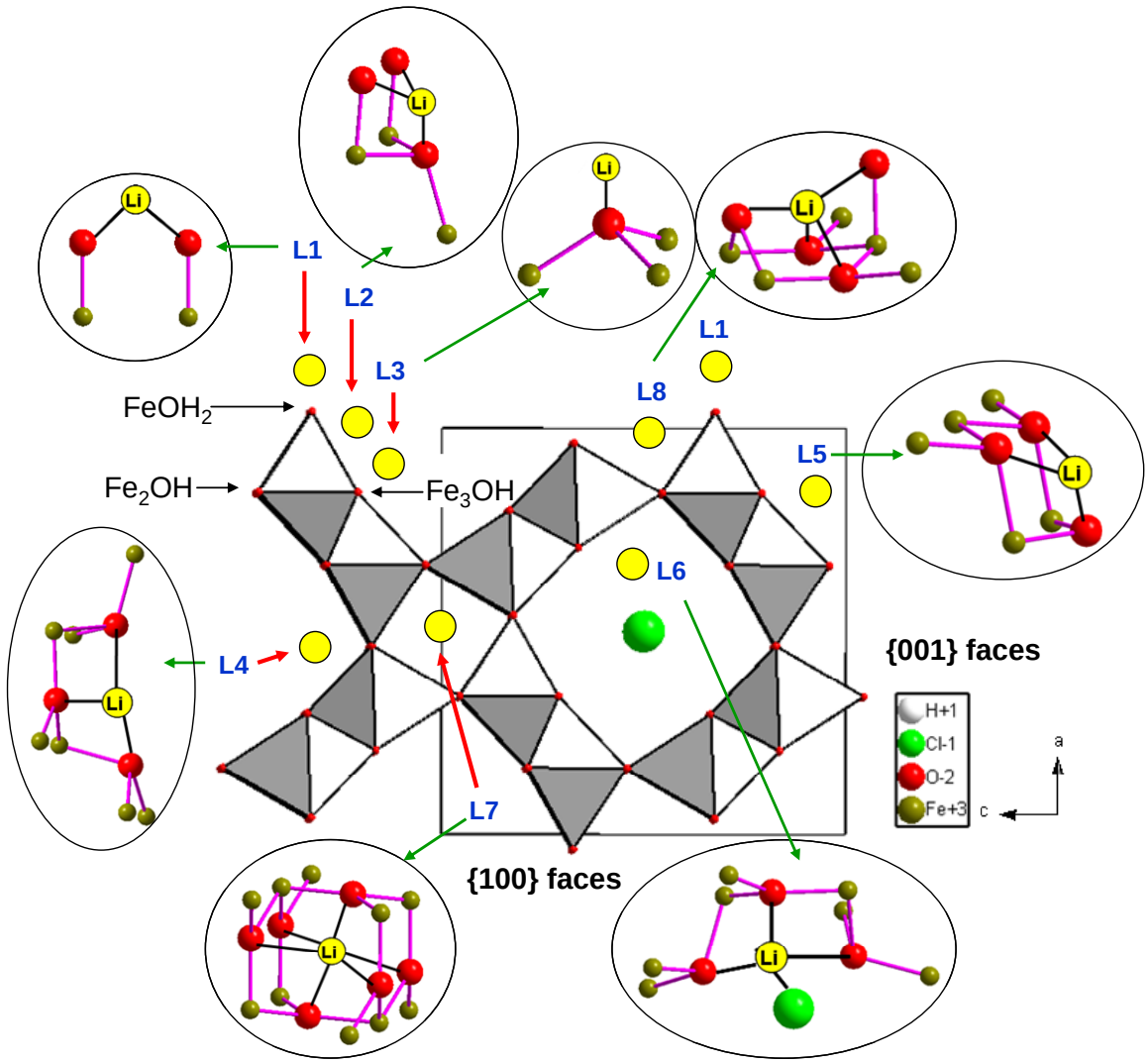

Figure 3.14. Possible positions for the lithium cations on the surface of akaganeite. The proton atoms in the structure and coordinated to the surface bound Li^+ have been removed for clarity. $FeOH_2$, Fe_2OH, and Fe_3OH sites are labeled.

sites	Number of Li-O-Fe bonds	NMR shift (calculated)
L1	2	30
L2	5	75
L3	3	45
L4	9	135
L5	8	120
L6	9	135
L7	18	270
L8	9	≤135

Table 3.1. Calculated hyperfine shifts for possible Li^+ adsorption sites.

3.5 Conclusion

The hydroxyl groups of the paramagnetic iron oxyhydroxide polymorph akaganeite were characterized by ^2H MAS NMR, showing the existence of the rigid OH groups. Lithium binding sites were also quantified and characterized with ^7Li MAS NMR. On the basis of the observed large hyperfine shifts, inner-sphere and outer-sphere complexes were clearly distinguished. In addition, several possible adsorption sites of Li^+ were suggested on the basis of the sizes of the hyperfine shifts as a function of pH. Around neutral pH, Li^+ forms a bidentate complex on the (001) or (100) face (i.e. the edges) of akaganeite. At high pH, Fe_3OH sites on the faces become deprotonated,

resulting in the formations of the monodentate and multidentate complexes involving both oxygen atoms of Fe_3O and FeO groups. The measured Li^+ absorption concentrations on akaganeite were larger by approximately a factor of 20 compared to those seen in our previous study of lepidocrocite.[58] This result is consistent since more $FeOH_2$ and $Fe_3O(H)$ sites are involved in adsorption.

In this contribution, we clearly demonstrate that MAS NMR spectroscopy is a useful technique to study ion binding on systems that are poorly characterized systems due to the difficulties of obtaining in single crystals. Similar NMR approaches can be applied to the study of ion binding modes at water-solid interfaces in other magnetically challenging paramagnetic systems such as those found in alkaline batteries or some water splitting catalysts.

Chapter 4

Phosphate Adsorption on the Iron Oxyhydroxides Goethite (α-FeOOH), Akaganeite (β-FeOOH), and Lepidocrocite (γ-FeOOH): a ^{31}P Solid-state Static NMR Study

Surface adsorption of the phosphate anion on surfaces of the iron oxyhydroxides, goethite, akaganeite, and lepidocrocite was studied to understand adsorption mechanisms at the molecular level due to their environmental importance. In this work, ^{31}P static spin-echo mapping NMR experiments were performed to confirm the formation of an inner-sphere complex of the phosphate anion on iron oxyhydroxide surfaces by observing a signal with a large ^{31}P hyperfine shift in the NMR spectrum. The binding modes and sites of the phosphate anion on these surfaces were characterized in detail on the basis of the observed ^{31}P hyperfine shifts as a function of pH and equilibrium concentrations. To support our analysis of the NMR spectra, adsorption of dimethyl phosphinic acid (DPA) on iron oxyhydroxides was also investigated. Furthermore, ^{31}P NMR spectra of iron phosphate compounds were examined to correlate hyperfine-shift/Fe-O-P bond with magnetic moments (μ_{eff}) of the compounds.

4.1 Introduction

The phosphate anion ($H_2PO_4^-$) is a plant nutrient of major importance. At the same time, it has been recognized as a source of eutrophication in surface water bodies and an agricultural pollutant as an ingredient of fertilizers.[86, 87] The process of phosphating metal surfaces has also been a common practice to protect ferrous or nonferrous metallic materials against oxidative corrosion.[88] In addition, phosphate is a model anion for other toxic oxyanions such as $H_2AsO_4^-$ in environmental studies.

Many studies have reported that iron oxyhydroxides have strong interactions such as phosphate adsorption on their surfaces.[11, 89-92] As a result, iron oxyhydroxides play an important regulatory role for phosphate in the natural aquatic environments. Therefore, understanding the interactions between phosphate and iron oxyhydroxide surfaces at the molecular level is of great importance. There is a consensus that an inner-sphere complex forms via a ligand exchange reaction between phosphate oxygens and hydroxyl oxygens of the surface sites of iron oxyhydroxides.[92-97] An outer-sphere complex is generally thought to form by electrostatic interaction of phosphate anions with $Fe\text{-}OH_2^+$.[11, 98] However, important details concerning the adsorption mechanisms, such as binding modes and specific surface sites, are still not clear despite numerous studies utilizing a variety of techniques including IR[93-96], X-ray absorption spectroscopy[99], computational studies[100, 101], *etc*. Furthermore, the formation of surface precipitates and their identity such as amorphous $FePO_4$, strengite, or phosphosiderite are not also well understood.[93, 96, 98, 102] Solid-state NMR spectroscopy is an element-specific technique and therefore well suited as a tool to probe small anions such as phosphate. The Fermi-

contact (hyperfine) shift, H_{cs}, observed in a NMR spectrum of a paramagnetic material such as FeOOHs occurs through a covalent bond. The size of H_{cs} is determined by the number of Fe^{3+}-O-P bonds. In addition, the size of H_{cs} is directly proportional to a magnetic susceptibility (χ_M) or the square value of magnetic moment (μ_B^2) of a material. (A more detail description of the Fermi-contact shift interaction can be found in our previous work[52, 53, 58] and Chapter 1.) Therefore, solid-state NMR spectroscopy can be useful to investigate the formation of an inner-sphere complex and the local environments of the phosphate on the surface of iron oxyhydroxides. However, solid-state NMR spectroscopy has rarely been applied to studies examining binding modes and sites of small ions on iron (Fe^{3+})-containing systems due to paramagnetically enhanced transverse (T_2) relaxation and challenging magnetic properties.[50, 58, 59] To our knowledge, this work is the first solid-state NMR study of the adsorption modes and sites of the phosphate anion on iron oxyhydroxides, goethite, akaganeite, and lepidocrocite.

In this study, ^{31}P static solid-state NMR spectroscopy was used to probe phosphate ($H_2PO_4^-$) adsorption sites and modes on the surface of the iron oxyhydroxides as a function of pH and phosphate concentration. The results were compared with ^{31}P NMR spectra of several Fe^{3+}-containing phosphate compounds such as $FePO_4$, $Li_3Fe_2(PO_4)_3$, etc. to establish correlations between ^{31}P hyperfine (the Fermi-contact) shifts and μ_{eff}^2 of the materials. In order to explore the effect of monodentate vs. bidentate binding to the surface, ^{31}P NMR spectra of dimethyl phosphinic acid (DPA) adsorbed goethite, akaganeite, and lepidocrocite were also investigated with solid-state ^{31}P NMR spectroscopy since these ligands can only form one P-O-Fe linkage. These

analyses allowed potential sites for phosphate binding on the iron oxyhydroxides to be identified.

4.2 Experimental Section

4.2.1 Sample preparation.

4.2.2 Synthesis of iron oxyhydroxides (FeOOHs)

Goethite (α-FeOOH) was synthesized by dissolving 9.9 g $FeCl_2 \cdot 4H_2O$ (Aldrich) in 1L of distilled water, followed by adding 110 ml of 1M $NaHCO_3$ solution. Air was bubbled through the solution at pH 7 for 48 h at room temperature. The pH was maintained by $NaHCO_3$ buffer during oxidation. The formed goethite was separated by centrifugation, washed with water several times, and dried at room temperature.[60] Akaganeite (β-FeOOH) was prepared by dissolving 10 g of $FeCl_3 \cdot 4H_2O$ (Alfa Aesar) in 40 ml of distilled water. 27.5 ml of 1M NaOH solution was added to the ferric solution. The solution was allowed to stand at room temperature for 2 days and then 7.2 ml of 10 M NaOH was added. The resulting suspension was heated at 70 °C for 8 days. The formed akaganeite was separated by centrifugation, washed with water several times, and dried at room temperature.[60] Lepidocrocite (γ-FeOOH) was purchased from Alfa Aesar.

4.2.3 Phosphate adsorbed iron oxyhydroxides

0.10 g of the as-synthesized iron oxyhydroxide was suspended in 50 ml deionized (DI) water containing the background electrolyte 0.01 M NaCl. The pH of the suspension was adjusted to the desired values (pH 3 – 11) by adding 0.1 M HCl or NaOH. An auto-titrator (Metrohm STAT 718) was used to maintain the adjusted pH constant during phosphate adsorption. A small amount of 50 mM NaH_2PO_4 solution was added to the iron oxyhydroxide suspension to obtain the desired initial phosphate concentration (0.1 – 3 mM) by the other auto-titrator. The iron oxyhydroxide solution was stirred for 15 minutes to equilibrate. (Experiments indicated that 95% of the phosphate was removed from solution by goethite after 5 min.) After the equilibration time, the samples were centrifuged (11000 g, 15 min) to separate the phosphate adsorbed iron oxyhydroxide and supernant. The separated iron oxyhydroxide sample was quickly rinsed with a small amount of deionized water and then air-dried for the NMR measurement. The phosphorus (P) concentration of the supernant was analyzed by DCP-AES (Direct Coupled Plasma-Atomic Emission Spectroscopy) after filtration through 0.22 μm Millex GS-Millipore filters to remove any remaining suspended particles. The amount of the adsorbed phosphate on the iron oxyhydroxide was estimated from the difference between the initial and final P concentration in the solution. On the basis of this data, an adsorption isotherm was obtained at pH 5 as a function of the initial phosphate concentration (0.2 – 3 mM). Another set of adsorption isotherms was obtained at 1 mM initial phosphate concentration as a function of pH (3 – 11). Two extra phosphate adsorbed goethite samples were prepared at 10 mM initial phosphate

concentration and pH 5 and at 50 mM and pH 3, respectively, to investigate the effect of the high initial phosphate concentrations. An extra lepidocrocite sample was also prepared at an adsorption condition of pH 4 and 50 mM initial phosphate concentration.

4.2.4 Adsorption of dimethyl phosphinic acid (DPA) on iron oxyhydroxides

Dimethyl phosphinic acid ($(CH_3O)_2P(O)OH$) adsorbed iron oxyhydroxide samples were prepared by mixing 50 mL of 10 mM DPA with 0.1 g iron oxyhydroxides at pH 3 for 15 minutes. After the equilibration time of 15 min., the suspensions were centrifuged to separate the solid samples from their mother solutions. The obtained solid samples were air-dried and ground to fine powders for the NMR measurement, whereas the supernatant solutions were filtered with a 0.22 μm Millex GS-Millipore filters for DCP-AES analysis.

4.3 Characterization

4.3.1 X-Ray Diffraction (XRD), Transmission Electron Microscope (TEM), BET (Brunauer, Emmett, and Teller) Surface Area, and Magnetic susceptibility

XRD data were collected for all samples on a Rigaku Miniflex XRD bench top X-ray diffractometer (Cr Kα radiation). The measured XRD patterns were converted to 2Θ values corresponding to Cu Kα radiation. All the diffraction patterns were compared with those in the Joint Committee on Powder Diffraction Standards (JCPDS). TEM

images were taken on a FEI BioTwinG^2 Transmission Electron Microscope. BET surface areas for goethite and akaganeite were measured on a Micromeritics ASAP 2010 gas sorption analyzer using N_2 gas. Magnetic properties were studied using a Quantum Design SQUID magnetometer (MPMS XL-5) and Quantum Design Physical Properties Measurement System (PPMS). The temperature dependences of the DC susceptibility ($\chi = M/H$, where M is the magnetization of the sample and H is the applied constant magnetic field) were measured while cooling the sample from 300 to 2 K in a magnetic field of 1000 Oe. Field-cooled (FC) and zero-field-cooled (ZFC) susceptibilities were measured from 300 to 2 K in a magnetic field of 10 Oe. The measured values of magnetic susceptibility (χ_M) at a temperature at which NMR experiments were performed were converted to magnetic moment (μ_{eff}) by using $\mu_{eff} = (8 \times C)^{0.5}$, where C (= $\chi \times T$) is the Curie constant (Table 4.2). (T is a temperature at which a value of χ is taken.)

4.3.2 ^{31}P Static Spin-echo Mapping NMR

^{31}P static spin-echo mapping NMR experiments were performed due to the large line widths observed in the NMR spectra of Fe^{3+}-containinng systems. A Larmor frequency of 80.94 MHz was used on a CMX-200 spectrometer equipped with a Chemagnetics static probe. ^{31}P NMR spectra were referenced to 1M H_3PO_4 at 0 ppm. The NMR measurement consists of recording a series of spectra using a spin-echo pulse sequence, $90°_x$– t – $180°_y$ – t (acquisition), at different irradiation frequencies. The irradiation frequency was increased by 30 kHz steps above and below the ^{31}P resonance of 1M H_3PO_4. The evolution/refocusing times were 25 and 15 μs, respectively. A

typical NMR spectrum in the series was collected using a pulse width of 4 μs. A spin-lattice relaxation (T_1) time (≈ 0.7 ms) of the phosphate adsorbed lepidocrocite sample at 50 mM and pH 4 at a frequency of 81.18 MHz where a peak with a peak maximum is observed was estimated by using an inversion-recovery pulse sequence. A value more than 10 times longer than the T1 time was chosen as a pulse delay (≈ 0.01 s) and used to measure peaks at other frequencies. It was assumed that T_1 times of other samples are similar to 0.7 ms. Phosphate adsorbed goethite samples were measured at 180 ºC. DPA adsorbed goethite samples were measured at 100 ºC to prevent the decomposition of DPA at higher temperatures. Phosphate and DPA adsorbed akaganeite and lepidocrocite samples were measured at room temperature. (The experimental temperatures were chosen to be above the Néel temperature of those compounds.)

4.4 Results and Discussion

4.4.1 Powder X-ray Diffraction (XRD), Transmission Electron Microscope (TEM), BET (Brunauer, Emmett, and Teller) Surface Area, and Magnetic Susceptibility

The XRD powder patterns of the goethite, akaganeite, and lepidocrocite were unambiguously indexed on the basis of the JCPDS files (Figure 4.1–4.4). No significant structural modification was observed in the XRD during the phosphate and dimethyl phosphinic acid adsorptions on the iron oxyhydroxides in the various conditions. This indicates that phosphate adsorption process did not result in any significant long-range structural changes of the iron oxyhydroxide phases.

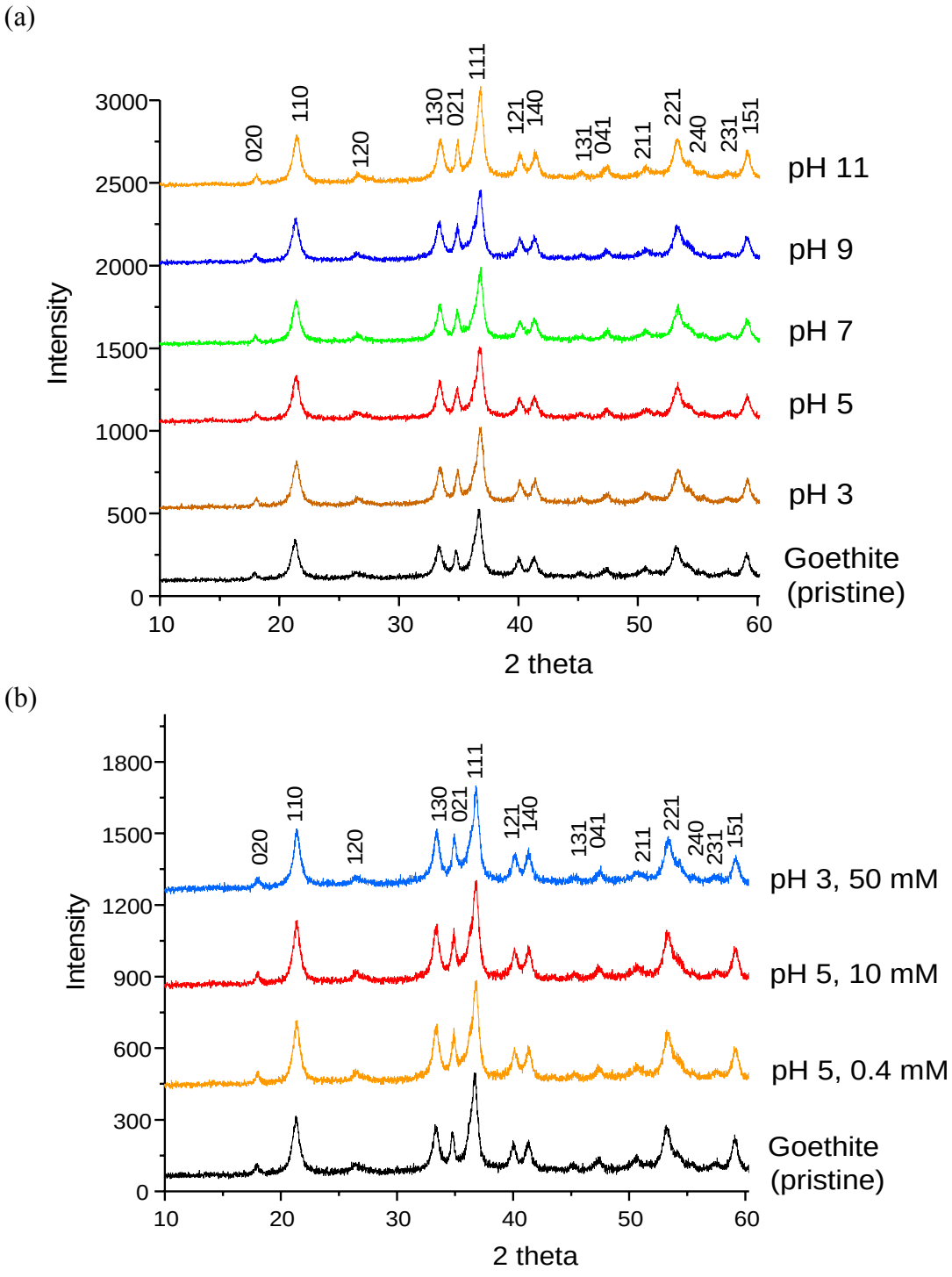

Figure 4.1. X-ray powder diffractions for phosphate-adsorbed goethite samples (a) at 1mM initial phosphate concentration as a function of pH and (b) at various pH values and initial concentrations.

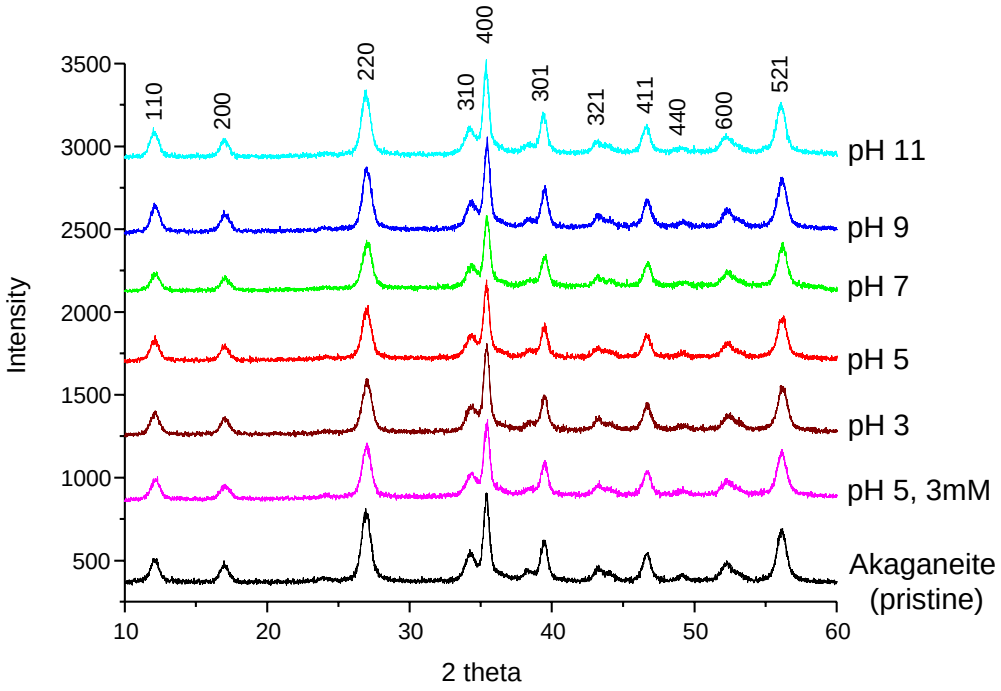

Figure 4.2. X-ray powder diffractions for phosphate-adsorbed akaganeite samples at a 1mM initial phosphate concentration as a function of pH, and at a 3mM initial phosphate concentration and pH 5.

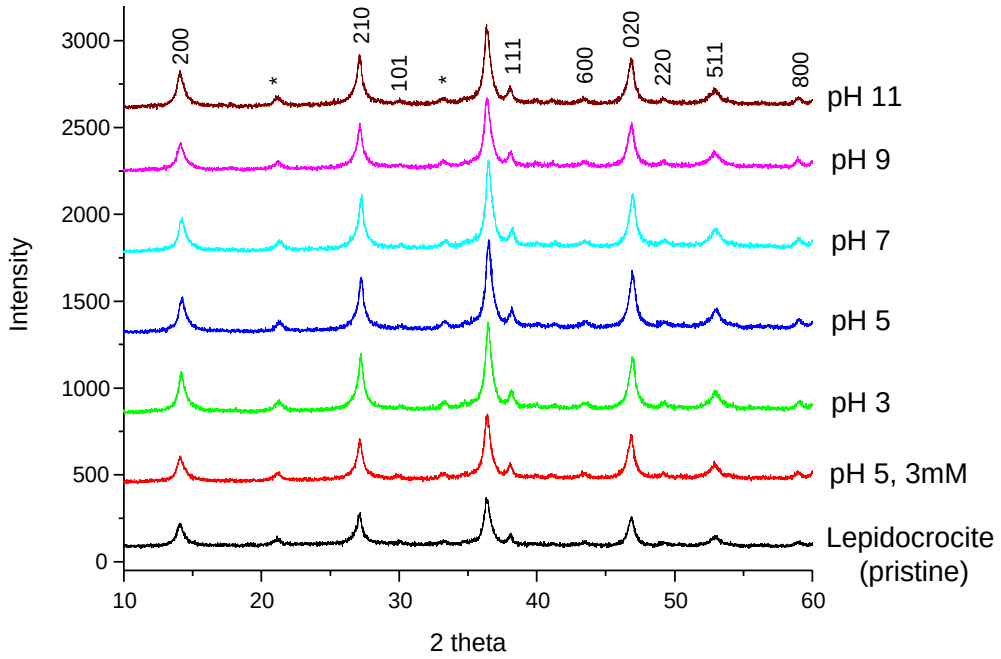

Figure 4.3. X-ray powder diffractions for phosphate adsorbed lepidocrocite samples at a 1mM initial phosphate concentration as a function of pH and at a 3mM initial phosphate concentration and pH 5. (*) denotes the reflection due to the goethite impurity, present in all the samples.

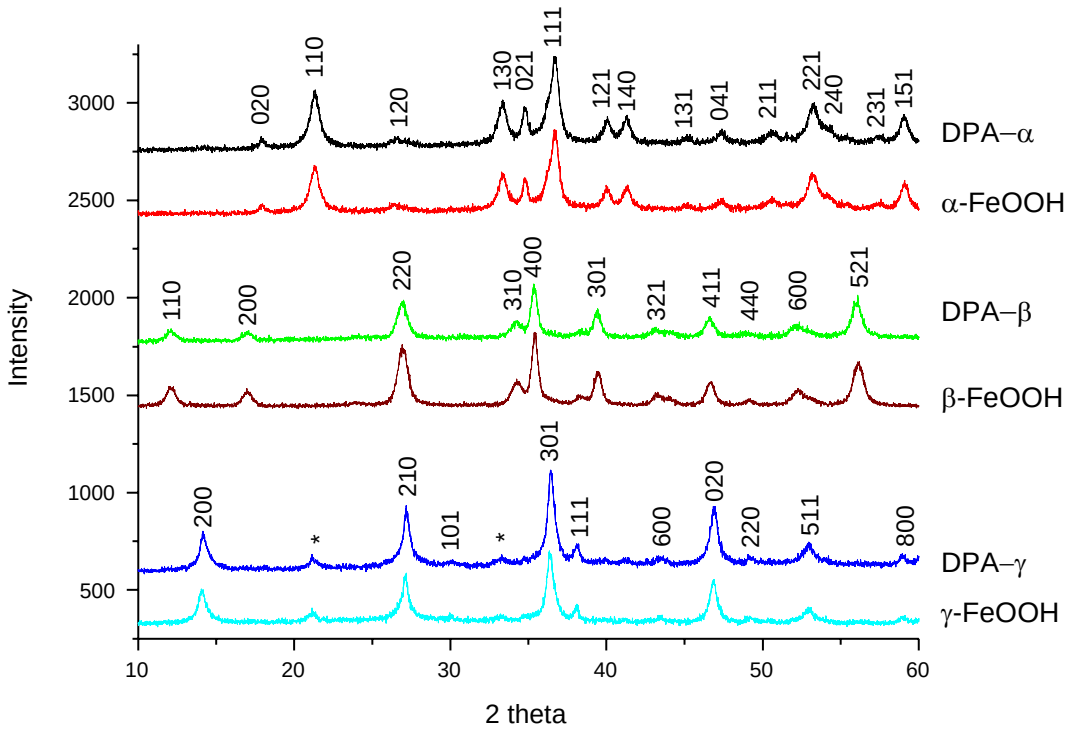

Figure 4.4. X-ray powder diffractions for dimethyl phosphinic acid (DPA) adsorbed FeOOH samples at a 10 mM initial phosphate concentration and pH 5. (*) denotes the reflection due to the goethite impurity. The DPA-sorbed goethite, akaganeite, and lepidocrocite samples were labeled as DPA-α, DPA-β, and DPA-γ, respectively.

TEM images of the synthesized goethite sample show needle like shapes, 122 - 148 nm in length and 7.6 – 15.7 nm wide (Figure 4.5 (a)), consistent with previously reported data.[1, 68] The akaganeite sample shows cigar-like shapes 76 nm in length and 11.5 nm wide (Figure 4.5 (b)).[1, 22] The morphology of lepidocrocite (Alfa Aesar), which is the same sample used here, was previously reported to show needle shapes 300 nm in length and 2 nm wide.[58] Goethite and akaganeite show BET surface areas of 63 and 94 m^2/g, respectively. A BET surface area of lepidocrocite was reported as 85 m^2/g also in our previous work.[58]

(a)

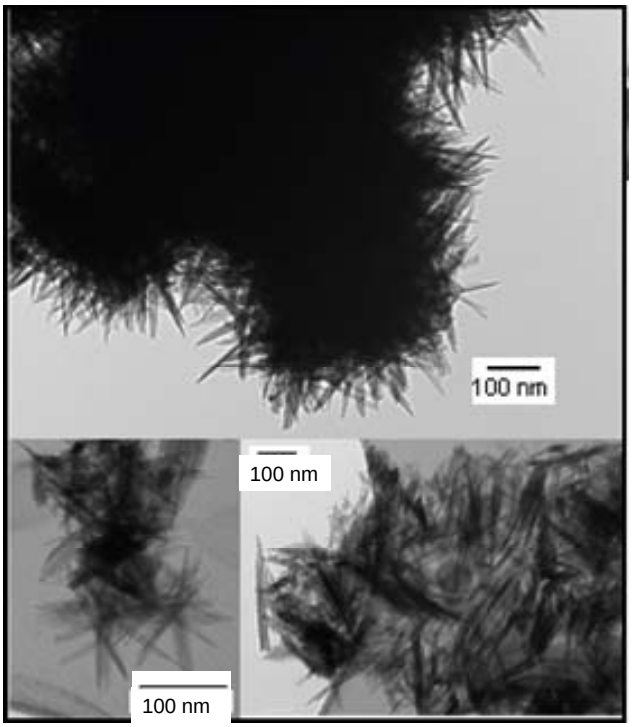

(b)

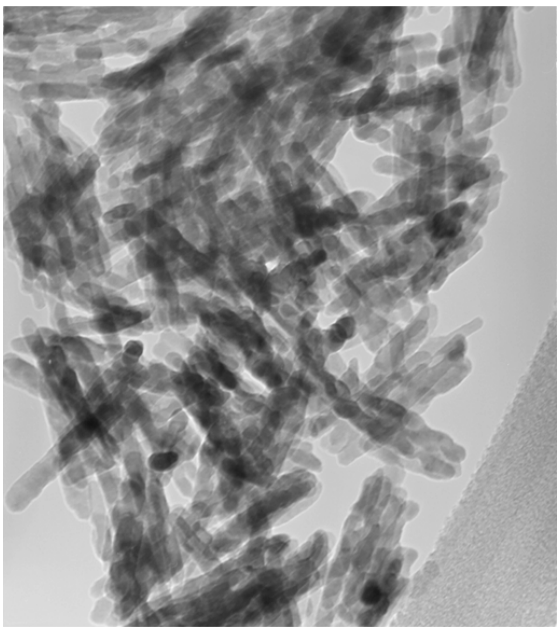

Figure 4.5. Transmission Electron Microscope (TEM) images of (a) goethite and (b) akaganeite.

DC susceptibility measurement of goethite shows two very broad features at 25 K and 325 K (Figure 4.6 (a)). The peak at about 25 K is assigned to a small amount of ferrihydrite impurities in the goethite sample, as ferrihydrite is known to have a blocking temperature of 25 to 115 K.[1] The second peak at about 325 K is caused by an antiferromagnetic transition of the goethite particles. We did not measure the magnetic susceptibility up to the highest temperature where the NMR experiments were performed, 450 K, due to the instrumental limitations (Figure 4.6 (a)-(b)). Therefore, the previously reported value of magnetic susceptibility at 450 K was converted to a value for the magnetic moment of 3.06 μ_B.[103] A FC-ZFC curve of akaganeite sample shows two broad peaks at 65 and 252 K (Figure 4.6 (b)). The peak at 65 K is due to a small amount of lepidocrocite impurity not detected by XRD measurements. Lepidocrocite reportedly shows a magnetic transition around 77 K.[1, 68] The other peak at 252 K is from antiferromagnetic ordering of akaganeite particles, consistent with the previously reported data.[1, 83] The magnetic moment of this sample was estimated to be 2.20 μ_B at room temperature. The lepidocrocite sample shows a broad peak at 35 K in a FC-ZFC curve, caused by an antiferromagnetic transition (Figure 4.6 (c)), which occurs at a lower magnetic transition temperature than the previously reported data. This lepidocrocite sample was estimated to have a magnetic moment of 3.22 μ_B at room temperature.

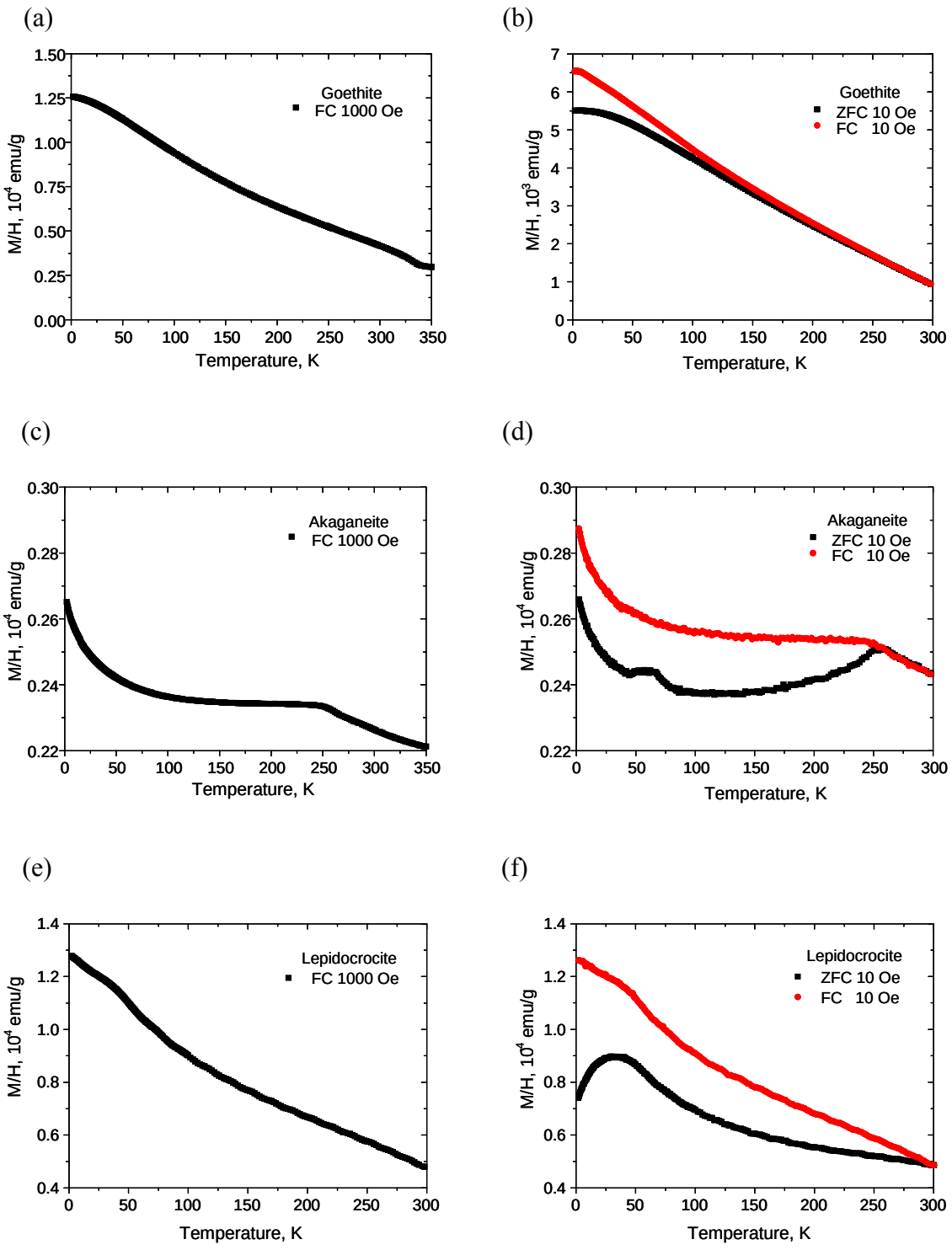

Figure 4.6. Magnetization curves of (a-b) goethite, (c-d) akaganeite, and (e-f) lepidocrocite. Left side: DC susceptibility measurements at 1000 Oe. Right side: FC-ZFC measurements at 10 Oe.

4.4.2 Phosphate Adsorption Data

Figure 4.7 shows adsorption isotherms for the orthophosphate ($H_2PO_4^-$) on goethite, akaganeite, and lepidocrocite. Two sets of adsorption isotherms were obtained (1) at pH 5 as a function of equilibrium phosphate concentrations (left side in Figure 4.7) and (2) at 1 mM of phosphate concentration as a function of pH (right side in Figure 4.7) for each iron oxyhydroxide, respectively. As the equilibrium phosphate concentration increases from 0.1 mM to 3 mM at pH 5, the amount of adsorbed phosphate increases exponentially. Goethite shows a maximum adsorption of about 266 μmol/g at the highest equilibrium concentration used (3 mM), which is similar to the previously reported adsorption capacity.[94] Akaganeite and lepidocrocite show 450 and 265 μmol/g at 3 mM of the equilibrium concentration, respectively, but both of these adsorptions do not appear to have reached a maximum. The adsorption capacities on goethite, akaganeite, and lepidocrocite were estimated with their surface areas to be 2.54, 2.88, and 1.88 phosphate anions/nm^2, respectively. The akaganeite sample has a higher surface area than those of goethite and lepidocrocite, and so it is reasonable that the akaganeite sample shows the highest adsorption capacity among them. Even though lepidocrocite sample has a higher surface area than goethite sample, it shows a similar amount of phosphate adsorption capacity, at least with these phosphate concentrations. These results suggest that the reactive surface planes for phosphate adsorption on lepidocrocite are not the major surfaces (010). This analysis is consistent with our NMR data, which will be shown below. The amount of phosphate adsorption on the iron oxyhydroxides decreases in a 1 mM phosphate solution with increasing pH, as previously reported for similar

experiments on goethite[11, 98], akaganeite[11], ferrihydrite[95], magnetite[88], *etc*. Of particular note is the dramatic decrease in adsorption capacity just above pH 7. This is mainly due to electrostatic repulsions between negatively charged surfaces of iron oxides above the point of zero charge (PZC ≈ 7) and multivalent phosphate anions in a high pH solution.[9, 11, 13, 58, 59, 80, 98]

(a)

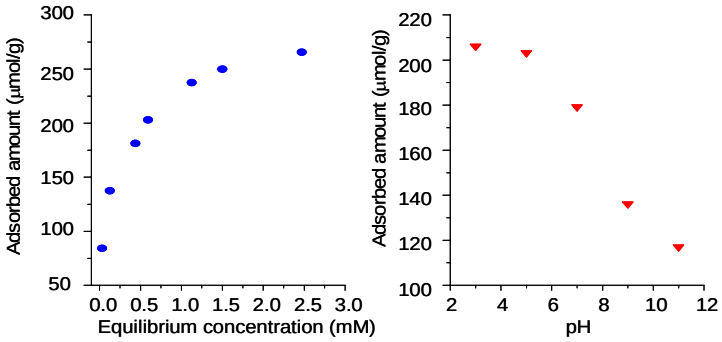

(b)

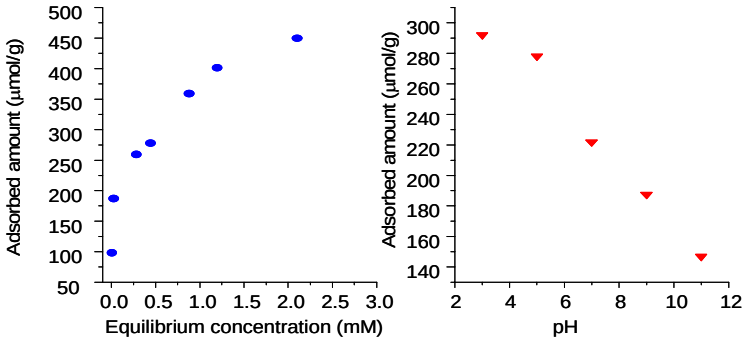

(c)

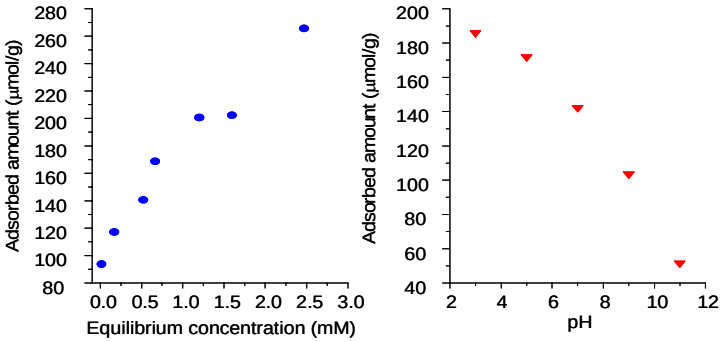

Figure 4.7. Adsorption isotherms of phosphate on the surface of (a) goethite, (b) akaganeite, and (c) lepidocrocite. (Left) phosphate adsorption at pH 5 as a function of initial phosphate equilibrium concentrations. (Right) phosphate adsorption from a 1 mM phosphate solution as a function of pH.

4.4.3 Solid-State NMR

4.4.3.1 ^{31}P NMR of phosphate adsorbed goethite, akaganeite, and lepidocrocite

In this work, adsorptions of phosphate anion on the iron oxyhydroxides (α-, β-, and γ-FeOOHs) were investigated with ^{31}P solid-state NMR as a function of pH and equilibrium phosphate concentrations. Very broad and asymmetric spectral line shapes with about 6000 – 8000 ppm line width are often observed for all the phosphate adsorbed FeOOH samples due to a strong dipolar coupling between unpaired electrons of the Fe^{3+} atom and a ^{31}P nuclear spin and possibly different environments of the bound phosphate ions (Figure 4.8-4.11). A similar spectral width was previously reported for Fe^{3+}-substituted $AlPO_4$.[47] The phosphate adsorbed FeOOH samples show different overall line shapes, depending on the adsorption conditions and adsorbents in their NMR spectra (Figure 4.8-4.11). This is tentatively ascribed to the different protonation states of the adsorbed phosphate anion, different dipolar interactions between an unpaired electronic spin on Fe^{3+} atom and phosphorus nucleus in space, and binding to different sites. In particular, akaganeite samples show notably different line shapes from those of goethite and lepidocrocite samples, due to either surface termination effects that result in higher a magnetic moment or larger dipolar coupling with surface due to binding arrangement and shape. For a more in depth understanding of the influences of phosphate protonation and surface defects on observed line shapes, further investigations are required and are in progress. The phosphate-adsorbed FeOOH samples show that the intensities of the observed peaks are inversely proportional to pH at which the adsorption experiments were performed, but directly dependent on the phosphate concentrations (Figure 4.8-

4.11). This tendency is consistent with the observed adsorption isotherms of those samples (Figure 4.7).

Phosphate adsorbed goethite samples show a peak with a peak maximum at 2600 (±100) ppm over a wide range of phosphate concentrations (0.4 – 10 mM) at pH 5 and at 50 mM and pH 3 (Figure 4.8). The increased peak intensity is observed as the phosphate concentration increases from 0.4 mM to 10 mM. A peak at 2550 (±150) ppm is also observed in adsorption conditions from pH 3-9 at 1 mM phosphate concentration (Figure 4.9).

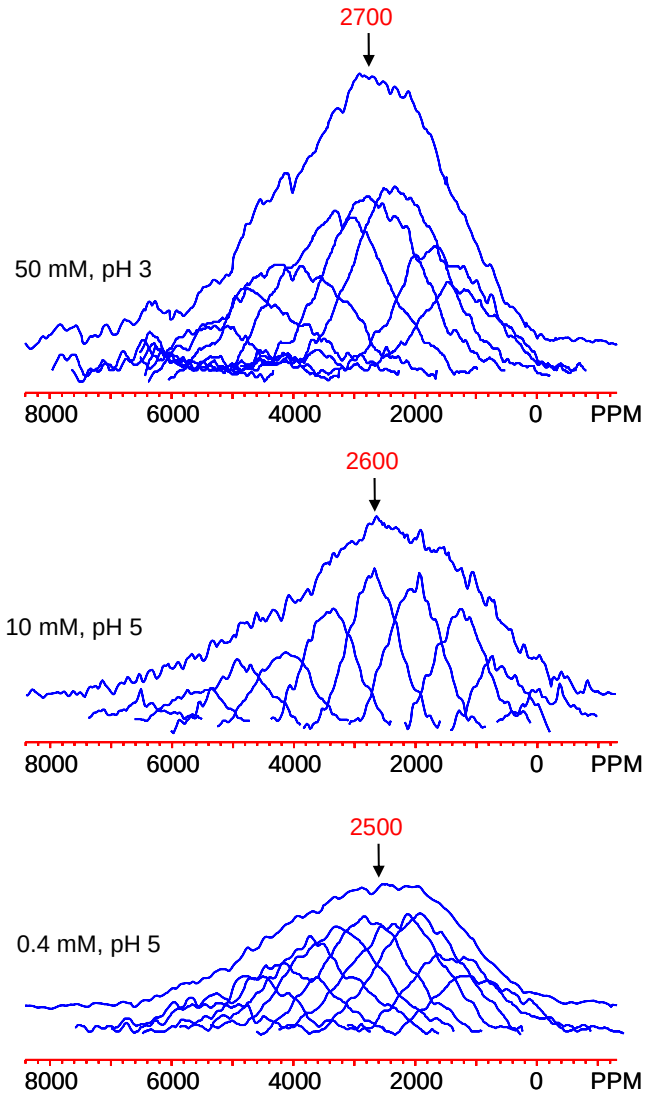

Figure 4.8. Spin echo mapping ^{31}P NMR spectra of phosphate-adsorbed goethite at various phosphate concentrations and pH. The NMR spectra of 0.4 and 10 mM samples are normalized by the acquisition number used in their measurements.

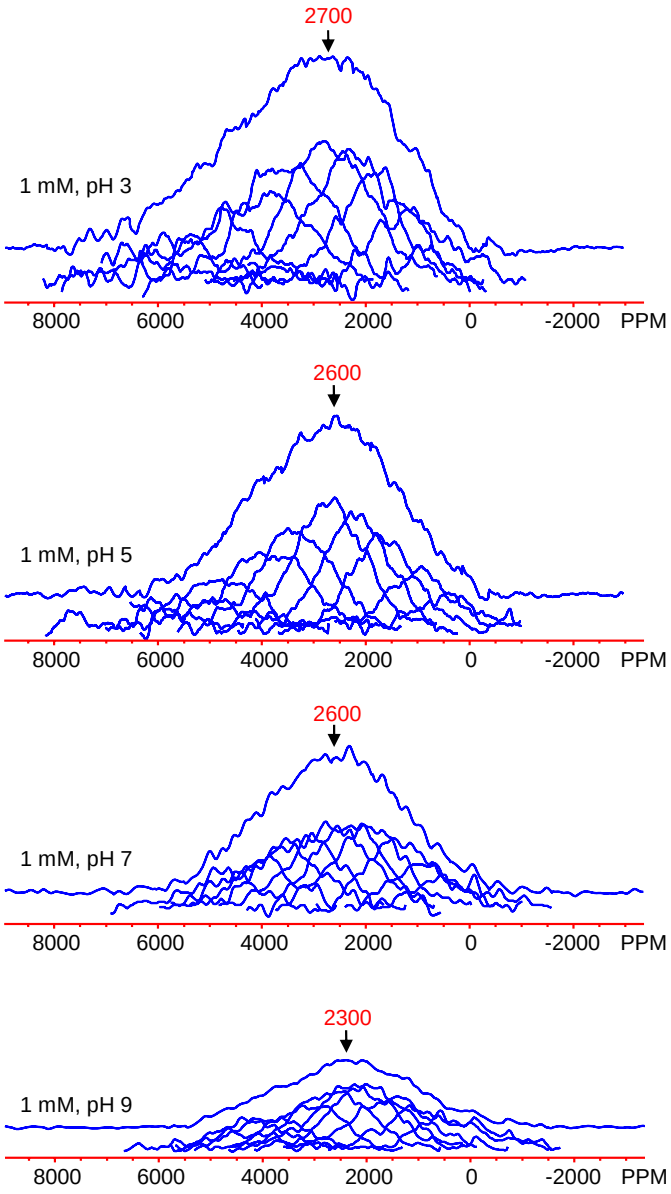

Figure 4.9. Spin echo mapping ^{31}P NMR spectra of phosphate adsorbed goethite at a 1mM phosphate concentration as a function of pH. The NMR spectra of pH 3 and 5 samples are normalized with respect to each other by the acquisition number used in their measurements; the NMR spectra of pH 7 and 9 samples are normalized as well, with respect to each other.

Phosphate-adsorbed akaganeite samples at pH 3, 5, 7, and 9 in 1 mM of the phosphate solution show a broad resonance with a peak maximum at 1100 (±200) ppm (Figure 4.10). The phosphate-adsorbed akaganeite sample at pH 5 and 3 mM the phosphate concentration shows two peaks with a peak maximum at about 0 (±30) ppm and 1100 (±200) ppm (Figure 4.10). This peak with the smaller shifted (≈ 0 ppm) is assigned to diamagnetic impurities such as outer sphere sorbed phosphate molecules that remain even after filtration and washing with deionized water.

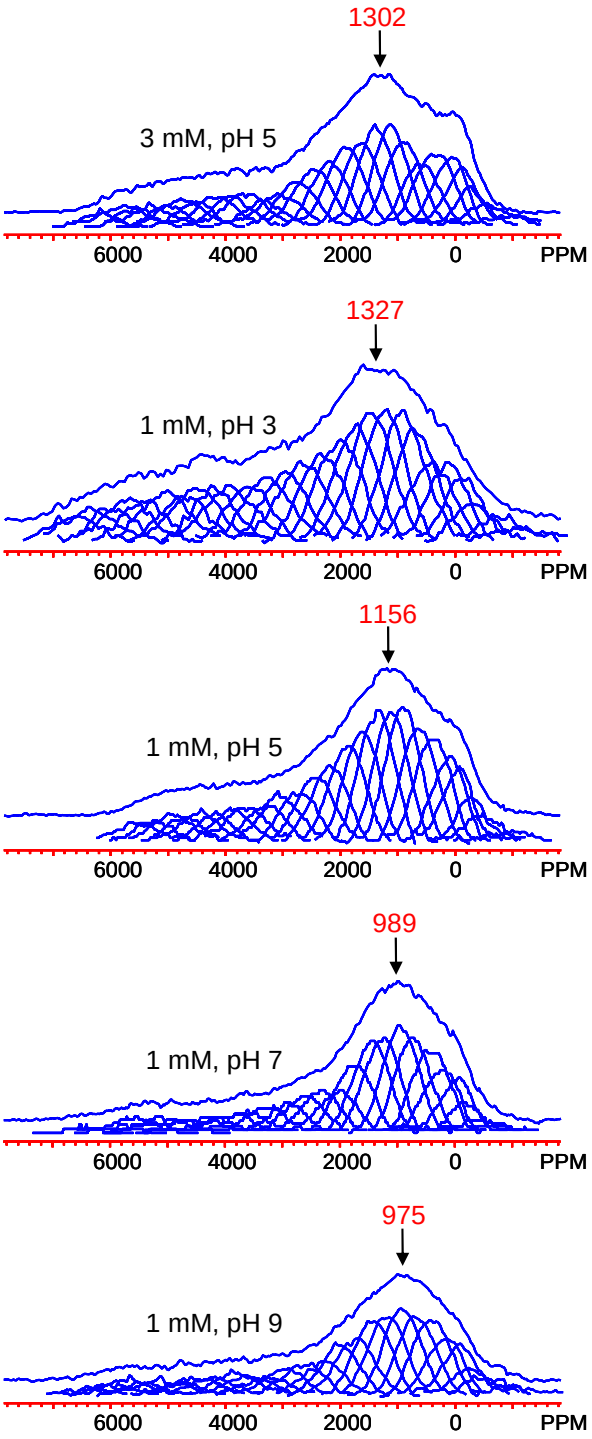

Figure 4.10. Spin echo mapping ^{31}P NMR spectra of phosphate adsorbed akaganeite at a 3mM phosphate concentration and pH 5 and as a function of pH at a 1mM phosphate concentration. The NMR spectra, except for pH 3 sample, are normalized with respect to each other by the acquisition number used in their measurements.

Phosphate adsorptions on lepidocrocite show a broad peak with a peak maximum at about 2600 (±200) at pH 3, 5, 7, and 9 in 1 mM phosphate solution (Figure 4.11). Similarly, hyperfine shifted peaks are observed at 3000 and 2700 ppm for phosphate adsorbed samples at pH 4 in a 50 mM phosphate solution and pH 5 in a 3 mM phosphate solution, respectively (Figure 4.11).

The slightly increased hyperfine shifts often observed in the phosphate-adsorbed FeOOH samples, which are proportional to phosphate concentration, but inversely to pH, are tentatively ascribed to the stronger binding of the phosphate anion under more favorable adsorptive conditions, such as higher phosphate concentration and lower pH (Figure 4.8-4.11). These large hyperfine shifts confirm the existence of an inner-sphere complex of the phosphate on the surface of iron oxyhydroxides.

Strengite and phosphosiderite have been proposed as the most commonly formed precipitate species on iron oxyhydroxide surfaces.[93, 96, 98, 102] The ^{31}P NMR spectra of these compounds show peaks with a peak maximum at about 15800 ppm and 16680 ppm, respectively (Table 4.1).[104] There was no obvious signal above 8000 ppm for the phosphate adsorbed iron oxyhydroxide samples previously discussed, indicating no such precipitate formation at the surface in our adsorption experiments.

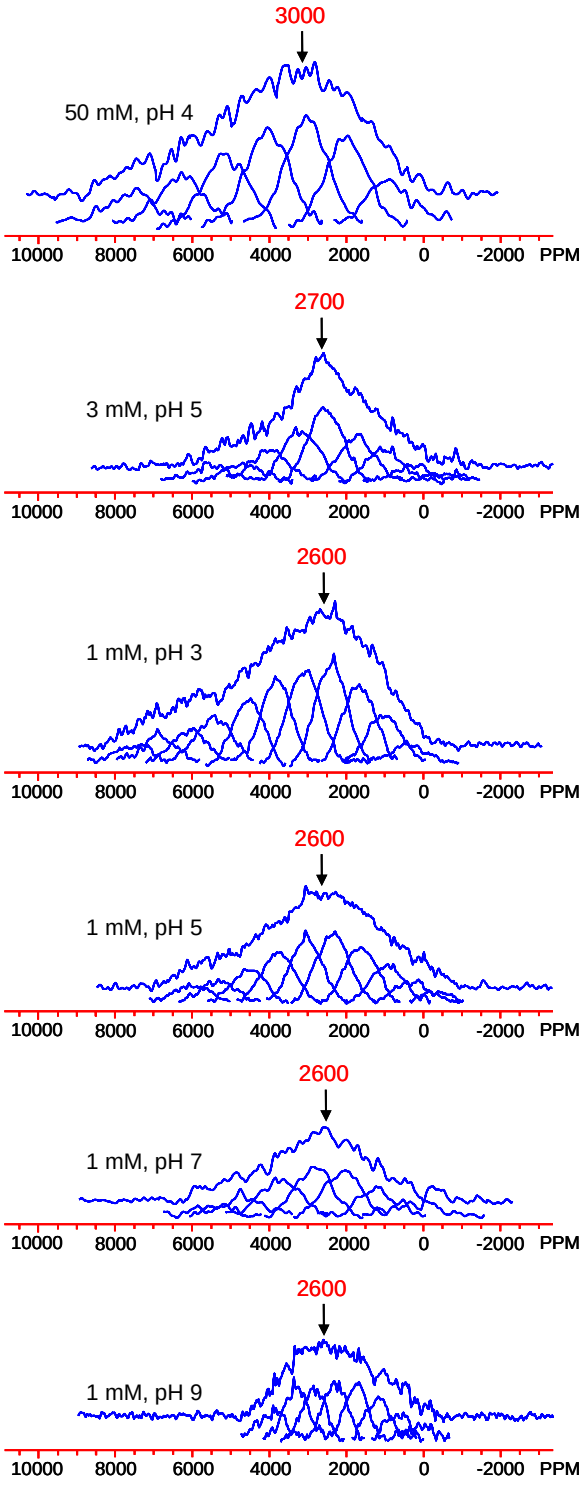

Figure 4.11. Spin echo mapping ^{31}P NMR spectra of phosphate adsorbed lepidocrocite at pH 4 and 50 mM initial phosphate concentration, pH 5 and 3mM initial phosphate concentration, and 1mM phosphate concentration as a function of pH. The NMR spectra, except for 50 and 3 mM samples, are normalized with respect to each other by the acquisition number used in their measurements.

4.4.3.2 Magnitude of hyperfine shift per Fe^{3+}-O-P bond in ^{31}P solid-state NMR spectra from model compounds

The magnitude of hyperfine shift depends on the square value of magnetic moment, μ_{eff}^2 (in unit of Bohr magneton) or magnetic susceptibilities, χ (in unit of emu/mol·Oe). Therefore, it is possible to predict the magnitude of the contribution per Fe^{3+}-O-P bond to the overall observed hyperfine shifts for each oxyhydroxide based on the Fermi-contact shifts of Fe^{3+}-containing model compounds with a well characterized structure and magnetic property. In this study, we chose model compounds including heterosite ($FePO_4$), rhombohedral $Li_3Fe_2(PO_4)_3$, monoclinic $Li_3Fe_2(PO_4)_3$, phosphosiderite (monoclinic $FePO_4 \cdot 2H_2O$), strengite (orthorhombic $FePO_4 \cdot 2H_2O$), and dehydrated phosphosiderite and strengite. The observed hyperfine shifts per Fe^{3+}-O-P bond, the magnetic moments, μ_{eff}, and magnetic susceptibilities, χ of these compounds are summarized in Table 4.1. (A more detailed study on these iron phosphate compounds will be reported in Chapter 5.) Two plots of the μ_{eff}^2 values and χ of the model compounds verses their observed ^{31}P NMR hyperfine shifts are reported in Figure 4.12 (a) and (b), respectively. The μ_{eff}^2 values show better correlation with the observed ^{31}P NMR hyperfine shifts than χ. However, that χ shows a weak correlation with the observed ^{31}P NMR hyperfine shifts is not clearly understood. (The correlations between χ and the observed hyperfine shifts are investigated by considering A (the hyperfine coupling constant) in equation [1.23] with periodic density functional theory (DFT) calculations in the subsequent chapter.) In this chapter, the plot of the μ_{eff}^2 values verses

their observed ^{31}P NMR hyperfine shifts was used to yield the following correlation function:

$$\delta_{iso}/\ Fe^{3+}\text{-O-P bond} = 115 \times \mu_{eff}^2 \qquad [4.1]$$

From this equation [4.1], goethite, akaganeite, and lepidocrocite are expected to contribute 1074, 555, and 1190 ppm per Fe^{3+}-O-P bond, respectively (Table 4.2).

(a)

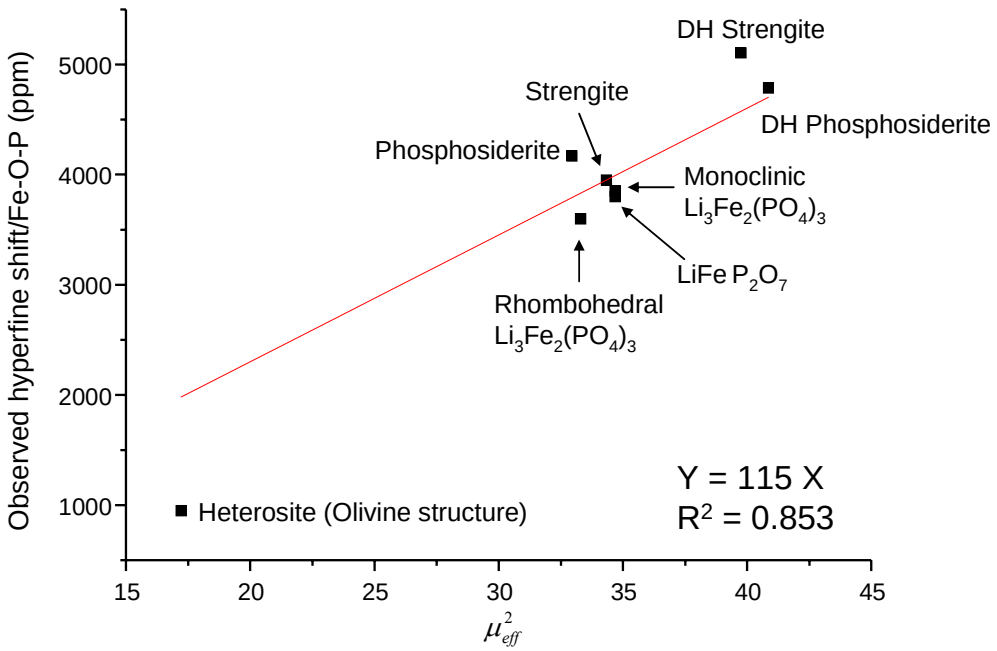

(b)

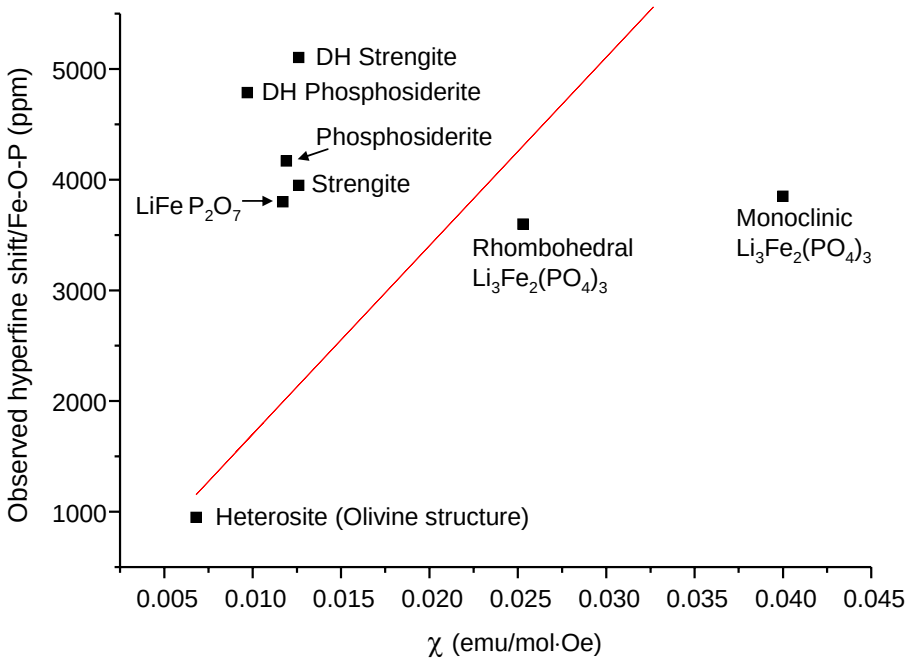

Figure 4.12. The correlation of the observed hyperfine shifts of iron phosphates with (a) the square value of their μ_{eff} (in unit of Bohr magneton) and (b) magnetic susceptibilities, χ (in unit of emu/mol·Oe).

	μ_{eff}	χ (emu/mol·Oe)	Observed δ_{iso} (ppm)[104, 105]	no. of Fe-O-P bonds	δ_{iso}/Fe-O-P (ppm)
Heterosite	4.15[106]	6.80×10^{-3}	5770	6	950
Phosphosiderite	5.74[104]	1.19×10^{-2}	16680	4	4170
Rhombohedral $Li_3Fe_2(PO_4)_3$	5.77[107]	2.53×10^{-2}	14350	4	3600
Strengite	5.86[104]	1.26×10^{-2}	15800	4	3950
Monoclinic $Li_3Fe_2(PO_4)_3$	5.89[107]	4.0×10^{-2}	14230 15250 16200	4 4 4	3600 3875 4075
Dehydrated (DH) strengite	6.31[108]	1.08×10^{-2}	19149	4	5106
Dehydrated (DH) phosphosiderite	6.39[108]	9.70×10^{-3}	20426	4	4787
$LiFeP_2O_7$	5.89[109]	1.17×10^{-2}	8500 14943	3	2833 4766

Table 4.1. Summary of the observed hyperfine shift per Fe-O-P bond of iron (III) phosphate compounds with their magnetic moment, μ_{eff} (in unit of Bohr magneton) and magnetic susceptibility, χ (emu/mol·Oe).

	χ (10^{-6} emu/g·Oe)	μ_{eff}	Calculated δ_{iso}/Fe-O-P (ppm)
α-FeOOH	29	3.06[103]	1074
β-FeOOH	22	2.20	555
γ-FeOOH	49	3.22	1190

Table 4.2. Predicted hyperfine shifts for the α, β, and γ-FeOOH polymorphs per Fe-O-P bond. The values of magnetic moments, μ_{eff} (in unit of Bohr magneton) were estimated from magnetic susceptibility data, χ (emu/g·Oe) at a temperature at which NMR experiments were performed. The magnetic moment (μ_{eff}) of goethite was obtained by using the previously reported magnetic susceptibility, χ (emu/g·Oe).[103]

To increase the level of confidence of our analysis of the measured NMR spectra of the phosphate adsorbed iron oxyhydroxides, adsorptions of dimethyl phosphinic acid (DPA) on goethite, akaganeite, and lepidocrocite were investigated with solid-state ^{31}P NMR spectroscopy. DPA is expected to form a monodentate complex on the surface of the iron oxyhydroxides because the oxo group (P=O) of DPA molecule is unreactive and will not bind to the Fe^{3+} ions on the surface. There are several studies on the adsorption of organic phosphates with a single OH group, similar to DPA, such as adsorption on the surface of goethite and TiO_2.[110, 111] In these infrared (IR) spectroscopy and theoretical studies, phosphodiester group, which has one oxo group (P=O) and one hydroxyl group (P-O), is reportedly bound to the surface of goethite by forming a monodentate complex.[110] Dimethylarsinic acid ($(CH_3)_2As(O)OH$) was also reported to form an monodentate complex on TiO_2 by an investigation with X-ray absorption spectroscopy (XAS).[111] DPA adsorbed goethite, akaganeite, and lepidocrocite show peaks with a peak maximum at about 1150, 550, and 1600 ppm, respectively. The magnitudes of these observed hyperfine shifts are almost half those seen for the phosphate anion adsorbed on the goethite, akaganeite, and lepidocrocite, correspondingly. From these results, we estimate that one Fe^{3+}-O-P bond contributes 1150, 550, and 1600 ppm to the hyperfine shifts in ^{31}P NMR spectra of goethite, akaganeite, and lepidocrocite, respectively. Furthermore, we can confirm that the observed NMR signals of the phosphate anion adsorbed samples are from inner sphere adsorption and not from the presence of precipitates.

From the analyses of the model systems, we can conclude that one Fe^{3+}-O-P interaction contributes a shift of 1074-1150, 550-555, and 1190-1600 ppm for goethite,

akaganeite, and lepidocrocite, respectively, where again these quoted values correspond to the peak maximum of a broad line shape.

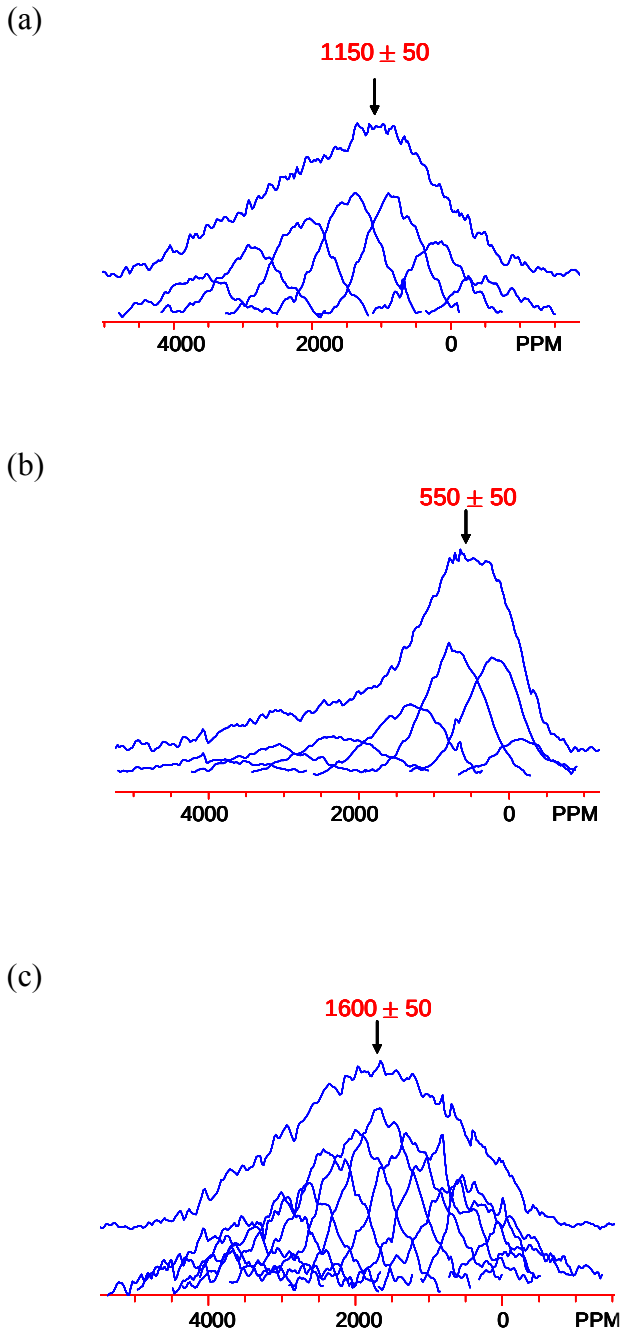

Figure 4.13. ^{31}P NMR spectra of dimethyl phosphinic acid (DPA) adsorbed goethite (a), akaganeite (b), and lepidocrocite (c) samples at a 10 mM initial phosphate concentration and pH 5.

4.4.3.3 Binding modes and sites of the phosphate anion on the surfaces of goethite, akaganeite, and lepidocrocite

On the basis of predicted hyperfine shifts per Fe-O-P bond, we propose the existence of two Fe-O-P interactions on the surface of the FeOOHs used in this study. Therefore, the phosphate ion primarily forms a bidentate adsorption complex on the surface of oxyhydroxides (Figure 1.2). In addition, though many phosphate adsorption studies have reported possible changes in phosphate binding modes at the iron oxyhydroxide surface as a function of pH and phosphate concentration, obvious effects of pH and the concentration on the binding mode of phosphate were not observed in this study. We therefore conclude that the bidentate phosphate adsorption complex is a stable adsorption mode for a wide range of pH and phosphate concentrations.

Unlike cation adsorption on the surface, phosphate adsorption involves a ligand exchange reaction as previously mentioned, in which a Fe-O(H) bond is broken and a new Fe-O-P bond is formed.[92-97] Considering the most reactive sites on the surface with respect to the phosphate anion, the $Fe_3O(H)$ and Fe_2OH sites may be ruled out since these sites require that two or three Fe-O bonds are broken for phosphate adsorption and there is little likelihood of this occurring under the mild adsorption conditions used in this study. This leaves only the $FeOH_2$ surface sites. Based on the location of these $FeOH_2$ groups, we can propose the most reactive sites for phosphate adsorption on each FeOOH polymorph.

In goethite, several possible binding sites are proposed, G1 to G5, for bidentate adsorption as depicted in Figure 4.14 (a). Binding sites, G1 and G5, will be unfavorable

for phosphate adsorption on the surface because they involve $Fe_3O(H)$ and Fe_2OH sites. Therefore, G2, G3, and G4 are considered as possible binding sites. The G2 site is on the (101) plane, which is a major surface face, while the G3 and G4 sites are located on the (210) plane (a minor plane). Taking this into consideration, we propose that the G2 site is a major phosphate adsorption site and the G3 and G4 sites are minor phosphate adsorption sites.

Akaganeite is also expected to have several possible adsorption sites, A1 to A5, as depicted in Figure 4.14 (b). The A1 and A2 sites involve $Fe_3O(H)$ and Fe_2OH sites and are therefore unfavorable for adsorption. As a result, three possible binding sites, A3, A4, and A5 are predicted to be more favorable for the phosphate adsorption. The A3 site is on the major (001) or (100) plane and the A4 and A5 sites are located on the (010) plane. On the basis of this reasoning, we predict that A3 site is a major binding site of the phosphate. Not to overlook possible phosphate binding inside the tunnel, previous work reported the phosphate anion to be too large to enter the tunnels of goethite and akaganeite.[11] Furthermore, all of the binding sites within the tunnel are composed of $Fe_3O(H)$ groups and can not bind the phosphate anion as an inner-sphere complex easily.

Lepidocrocite shows three possible bidentate adsorption sites, L3, L4, and L5. L3 and L5 are located on the (100) plane and L4 is located on the (001) plane, as depicted in Figure 4.14 (c). The O-O distance at L3 binding site is 3.88 Å, indicating that a P-OFe bond distance of 1.94 Å is required if a close-to-linear O-P-O linkage is formed at the L3 site.[29] The typical P-OFe bond distance is 1.57 – 1.59 Å.[100] Therefore, phosphate is unlikely to form a stable bidentate complex at the L3 site. Hence, we anticipate that the L4 and L5 sites will play a major role in binding phosphate on the lepidocrocite surface.

L1 and L2 sites involve $Fe_3O(H)$ and Fe_2OH, respectively, and are excluded as they are unfavorable binding sites.

(a)

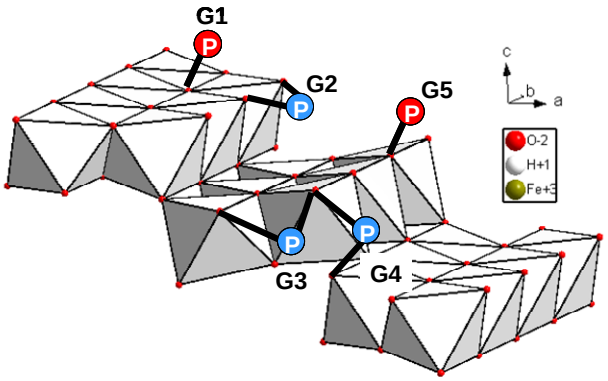

(b)

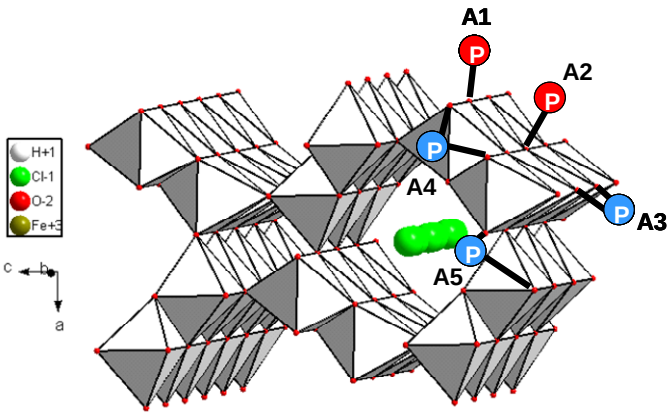

(c)

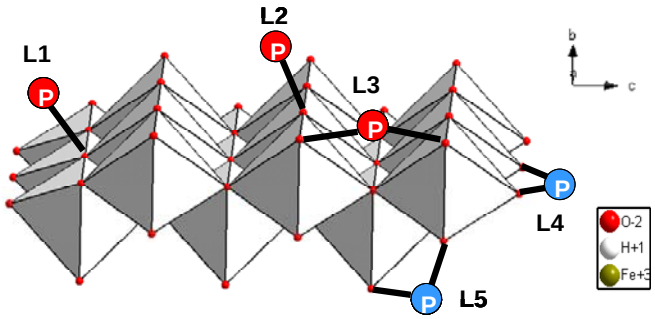

Figure 4.14. The possible adsorption sites on the surface of (a) α-FeOOH, (b) β-FeOOH, and (c) γ-FeOOH. The colored balls represent adsorbed phosphate. Red-colored balls represent an unfavorable binding site. Blue-colored balls represent a favorable site. For clarity the non-bonded oxygen atoms of the phosphate ions are omitted.

Our models for phosphate anion adsorption on the iron oxyhydroxides are well matched with the previously reported models of As^{5+} anion adsorption on them, investigated via EXAFS (extended X-ray absorption fine structure) spectroscopy.[74, 112, 113] In these studies, goethite adsorbs the As^{5+} anion via the formation of a binuclear bidentate complex on (101) plane as we proposed for binding modes of the phosphate anion.[113] Akaganeite also adsorbs the As^{5+} anion by forming a binuclear bidentate complex on (100) and (001) planes.[113] Finally, the As^{5+} anion forms a binuclear bidentate complex on the (100) and (001) surface planes of lepidocrocite.[112, 113]

4.5 Conclusion

In this work, phosphate adsorption on the surface of goethite, akaganeite, and lepidocrocite were investigated at the molecular level. The formation of an inner-sphere complex of phosphate on the surfaces of the various iron oxyhydroxides was confirmed by the existence of large hyperfine shifts observed in the ^{31}P NMR spectra of the phosphate adsorbed compounds. Furthermore, a binuclear bidentate complex was proposed to be the predominant binding mode on the surfaces of various compounds. It was found that the (101) and (210) planes on goethite, the (100) and (001) planes on akaganeite, and the (100) and (001) planes on lepidocrocite are the main surface planes for phosphate adsorption. These results are consistent with a tendency of the estimated phosphate adsorption capacities: akaganeite (2.88 anions/nm^2), goethite (2.54 anions/nm^2), and lepidocrocite (1.88 anions/nm^2) in a decreasing order. This study has indicated that although pH may affect protonation of the adsorbed phosphate molecule and binding sites

available, pH does not have a strong influence on the binding mode, i.e. a monodentate complex, bidentate complex, etc. There was no clear evidence of an iron phosphate precipitate formation on the surface, at least under the experimental adsorption conditions used in this study. We believe that the findings of this study, such as reactive planes and binding modes, will be useful in the design and improvement of iron oxyhydroxides as adsorbents for anionic molecules.

Chapter 5

Linking Local Environments and Hyperfine Shifts: A Combined Experimental and Theoretical ^{31}P, ^{2}H and ^{7}Li Solid–State NMR Study of Paramagnetic Fe(III) Phosphates and Pyrophosphates

Iron phosphates ($FePO_4$) have been established as amongst the most promising candidate for advanced battery cathode materials. The local structures of these materials, and associated properties such as bond covalency, have been shown to be important factors controlling electrochemical properties. Accordingly, this work reports a combined experimental and theoretical solid–state NMR study of the environments and electronic structures of a wide range of paramagnetic Fe(III) (pyro)phosphate compounds such as $FePO_4$ (heterosite), monoclinic $Li_3Fe_2(PO_4)_3$ (NASICON A-type), rhombohedral $Li_3Fe_2(PO_4)_3$ (NASICON B-type), $LiFeP_2O_7$, orthorhombic $FePO_4{\cdot}2H_2O$ (strengite), monoclinic $FePO_4{\cdot}2H_2O$ (phosphosiderite), and the dehydrated forms of the latter two phases. NMR techniques such as ^{31}P spin-echo mapping spectroscopy, and ^{2}H and ^{7}Li magic angle spinning (MAS) were applied to determine the magnitude of the various hyperfine shifts of the species of interest, along with periodic B3LYP hybrid density functional theory (DFT) calculations of the corresponding hyperfine tensors. It is anticipated that a similar combined approach may be fruitfully applied to characterize other paramagnetic iron phosphate compounds at a local level with solid-state NMR spectroscopy.

5.1 Introduction

Since olivine-type $LiFePO_4$ was proposed as a promising candidate for Li-ion batteries cathode materials,[114-116] various Fe(III) (pyro)phosphate compounds such as $FePO_4$, $LiFeP_2O_7$, etc. have been synthesized and characterized in regard to their structural and electrochemical properties.[106, 108, 117-122] We have an interest in Fe(III)PO_4 phases of this type as model compounds relating to the sequestration of phosphate ions via formation of a precipitate of Fe and phosphate ions[93, 96, 98, 102] and adsorption on the surfaces of environmentally important iron oxyhydroxides such as goethite and ferrihydrite.[1, 11, 89-92] The accumulation of data linking hyperfine shifts to P environments within such model phases should be of assistance in determining the sites and coordination modes with which phosphate ions bind on the oxyhydroxides.

Solid-state NMR spectroscopy is well–established as a unique tool for the provision of quantitative data relating to the local environments of NMR-active nuclei at the atomic level. However, there exist only a limited number of successful NMR studies of Fe(III) systems; a scarcity due in large part to the often substantial line broadenings and shifts of NMR signals observed in paramagnetic systems.[50, 58, 59] Moreover, the ^{31}P nucleus emerges as a particularly challenging species from which to obtain highly resolved NMR spectra.[44, 47, 123, 124]

The large shifts observed in typical inorganic paramagnetic systems may be straightforwardly ascribed to the Fermi contact (hyperfine) interaction between the unpaired electrons localized (to a greater–or–lesser degree) in the cation d– or f–orbitals and the s–orbital electrons of the ligand species under investigation. The latter restriction

comes from the fact that it is only the s–symmetry orbitals which may manifest any overlap with the nucleus. The Hamiltonian for the Fermi contact interaction can be found in equations [1.22] and [1.23] in Chapter 1.

In this work, we report upon a combined experimental and first principles theoretical ^{2}H, ^{7}Li, and ^{31}P NMR study of a range of Fe(III) (pyro)phosphate materials, namely, $FePO_4$ (heterosite), monoclinic $Li_3Fe_2(PO_4)_3$ (NASICON A-type), rhombohedral $Li_3Fe_2(PO_4)_3$ (NASICON B-type), $LiFeP_2O_7$, orthorhombic $FePO_4{\cdot}2H_2O$ (strengite), monoclinic $FePO_4{\cdot}2H_2O$ (phosphosiderite), and the dehydrated phases of the latter two materials. Our method combines two distinct, but complementary approaches. First, the acquired NMR spectra are analyzed in terms of simple crystallographic considerations, which seek to relate the disposition of the various Fe–O–X bonds (X = observed species) to the corresponding likely hyperfine shifts. Secondly, theoretical hyperfine shifts have also been obtained directly from periodic DFT (density functional theory) simulations using the CRYSTAL06 linear combinations of atomic orbitals code, with the aim of testing the experimental assignment of the spectra. We suggest that this combined approach should be readily applicable to other paramagnetic transition metal compounds.

We turn now to discuss the details of the structures studied. $FePO_4$ (heterosite, space group Pnma) may be classed as an olivine-type compound,[125] its crystal structure[8] (Figure 5.1 (a)) comprising FeO_6 octahedra and PO_4 tetrahedra linked such that each PO_4 tetrahedron shares a corner with four FeO_6 octahedra and an edge with one further FeO_6 unit.

The framework structure of rhombohedral $Li_3Fe_2(PO_4)_3$ (NASICON B–type; space group R-3), meanwhile, comprises exclusively corner–sharing FeO_6 octahedra and

PO_4 tetrahedra (Figure 5.1 (b)).[126] Here, the Fe ions are distributed over two crystallographically–distinct sublattices, while the Li and P ions each occupy a single sublattice, respectively. The P ions manifest four Fe ions in their first coordination shells, while each Li ion coordinates with three Fe sites in the first shell, where two of the Fe octahedra link to Li by corner–sharing, while the remaining Fe octahedron links to Li by edge-sharing.

Monoclinic $Li_3Fe_2(PO_4)_3$ (NASICON A–type; space group $P2_1/n$) is formed by heating rhombohedral $Li_3Fe_2(PO_4)_3$ to temperatures above 570 °C.[120] Again, its structure comprises corner–sharing FeO_6 octahedra and PO_4 tetrahedra (Figure 5.1 (c)) with the Fe ions distributed over two sublattices. Further to the rhombohedral B–type phase, however, the Li and P ions each occupy three distinct sublattices in this form.[120] The three P sites, denoted here as P1, P1s, and P2, link to four Fe ions via corner sharing of the respective PO_4 and FeO_6 units. The Li1 site is four–fold coordinated, linking to two neighboring FeO_6 units by edge–sharing, whereas the Li2 and Li3 sites are both five–fold coordinated.[120] However, Li2 manifests a Li-O bond of length 2.46 Å,[120] which is substantially longer than a typical Li-O distance of approximately 1.7 to 2.0 Å. Similarly, the Li3 site shows two substantially elongated Li-O bonds of lengths 2.37 and 2.44 Å.[120]

The crystal structure of $LiFeP_2O_7$ is monoclinic (space group $P2_1$), as shown in Figure 5.1 (d).[119] Here, the Fe and Li ions each occupy a single sublattice, while there are two symmetry–distinct P sublattices, denoted P1 and P2. Each FeO_6 octahedron connects with six P_2O_7 groups arranged in such a fashion that the P ions manifest three Fe ions in their first coordination shells: linking to two of the Fe ions by corner–sharing and to the third by edge–sharing. The Li ions, meanwhile, are located in the tunnels formed

by the FeO_6 octahedra and PO_4 tetrahedra, and feature four Fe ions in their first coordination shells.

Strengite and phosphosiderite possess the same chemical formula $FePO_4 \cdot 2H_2O$, forming in cells with orthorhombic (space group Pbca) and monoclinic (space group $P2_1$) symmetries, respectively (Figure 5.1 (e) and (f)).[127] The structures of both polymorphs consist of corner–sharing FeO_6 octahedra and PO_4 tetrahedra, where two of the corners of each FeO_6 octahedra host the O atoms associated with structural water molecules. The P ions each present with four Fe ions in their first coordination shells. Loss of structural water occurs when strengite is heated to 120 °C, and when phosphosiderite is dried at 80 °C under vacuum, leading to the formation of two dehydrated phases. The FeO_6 octahedra are transformed to tetrahedra by this process, but the respective space group symmetries of the two forms remain unchanged (Figure 5.1 (g) and (h)).[108] FeO_4 tetrahedra and PO_4 tetrahedra now link by corner-sharing. The P sites in the dehydrated $FePO_4$ phases present with four Fe ions in their first coordination shells.

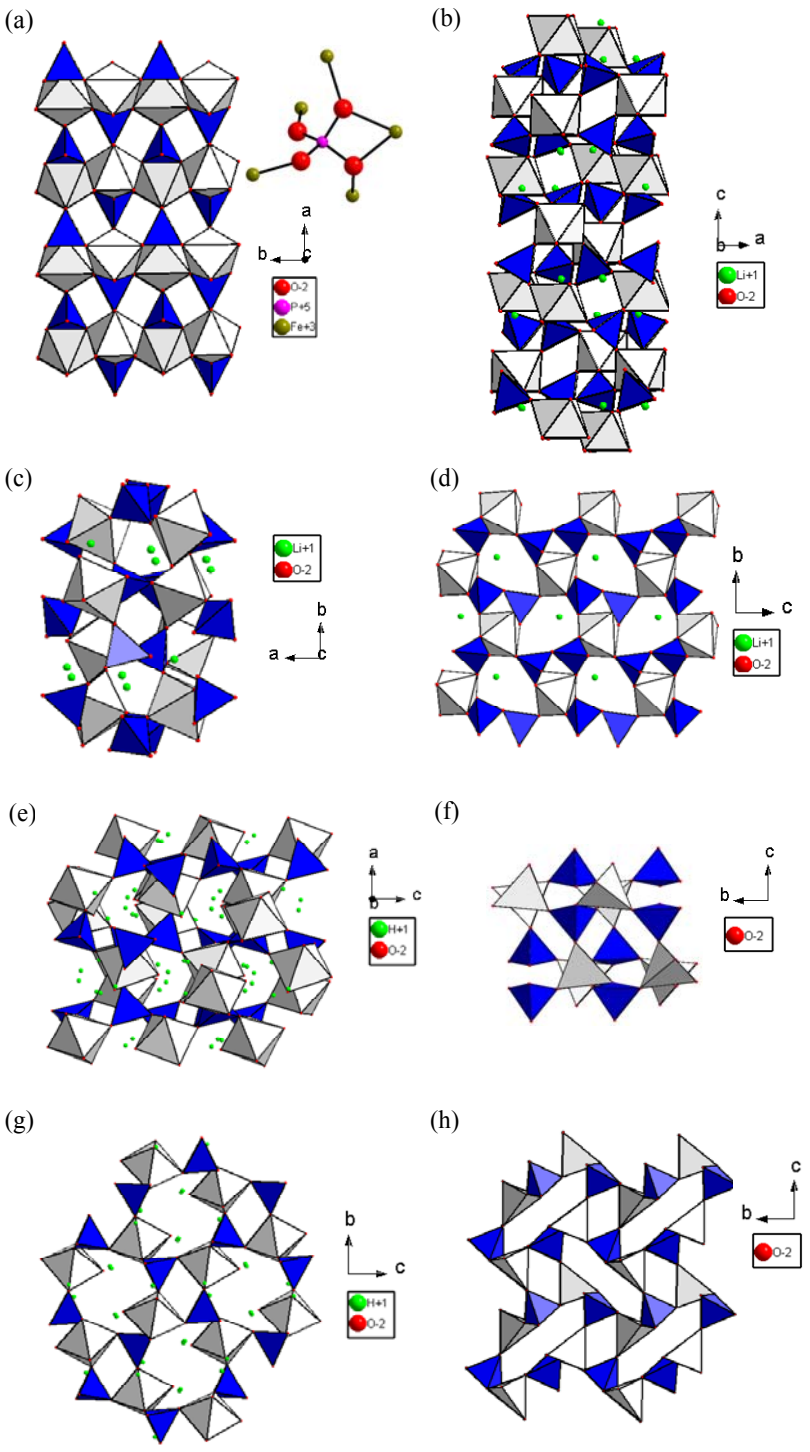

Figure 5.1. The crystal structures of (a) heterosite $FePO_4$, (b) rhombohedral $Li_3Fe_2(PO_4)_3$, (c) monoclinic $Li_3Fe_2(PO_4)_3$, (d) $LiFeP_2O_7$, (e) strengite, (f) dehydrated strengite, (g) phosphosiderite, and (h) dehydrated phosphosiderite. Inset in (a) shows the first-coordination shell of a phosphorus atom. These crystal structures were drawn with the reported crystallographic parameters.[106, 108, 119, 120, 126] Grey corresponds to FeO_6 octahedra and blue to PO_4 tetrahedra, respectively.

5.2 Experimental and Theoretical Section

5.2.1 Sample Preparation

Strengite (orthorhombic $FePO_4 \cdot 2H_2O$) was prepared by mixing 0.009 M $FeCl_3 \cdot 6H_2O$ and 0.027 M H_3PO_4 solutions under magnetic stirring.[117] The pH of the mixed solution was adjusted to 3 with 0.04 M NaOH solution, and the final solution refluxed for 2 days. A yellowish powder of strengite was obtained after centrifugation and drying at room temperature. A part of the formed strengite was dried for 12 hrs at 140 °C, leading to the formation of the dehydrated phase (DH strengite).[117]

Phosphosiderite (monoclinic $FePO_4 \cdot 2H_2O$) was synthesized by mixing 0.009 M $FeCl_3 \cdot 6H_2O$ and 0.027 M H_3PO_4 solutions, and then the adjusting pH to approximately 1 by addition of 0.5 M HCl solution.[117] The resulting solution was then refluxed for 12 days, and the solid product, phosphosiderite, separated from the mother liquor by centrifugation and then dried at room temperature. A part of the obtained phosphosiderite was dried at 80 °C for 12 hrs under vacuum to form the associated dehydrated phase (DH phosphosiderite).[108] Monoclinic and rhombohedral $Li_3Fe_2(PO_4)_3$ and $LiFeP_2O_7$ compounds were provided by the group of C. Masquelier.[107, 119, 121, 128]

5.2.2 Characterization

5.2.2.1 X-Ray Diffraction (XRD) and Magnetic Susceptibility Measurement

XRD data were collected for all samples on a Rigaku Miniflex XRD X-ray diffractometer (Cr Kα radiation). The measured XRD patterns were converted to the 2Θ values corresponding to Cu Kα radiation. The diffraction patterns of DH strengite and phosphosiderite samples were compared with the previously reported XRD patterns.[108, 117] All of the XRD patterns of strengite, phosphosiderite, monoclinic and rhombohedral Li3Fe2(PO4)3 compounds, and LiFeP2O7 were compared with the calculated XRD patterns on the basis of the structural refinements of these compounds. [119, 120, 126, 127] Magnetic properties of strengite and phosphosiderite were measured by using a Quantum Design SQUID magnetometer (MPMS XL-5) and Quantum Design Physical Properties Measurement System (PPMS). Field-cooled (FC) and zero-field-cooled (ZFC) susceptibilities were measured from 300 to 2 K in a magnetic field of 10 Oe.

5.2.2.2 Solid-state NMR

^{31}P spin-echo mapping experiments were performed on a CMX-200 spectrometer equipped with a 5mm Chemagnetics static probe. ^{31}P NMR spectra were referenced to a 1.0 M H_3PO_4 solution at 0 ppm. The NMR experiments used a spin-echo pulse sequence of the form $90°_x$-τ-$180°_y$-τ-acquire with an evolution period of 20 μs and a pulse width of 3.25 μs. The irradiation frequency was varied with a step size of 0.08 MHz. The spin-lattice relaxation (T_1) time was measured by use of an inversion-recovery pulse sequence. A pulse delay of 0.01 s was used, on the basis of the measured T_1 times (≈ 0.5 ms) of strengite; the T_1 times of the other compounds were assumed to be similar. The chemical shift anisotropy (CSA) interaction for the ^{31}P NMR spectrum of $LiFeP_2O_7$, the only

compound for which appreciable CSA was noted, was simulated by MATNMR module within MATLAB V.7.1[129] and an isotropic resonance was obtained. The ^{7}Li MAS (magic angle spinning) NMR experiments were performed at a Larmor frequency of 77.7 MHz on a CMX-200 spectrometer equipped with a Chemagnetics 3.2 mm HFX MAS probe. Spinning speeds in the range 17–20 kHz were used, adopting a 1.0 M LiCl solution at 0 ppm as a reference. A rotor-synchronized, spin-echo pulse sequence with a pulse delay of 0.15 s was used. The ^{2}H MAS NMR spectra were measured at a Larmor frequency of 55.3 MHz on an Infinity-360 spectrometer with a Chemagnetics 4 mm MAS probe at 15 kHz spinning speed. The spectra were referenced to D_2O at 4.8 ppm. A pulse delay of 0.15 s was used.

5.2.3 First Principles Calculations and Magnetic Model

All calculations were performed within the CRYSTAL06 linear combinations of atomic orbitals code.[130] Basis sets comprising contractions of Gaussian–type functions of the form 1s(3) 2s(1) 2p(1) for H; 1s(5) 2sp(1) 3sp(1) 3d(1) for Li; 1s(6) 2sp(3) 3sp(1) 3d(1) for O; 1s(8) 2sp(5) 3sp(2) 4sp(1) 3d(1) for P; and 1s(8) 2sp(6) 3sp(4) 4sp(1) 5sp(1) 3d(4) 4d(1) for Fe were employed, where the values in parentheses denote the number of Gaussian primitives comprising each contraction. The sets were obtained from the CRYSTAL online repository[131]: the Fe set having been used in a wide range of magnetic Fe compounds; the H, O and P sets, in a recent study of hexagonal hydroxyapatite $Ca_{10}(PO_4)_6(OH)_2$;[132] and the Li set, in LiOH[133]. The spin–polarized B3LYP hybrid exchange–correlation functional[134-136] was used throughout the present study, motivated

by its superior performance in reproducing the properties of a wide range of transition metal compounds.[137-140] Sufficient convergence in total energies and spin densities was obtained by use of Coulomb– and exchange integral series truncation thresholds of 10^{-7}, 10^{-7}, 10^{-7}, 10^{-7} and 10^{-14} and an 8×8×8 Monkhorst–Pack reciprocal space mesh, all as described in the code documentation.[130] Calculations were performed within both the fixed experimental (termed a single point energy, denoted SPE) and fully optimized (denoted OPT) structures. In the latter case, the optimizations were pursued until convergence tolerances of 10^{-7}, 0.0003 and 0.0012 A.U. for total energy, RMS force and RMS displacement, respectively, were simultaneously satisfied. Tolerances for maximum force and displacement components were set at 1.5 times the respective RMS values. All calculations assume a ferromagnetic spin distribution, as enforced by initial spin constraints on the cells consistent with five unpaired electrons per Fe(III) site. It should be noted, however, that the final total energies and spin and charge distributions are obtained in the absence of such constraints. The charge and spin distributions in the cells were further rationalized by the application of the Mulliken partitioning scheme to the converged wave functions.

The isotropic chemical shifts of the nuclei of interest are assumed to be dominated by the Fermi contact (FC) interaction, which, rewriting equations [1.22] and [1.23], is obtained in the form

$$\frac{H_{FC}}{h} = \frac{2}{3h}\mu_0\mu_B\mu_N g_e g_I \mathbf{I}\cdot\mathbf{S}_e\left|\psi^{\alpha-\beta}\left(\mathbf{R}_N\right)\right|^2 \qquad [5.\ 1]$$

where h denotes the Planck constant; μ_0, the vacuum permeability; μ_B, the Bohr magneton; μ_N, the nuclear magneton; g_e, the electron g–factor, here assumed equal to two; g_I, the isotope–specific nuclear g–factor; **I**, the vector associated with the nuclear spin quantum number, where a change in interaction energy ΔH_{FC} is associated with the condition $\Delta\mathbf{I} = \pm 1$ for the single quantum NMR experiments performed here; $\mathbf{S}_e$, the vector associated with the electron spin quantum number; and $|\psi^{\alpha-\beta}(\mathbf{R}_N)|^2$, the spin–unpaired electron density at the position $\mathbf{R}_N$ of the nucleus of interest. The corresponding isotropic shift (ppm) may then be obtained as $\delta_{iso} = 10^6\Delta H_{FC}\Phi/(h\nu_0)$, where ν_0 is the single quantum resonance frequency of the isotope of interest, and $\Phi = M_{para}/M_{sat}$ is an effective scaling factor relating the saturated ferromagnetic magnetization, M_{sat}, represented by the DFT calculations to the much weaker paramagnetic magnetization, M_{para}, relevant to the NMR experiments. Normally, Φ might be assumed equal to the Brillouin function, $B_J(\lambda)$, for a species characterized by a total angular momentum quantum number J

$$B_J(\lambda) = \frac{2J+1}{2J}\coth\left(\frac{2J+1}{2J}\lambda\right) - \frac{1}{2S}\coth\left(\frac{\lambda}{2J}\right) \qquad [5.\ 2]$$

where

$$\lambda = \frac{g_J\mu_B J B_0}{k_B(T-\Theta)} \qquad [5.\ 3]$$

and in which g_J denotes the Landé g–factor; B_0, the applied static magnetic induction; k_B, the Boltzmann constant; and Θ, the experimentally–determined Weiss constant for the compound considered. However, here we make a further approximation so as to simplify the task of accounting for the fact that the experimental effective moment and the formal spin–only moment represented by the DFT calculations typically differ. Noting that the quotient λ is typically much smaller than unity, we substitute the Maclaurin expansion for coth(x), obtaining $B_J(\lambda) \approx (J+1)\lambda/3J + O(\lambda^3)$. Retaining only the term linear in λ, the scaling factor is finally obtained as

$$\Phi\left(B_0, T, \Theta, S_{form}, \mu_{eff}\right) = \frac{B_0 \mu_{eff}^2}{3k_B g_e \mu_B S_{form}\left(T - \Theta\right)} \qquad [5.4]$$

where μ_{eff} is the experimental effective moment obtained (along with Θ) from variable temperature measurements of the paramagnetic susceptibility; and S_{form}, the formal spin borne by the Fe(III) cation, assumed equal to 5/2 throughout the present study. Thus, the method as outlined should rightly be regarded as semi–empirical, relying as it does upon the input of data from the experimental magnetic measurements. (The experimental values of μ_{eff} and Θ, used in the calculation can be found Table 5.2.) A final issue arises in relation to the Fermi contact interaction, this being the well–known difficulty in obtaining accurate spin densities at nuclear positions due to the limitations of the basis

sets applied.[141] Here, this difficulty is partly alleviated by the fact that the calculations consider a range of H, Li and P sites, which should permit for the assessment of the correlation of experimental and calculated shifts. Again, this does introduce a further degree of empiricism into the theoretical method, but this is consistent with the use of the experimental susceptibility data, and with the main purpose of the calculations, namely, to aid in the interpretation of the experimental spectra.

5.3 Results and Discussion

5.3.1 Powder X-ray Diffraction (XRD) and Magnetic Susceptibility Measurement

The XRD powder patterns of as-synthesized strengite, phosphosiderite, and their anhydrous phases are well matched with the previously reported data[108, 117] (Figure 5.2). $LiFeP_2O_7$, monoclinic $Li_3Fe_2(PO_4)_3$, and rhombohedral $Li_3Fe_2(PO_4)_3$ samples shows very similar XRD powder patterns to those calculated on the basis of the previously reported crystal structures of those compounds[119, 120, 126] (Figure 5.3).

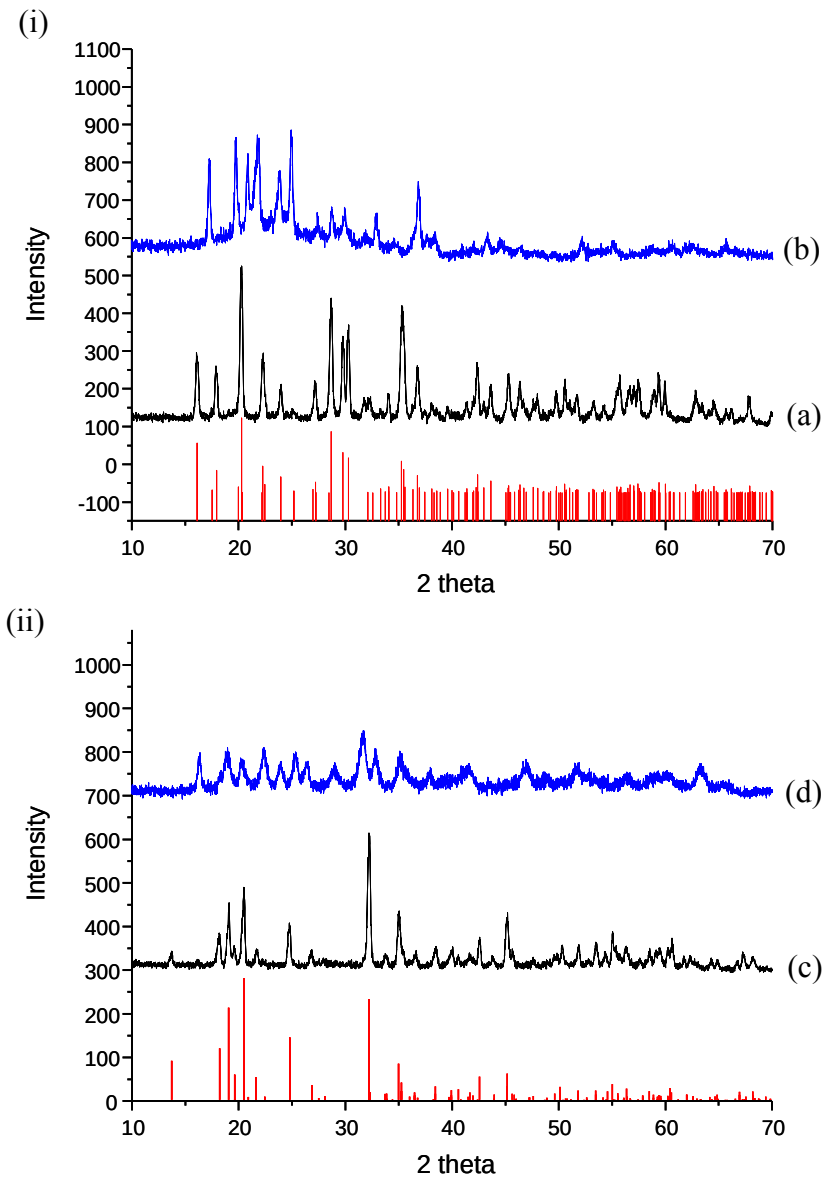

Figure 5.2. X-ray powder diffraction for (a) strengite, (b) DH strengite, (c) phosphosiderite, and (d) DH phosphosiderite. XRD patterns of the dehydrated phases were compared with the published data.[108, 117] Red vertical lines are calculated XRD patterns of strengite and phosphosiderite on the basis of the structural refinements of these materials.

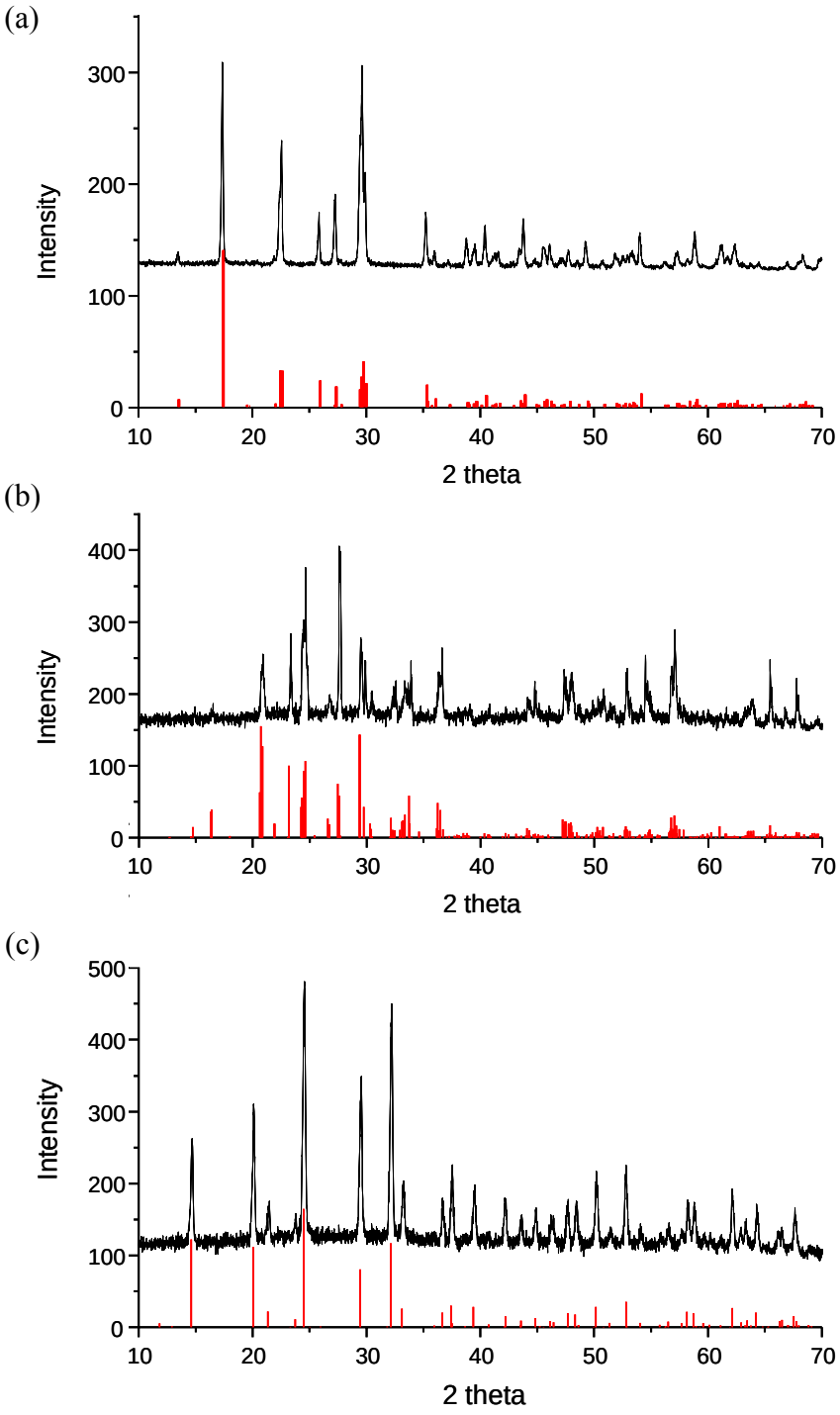

Figure 5.3. X-ray Powder diffraction for (a) $LiFeP_2O_7$, (b) monoclinic $Li_3Fe_2(PO_4)_3$, and (c) rhombohedral $Li_3Fe_2(PO_4)_3$. All of the XRD patterns were compared with the calculated XRD patterns used for the structural refinements of these compounds.[119, 120, 126]

The field–cooled and zero–field–cooled (FC-ZFC) susceptibility curves of strengite show a broad peak at approximately 6-7 K (Figure 5.4 (a)), indicating the onset of magnetic ordering. The FC curve of strengite indicates an increase of the magnetic susceptibility below the ordering temperature, which is typical for a weak ferrimagnetic material. Above this temperature, the susceptibility follows the Curie-Weiss law, a fit of the form $\chi = \chi^{o} + C/(T-\Theta)$, where C is the Curie constant, and Θ the Weiss constant, yielding μ_{eff} and Θ values of 5.86 μ_B and -42.3 K, respectively. Meanwhile, phosphosiderite shows a magnetic phase transition in the range 21-25 K (Figure 5.4 (b)), with fits of the Curie – Weiss susceptibility yielding μ_{eff} and Θ values of 5.64 μ_B and -45.8 K, respectively. Phosphosiderite also shows a weak ferrimagnetic ordering, with S-shaped susceptibility curves manifesting below the transition.

(a)

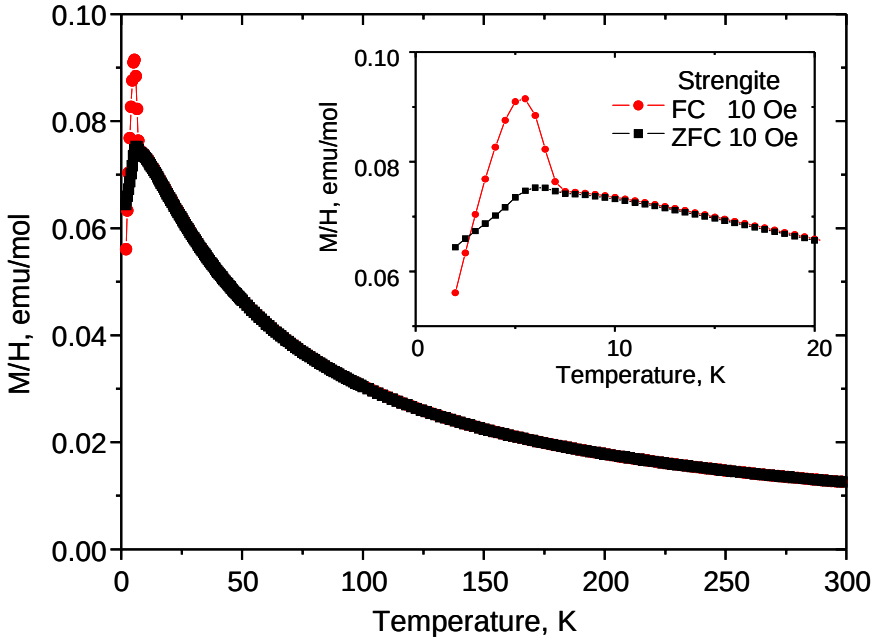

(b)

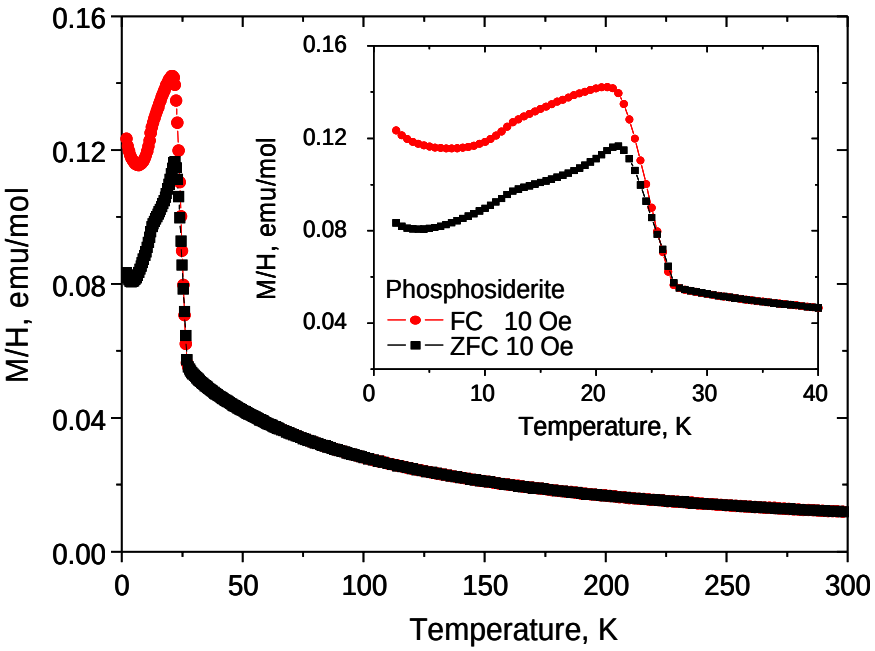

Figure 5.4. FC-ZFC magnetization curves of (a) strengite and (b) phosphosiderite at 10 Oe.

5.3.2 Solid-State NMR

5.3.2.1 ^{31}P Static Spin-echo Mapping NMR of Iron (Pyro)Phosphates

In this work, the Fe(III) (pyro)phosphates show unexpectedly large ^{31}P chemical shifts in the range 5700 to 20000 ppm and broad spectral widths some of which amount to more than 4000 ppm in the static solid-state NMR spectra (Figures 5.5 and 5.6). The large shifts are ascribed to the Fermi contact shift interaction discussed above, the typical diamagnetic chemical shift typically being reported in the region of 0 ppm. The broad line widths are attributed to the dipolar coupling between the unpaired electron density and the ^{31}P nuclei.

Heterosite $FePO_4$ shows an isotropic peak at 5770 ppm, further details on the NMR of this and related compounds to be published elsewhere.[105] A peak with a peak maximum at 14350 ppm is observed for rhombohedral $Li_3Fe_2(PO_4)_3$ (Figure 5.5 (a)), while strengite and DH strengite provide peaks at 15800 and 20426 ppm, respectively (Figures 5.5 (b) and (c)); phosphosiderite and DH phosphosiderite, at 16680 and 19149 ppm, respectively (Figures 5.5 (d) and (e)). Each of these six compounds manifests only one symmetry unique P site in their crystal structures, as discussed above.[106, 108, 126] The number of observed ^{31}P NMR resonances agrees with the results of this crystallographic analysis. The magnitude of the observed hyperfine shifts of those compounds increase in an order, heterosite, rhombohedral $Li_3Fe_2(PO_4)_3$, strengite, phosphosiderite, DH phosphosiderite, and DH strengite. Heterosite has the smallest average Fe-O-P bond among them due to the presence of a two Fe-O-P bond with a bond angle of 96° due to the linkages of Fe and P by edge-sharing. It has the largest average Fe-O bond distance

and the smallest value of effective magnetic moment (5.05 μ_B) (Table 5.1 and 5.2). Therefore, it is predictable that heterosite shows the smallest hyperfine shift among them. However, it is difficult to predict an ordering of the shift magnitudes of the remaining compounds by considering only a single factors, e.g. average Fe-O-P bond angles, Fe-O and O-P bond distances, and effective magnetic moments (μ_{eff}). For this reason, it is necessary to quantitatively investigate the contribution of each factor, e.g. bond angle and distance and magnetic moment, to the magnitude of the hyperfine shift. The hyperfine shifts obtained from calculations within the fixed experimental structures (SPE) amount to 4275, 12388, 12926, 19137, 13696, and 20931 for heterosite $FePO_4$, rhombohedral $Li_3Fe_2(PO_4)_3$, strengite, DH strengite, phosphosiderite, and DH phosphosiderite, respectively. The shifts obtained with the optimized structures (OPT), meanwhile, amount to 5280, 12257, 13621, 19166, 12281, and 19564 ppm, respectively. It is clear that both sets of values reproduce the broad range (approximately 14700 ppm) of experimental shifts, the SPE and OPT data ranging over approximately 16700 and 14300 ppm, respectively. Moreover, the experimental ordering of the shift magnitudes is represented faithfully by the SPE calculations, whereas the OPT calculations reverse the order of the strengite and phosphosiderite values.

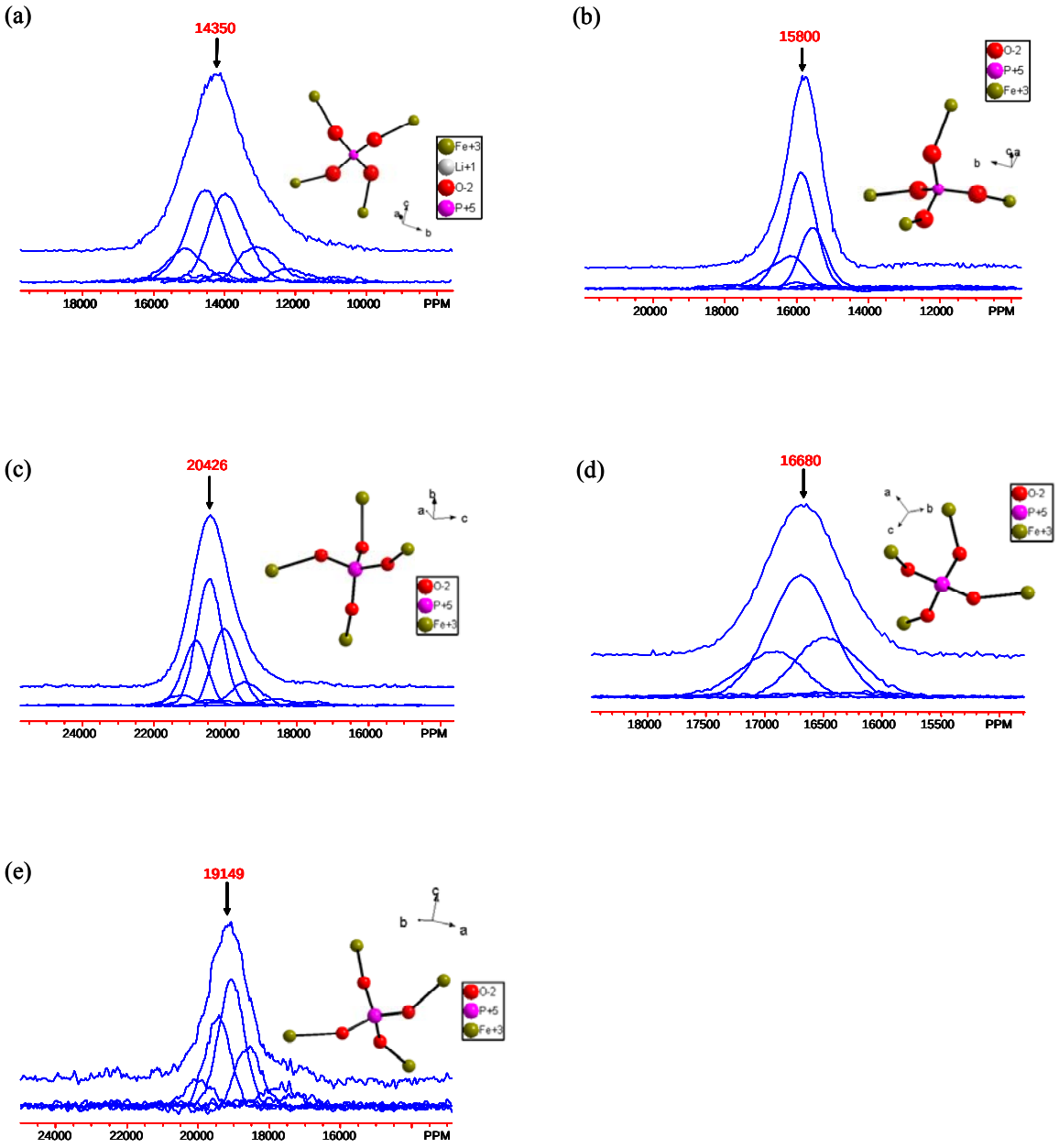

Figure 5.5. Spin echo mapping ^{31}P NMR spectra of (a) rhombohedral $Li_3Fe_2(PO_4)_3$, (b) strengite and (c) DH strengite and (d) phosphosiderite and (e) DH phosphosiderite. Inset on the right side: the local structure of a phosphorus atom.

	avg. Fe-O-P (°)	avg. Fe-O (Å)	avg. O-P (Å)
Heterosite	119.36	2.017	1.533
rhombohedral $Li_3Fe_2(PO_4)_3$	143.24	2.006	1.535
strengite	139.02	1.968	1.535
phosphosiderite	144.40	1.956	1.528
DH phosphosiderite,	148.80	1.886	1.531
DH strengite	138.69	1.854	1.534

Table 5.1. Summary of the average Fe-O-P bond angles and Fe-O and O-P bond distances taken from the reported crystallographic structures.[108, 126, 127]

Three peaks are observed with a peak maximum at 14230, 15250, and 16200 ppm for monoclinic $Li_3Fe_2(PO_4)_3$ (Figure 5.6 (a)), in correspondence with the number of symmetry–inequivalent P sublattices in this compound, as discussed earlier (Figure 5.6 (a)).[120] Of these sublattices, the P2 site possesses the shortest average Fe–O and O–P bond distances, amounting to 1.97 and 1.53 Å, respectively.[120] The P1s site, meanwhile, manifests an average Fe–O bond distance of 2.04 Å; substantially longer than the value 2.01 Å obtained for the P1 site,[120] both sites presenting a similar average O-P bond distance of 1.53 Å.[120] On the basis of this structural analysis, the peaks at 14230, 15250, and 16200 ppm are assigned to P1s, P1, and P2, respectively. The SPE calculation, meanwhile, provides predicted isotropic peaks at 13023, 13580, and 14424 ppm for P1s, P1, and P2, respectively, while the OPT calculation yields 13260, 13519, and 14111 ppm

peaks, respectively. The experimental δ(P1s)–δ(P1) and δ(P1)–δ(P2) peak separations of approximately 1000 ppm each are relatively poorly reproduced by the calculations: the SPE values yielding approximately 557 and 844 ppm, respectively; and the OPT values, 259 and 592, respectively.

Two peaks with a peak maximum at 8500 and 14934 ppm are observed for the $LiFeP_2O_7$ compound. Here, the reported structure yields longer average Fe–O and similar average P–O bond distances at the P2 site as compared with those at the P1 site: the former presenting average Fe–O and P–O bond distances of 2.02 and 1.51 Å, respectively; the latter, 1.96 and 1.51 Å, respectively.[119] On the basis of the bond distances above, the P2 site is expected to show a smaller hyperfine shift than the P1 site. Therefore, the P1 site is assigned to the peak at 14934 ppm, and the P2 site, to the peak at 8500 ppm. Both sets of calculated values support this assignment: the SPE calculation yielding predicted shifts of 12629 and 7378 ppm for P1 and P2 sites, respectively; and the OPT calculations, 12929 and 6968 ppm, respectively.

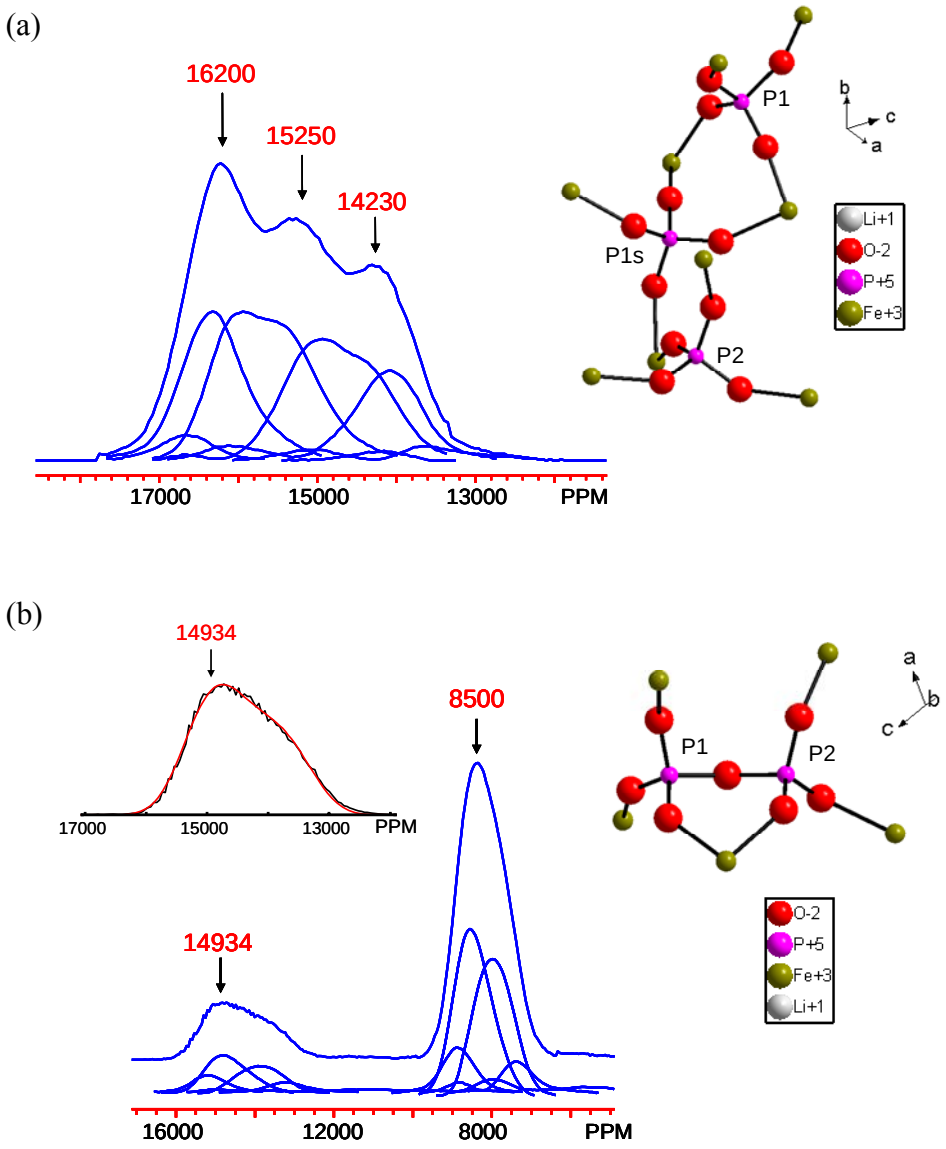

Figure 5.6. Spin echo mapping ^{31}P NMR spectra of (a) monoclinic $Li_3Fe_2(PO_4)_3$ and (b) $LiFeP_2O_7$. Inset on the right side: the local structure of a phosphorus atom. The inset at the left corner in (b): an isotropic resonance was labeled, which was estimated by a CSA pattern simulation.

Finally, it remains to discuss the general quality of the correlations obtained between the experimental and calculated shifts. Comparisons of the data yield root mean square errors (RMSEs) in the calculated values of 1951 and 2021 ppm with SPE and OPT structures, respectively, the theoretical values underestimating experiment in all cases

save for DH phosposiderite. The RMSE values serve to establish a crude measure of confidence in the theoretical data, in that sites characterized by hyperfine shifts the separations of which are less than the RMSE might be incorrectly identified. Figures 5.7 (a) and (b) show plots of the theoretical–vs–experimental data obtained with the SPE and OPT structures, respectively. Here, clear correlations are evident, as supported by computed Pearson correlation coefficients of 0.962 and 0.959, respectively. Table 5.2 also presents the Fe and P site unpaired electron counts obtained from Mulliken analyses of the final OPT wave functions. It is noted that the Fe moments are all of the same approximate magnitude, varying over a relatively narrow range from 4.209 to 4.319 unpaired electrons, lending support to the idea that a generally similar Fe(III) state persists across the range of compounds studied. There is no apparent correlation, however, between the experimental μ_{eff} and theoretical $n^{\alpha-\beta}$(Fe) values, in keeping with the understanding that the deviations of μ_{eff} from the formal value 5.92 μ_B anticipated for Fe(III) are likely due to the existence of some fraction of unquenched orbital angular momentum, and that the latter is not included in the present theoretical formalism. The $n^{\alpha-\beta}$(P) values, meanwhile, track the computed shifts in an acceptable fashion, which offers up the possibility, for related theoretical methods in which the spin densities at nuclear positions are not readily available, of estimating the P hyperfine shifts directly from the integrated P spin densities.

	Heterosite[106]	Rhombohedral $Li_3Fe_2(PO_4)_3$[107]	Monoclinic $Li_3Fe_2(PO_4)_3$[107]	$LiFeP_2O_7$[109]	Strengite	Phosphosiderite	DH Strengite[108]	DH Phosphosiderite[108]
Experimental susceptibility data:								
μ_{eff} (μ_B)	5.05[a]	5.77	5.89	5.89	5.86	5.74	6.31	6.39
Θ (K)	-125[b]	-50	-55	-73	-42.3	-45.8	-120.1	-179.8
Total Mulliken unpaired electron populations (B3LYP, optimized cells)[c]:								
$n^{\alpha-\beta}$(Fe)	4.279	4.294, 4.319	4.289, 4.296	4.315	4.306	4.315	4.209	4.248
$n^{\alpha-\beta}$(P)	0.017	0.020	all 0.020	0.022, 0.016	0.022	0.021	0.029	0.029
Relative energies of polymorphic forms (B3LYP, optimized cells):								
E_{rel} (kJ/mol)	0[d]	+11.4[e]	0[e]	—	0[f]	+1.1[f]	+8.1[d]	+4.9[d]

Table 5.2. Summary of the experimental effective magnetic moments, μ_{eff} (μ_B), and Weiss constants, Θ (K), used in the calculations, and of the Fe and P site total unpaired electron populations and relative static energies of polymorphic forms obtained from the B3LYP structural optimizations.

[a]μ_{eff} quoted by Rousse *et al.*[8] as 4.15 μ_B, but, within context of their study, this apparently relates to the unpaired electron count at Fe(III) sites. Value used here obtained assuming 4.15 unpaired electrons at Fe sites.

[b]Θ unknown for $FePO_4$. The Neél temperature has been substituted as a best approximation.

[c]Li and H unpaired electron populations too small to be accurately extracted from Mulliken analyses.

[d]$FePO_4$ polymorphs, [e]$Li_3Fe_2(PO_4)_3$ polymorphs, [f]$FePO_4 \cdot 2H_2O$ polymorphs.

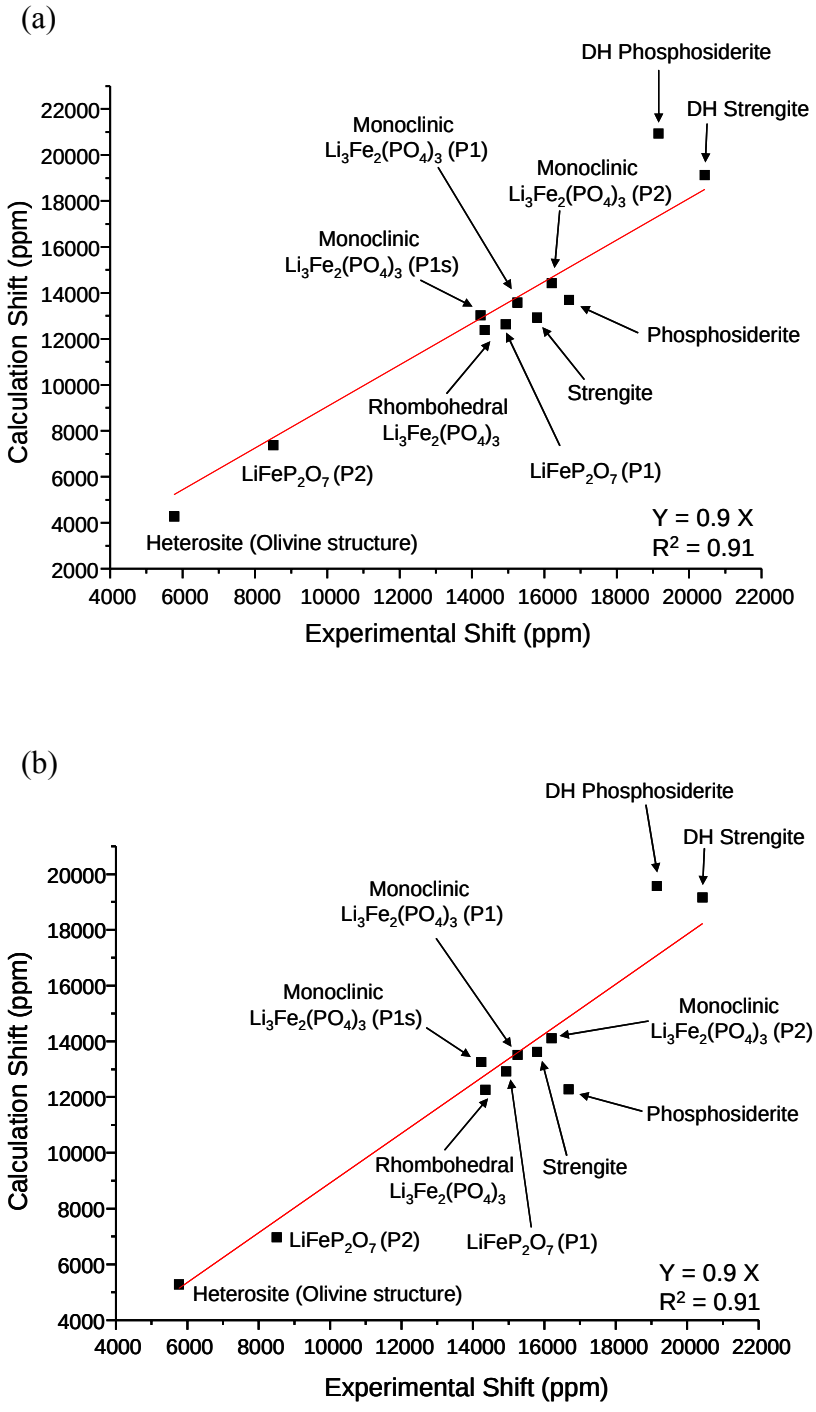

Figure 5.7. The correlation of the experimental hyperfine shifts of iron (pyro)phosphates with the calculated shifts based on the (a) experimental and (b) the optimized structures in ^{31}P solid-state NMR spectra. ('dehydrated' is abbreviated as DH.)

5.3.2.2 ^{7}Li MAS NMR of Monoclinic and Rhombohedral $Li_3Fe_2(PO_4)_3$ and $LiFeP_2O_7$

The $LiFeP_2O_7$ and rhombohedral $Li_3Fe_2(PO_4)_3$ compounds manifest a single crystallographic site of a Li atom in their framework structures,[126, 128] leading to the expectation of a single isotropic resonance in their solid-state ^{7}Li MAS NMR spectra. Here, the isotropic peaks are positioned at 162 and 164 ppm, respectively (Figures 5.8 (a) and (b)). By comparing the hyperfine shifts of these two compounds, it is suggest that Fe-O-Li bond angle is also an important factor to contribute the magnitude of the hyperfine shifts. $LiFeP_2O_7$ has shorter average Fe-O and Li-O bond distances of 2.01 and 2.02 Å, respectively, than those of rhombohedral $Li_3Fe_2(PO_4)_3$, 2.02 and 2.03 Å, respectively. Furthermore, $LiFeP_2O_7$ has a larger magnetic moment of 5.89 μB than that of rhombohedral $Li_3Fe_2(PO_4)_3$ (5.77 μB). However, rhombohedral $Li_3Fe_2(PO_4)_3$ shows the larger hyperfine shift than $LiFeP_2O_7$. It can be explained by larger Fe-O-Li bond angle of rhombohedral $Li_3Fe_2(PO_4)_3$ than that of $LiFeP_2O_7$, i.e. 100.72° vs. 97.61°.

Meanwhile, for monoclinic $Li_3Fe_2(PO_4)_3$, within which there are three symmetry–inequivalent Li sublattices,[120] the isotropic resonances occur at 40, 90, and 190 ppm (Figure 5.8 (c)). Here, the Li1 and Li2 sites present with four Li-O-Fe bonds in their first coordination shells, and the Li3 site, three Li-O-Fe first coordinations, subject to the criterion that a substantive Li-O chemical bond should be shorter than 2.30 Å. Therefore, the peak at 40 ppm is assigned to the Li3 sites on the basis that it has the smallest number of Fe-O-Li interactions. The Li1 site, meanwhile, has averaged Li-O and Fe-O distances of 1.96 and 2.04 Å, respectively; and the Li2 site, 2.00 and 2.08 Å, respectively.[120] On this basis, the Li1 and Li2 sites are assigned to the peaks at 190 and 90 ppm, respectively.

The SPE calculations for $LiFeP_2O_7$ and rhombohedral $Li_3Fe_2(PO_4)_3$ position the isotropic resonances at 206 and 221 ppm, respectively, while monoclinic $Li_3Fe_2(PO_4)_3$ shows three isotropic peaks at 260, 155, and 72 ppm for Li1, Li2, and Li3 sites, respectively. The OPT calculations provide values of 185 and 263 ppm for $LiFeP_2O_7$ and rhombohedral $Li_3Fe_2(PO_4)_3$, respectively, and values 262, 134, and 124 ppm for the Li1, Li2, and Li3 sites, respectively, of monoclinic $Li_3Fe_2(PO_4)_3$. Here, for the latter compound, the experimental δ(Li2)–δ(Li3) and δ(Li1)–δ(Li2) splittings of 50 and 100 ppm, respectively are reproduced relatively well by the SPE calculation, yielding values 83 and 105 ppm, respectively, and significantly more poorly by the OPT calculation, at 10 and 128 ppm, respectively. The RMSEs of the calculated values for all compounds amount to 55 and 70 ppm for the SPE and OPT data, respectively, both of which amount to large fractions of the experimental range spanning from 40 to 190 ppm. However, the Pearson coefficient of 0.985 obtained for the plot of the SPE calculated–vs–experimental data (Figure 5.9 (a)) does establish substantial correlation between these values, whereas the plot obtained using the OPT calculated data (Figure 5.9 (b)) shows significantly weaker correlation with a coefficient 0.890.

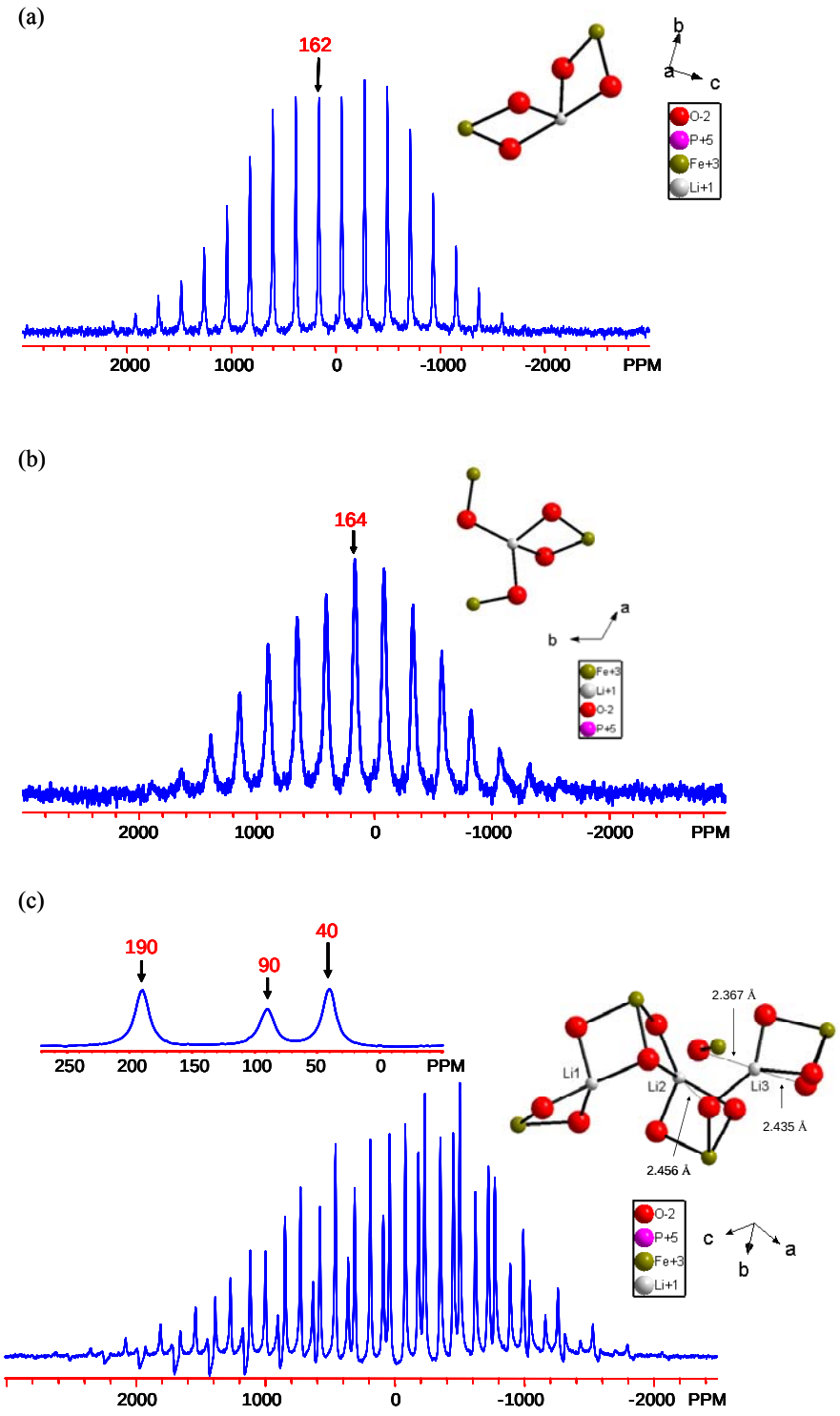

Figure 5.8. ^{7}Li MAS NMR spectra of (a) $LiFeP_2O_7$, (b) rhombohedral $Li_3Fe_2(PO_4)_3$, and (c) monoclinic $Li_3Fe_2(PO_4)_3$, at a Larmor frequency of 77.7 MHz. The isotropic resonances are labeled with their hyperfine shifts. MAS spinning speeds of 17, 21, and 19 kHz were used for measuring $LiFeP_2O_7$, monoclinic $Li_3Fe_2(PO_4)_3$, and rhombohedral $Li_3Fe_2(PO_4)_3$, respectively. Inset on the right side: the local structure of a lithium atom.

(a)

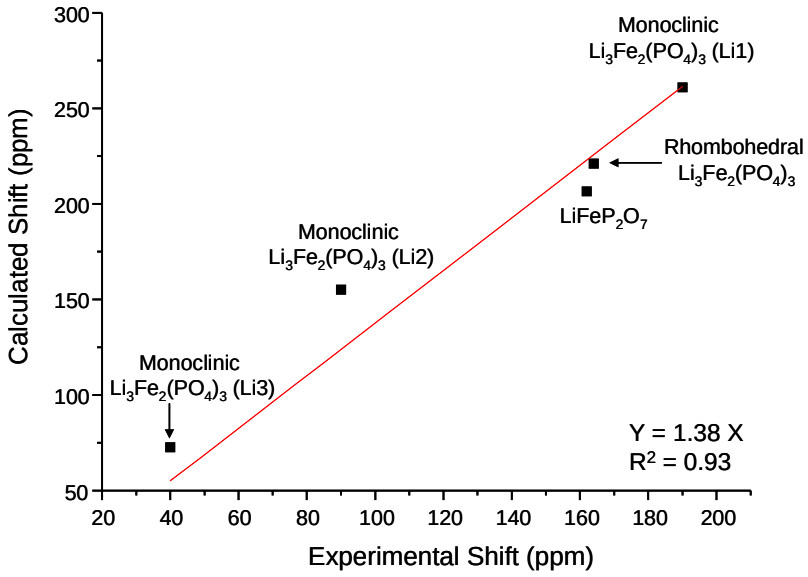

(b)

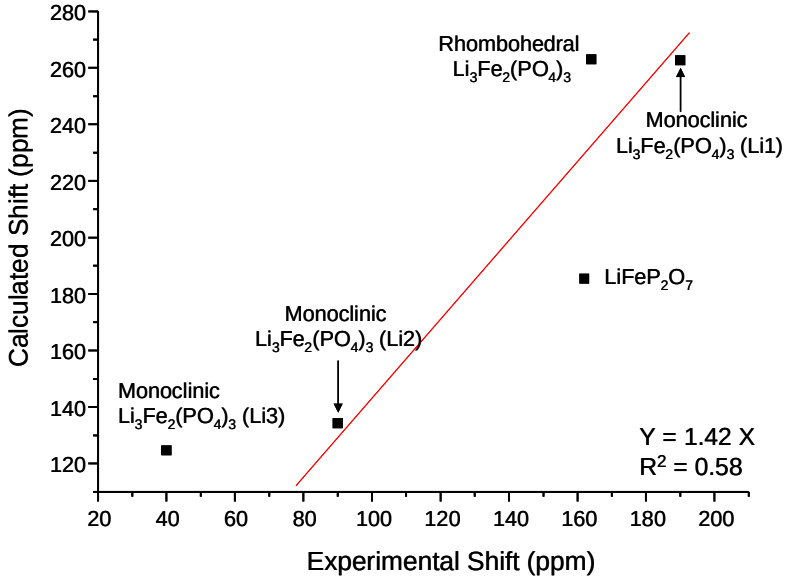

Figure 5.9. The correlation of the experimental hyperfine shifts of iron (pyro)phosphates with the calculated shifts based on the (a) experimental and (b) optimized structures in ^{7}Li MAS solid-state NMR spectra.

5.3.2.3 ^{2}H MAS NMR of Strengite and Phosphosiderite

Deuterated strengite provides five isotropic resonances at 66, 119, 133, 232, and 261 ppm (Figure 5.10 (a)). The line shape of the peak at 66 ppm is of the Pake doublet–type characteristic of rigidly bound hydroxyl (-OD) groups, supportive of the presence of a significant concentration of OD groups in the structure. The other peaks show line shapes characteristic of rotationally mobile $–OD_2$ groups, and are tentatively ascribed to the protons comprising the structural water molecules, H1-4. Four isotropic resonances at 139, 83, 33, and -53 ppm are predicted by SPE calculation for H1, H2, H3, and H4, respectively. OPT calculation shows 181, 194, 11, and -81 ppm for H1, H2, H3, and H4, respectively. These values are different from the observed hyperfine shifts. To interpret the ^{2}H spectrum, more investigations are necessary in terms of purity, more exact proton positions, etc. of the strengite sample.

Three isotropic resonances are observed at 6, 142, and 280 ppm in a ^{2}H MAS NMR spectrum of deuterated phosphosiderite (Figure 5.10 (b)). 6 ppm is assigned to surface water due to its small chemical shift. The large shifts of 142 and 280 ppm are ascribed to the hyperfine interactions and assigned to structural waters. The entire line shape of the 142 ppm resonance is characteristic of a rotational motion of $–OD_2$ groups, indicating that the 142 ppm is an averaged value of two hyperfine shifts of two protons by the motion. On the basis of this, the 142 ppm resonance is ascribed to the water involved with H2 and H4 atoms of the structural water, which has a longer Fe-O bond distance of 2.09 Å than that of the remaining structural water molecule (2.02 Å) (Figure 5.10 (b)).[127] Similarly, the isotropic resonance at 280 ppm was assigned to the other

water involved with H1 and H3 atoms of the other structural water due to the shorter O6-Fe bond distance. These protons have a shorter hydrogen bonding (1.81 Å) with oxygens (O2 and O3) in their first coordination shell than those of H2 and H4 (2.16 – 2.29 Å) (Figure 5.10 (b)).[127] That the envelope of the isotropic peak and its spinning side bands relatively closer to that of a rigidly bound OD group in comparison with that of 140 ppm resonance is attributed to the stronger hydrogen bonding. The theoretical calculation with SPE suggests four isotropic peaks at 593, 13, -0.3, and 188 ppm for H1, H2, H3, and H4, respectively, while the calculation with OPT shows shifts of 556, 223, 3, and 13 ppm for H1, H2, H3, and H4, respectively. If it is assumed, again, that the rotational motion averages chemical shifts of deuterium atoms of $-OD_2$ groups, two peaks at 13 and 188 ppm from SPE calculation will be averaged to be a peak at 100.5 ppm. Similarly, two peaks at -0.3 and 593 ppm in the calculation will become a peak at 296 ppm. Similarly, two averaged shifts of 118 and 280 ppm are predicted from OPT calculation, too. These values are close to the observed peaks at 142 and 280 ppm and consistent with our peak assignment.

SPE and OPT calculations showed the opposite trend of the hyperfine shifts for H2 and H4 atoms each other due to the inversed trend of O-H bond distances and Fe-O-H bond angles. O-H bond distance and Fe-O-H bond angle of H2 atom are modified from 0.863 Å and 115.58° to 0.981 Å and 122.01°, respectively. On the other hand, those of H4 atoms are optimized from 0.858 Å and 123.93° to 0.988 Å and 111.85°, respectively. Experimental coordinates of protons are appreciably different from the optimized coordinates of the protons due to the limit of powder X-ray technique to locate proton atoms in a crystal structure while Li and P coordinates in experimental are similar to

those of the optimized structures for the compounds studied here. Furthermore, it is suggested that a Fe-O-H bond angle closer to 180° and a shorter O-H bond increase the magnitude of a hyperfine shift.

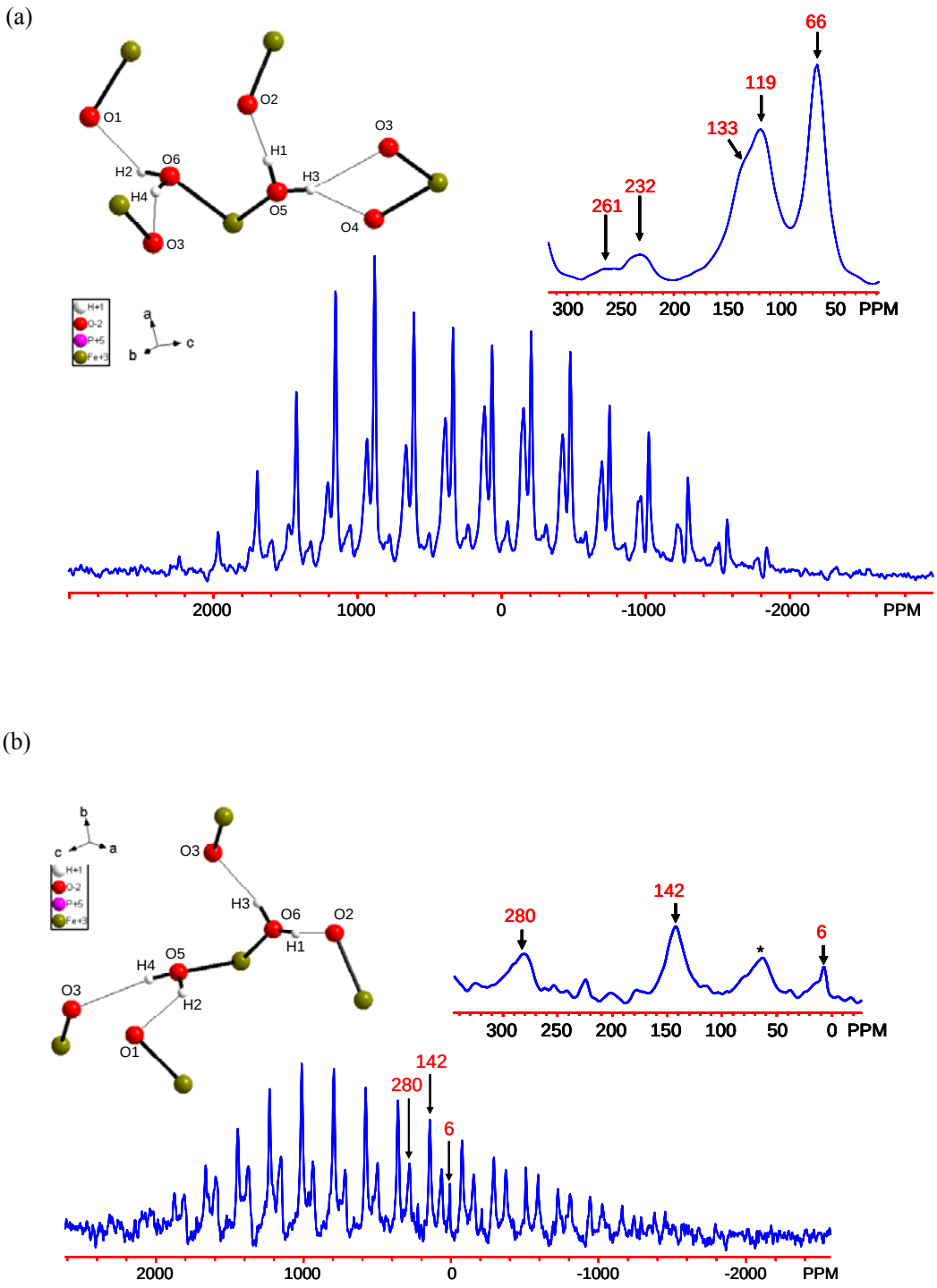

Figure 5.10. ^{2}H MAS NMR spectra of (a) strengite and (b) phosphosiderite at a Larmor frequency of 55.3 MHz. The isotropic resonances are labeled with their hyperfine shifts. MAS spinning speeds of 15 and 12 kHz were used for measuring strengite and phosphosiderite, respectively. The crystal cluster was drawn with the reported structural parameters.[127] (*) denotes a spinning side band. Inset on the left side: the local structure of a deuterium atom. Inset on the right side: a zoomed region of the full spectrum.

5.4 Conclusion

Several iron (pyro)phosphate compounds were investigated with ^{2}H, ^{7}Li, and ^{31}P solid-state NMR spectroscopy: $FePO_4$ (heterosite), monoclinic $Li_3Fe_2(PO_4)_3$ (Nasicon A-type compound), rhombohedral $Li_3Fe_2(PO_4)_3$ (Nasicon B-type compound), $LiFeP_2O_7$, orthorhombic $FePO_4 \cdot 2H_2O$ (strengite), monoclinic $FePO_4 \cdot 2H_2O$ (phosphosiderite), and dehydrated phases of strengite and phosphosiderite. Calculated hyperfine shifts of the observed nuclei of each compound were well correlated with the experimentally measured hyperfine shifts. The theoretical calculations supported the assignments of the observed NMR isotropic resonances to the corresponding crystallographic sites. In this contribution, a useful approaching method was demonstrated with a combination of solid-state NMR spectroscopy and theoretical calculation for characterizing the iron (pyro)phosphates. We believe that solid-state NMR spectroscopy can be applied to other complex paramagnetic systems to investigate their local environments in a similar method.

Bibliography

1. Cornell, R. M.; Schwertmann, U., *The Iron Oxides*. VCH: New York, 1996.

2. Huber, D. L., *Small* **2005,** *1*, 482-501.

3. Leland, J. K.; Bard, A. J., *J. Phys. Chem.* **1987,** *91*, 5076-5083.

4. White, A. F., *Reviews in Mineralogy 23*. Mineral Society of America: Washington, DC, 1990.

5. Amine, K.; Yasuda, H.; Yamachi, M., *J. Power Sources* **1999,** *81-82*, 221-223.

6. Matsumura, T.; Kanno, R.; Inaba, Y.; Kawamoto, Y.; Takano, M., *J. Electrochem. Soc.* **2002,** *149*, A1509-A1513.

7. Moon, J. W.; Roh, Y.; Lauf, R. J.; Vali, H.; Yeary, L. W.; Phelps, T. J., *Journal of Microbiological Methods* **2007,** *70*, 150-158.

8. Zhang, L.-Y.; Xue, D.-S.; Fen, J., *J. Magn. Magn. Mater* **2006,** *305*, 228-232.

9. Deliyanni, E. A.; Bakoyannakis, D. N.; Zouboulis, A. I.; Matis, K. A., *Chemosphere* **2003,** *50*, 155-163.

10. Deliyanni, E. A.; Matis, K. A., *Sep. Purif. Technol.* **2005,** *45*, 96-102.

11. Chitrakar, R.; Tezuka, S.; Sonoda, A.; Sakane, K.; Ooi, K.; Hirotsu, T., *J. Colloid Interface Sci.* **2006,** *298*, 602-608.

12. Lazaridis, N. K.; Bakoyannakis, D. N.; Deliyanni, E. A., *Chemosphere* **2005,** *58*, 65-73.

13. Deliyanni, E. A.; Peleka, E. N.; Matis, K. A., *J. Hazard. Mater.* **2007,** *141*, 176-184.

14. Ebner, A. D.; Ritter, J. A.; Navratil, J. D., *Ind. Eng. Chem. Res.* **2001,** *40*, 1615-1623.

15. Marmier, N.; Delisee, A.; Fromage, F., *J. Colloid Interface Sci.* **1999,** *211*, 54-60.

16. Yavuz, C. T.; Mayo, J. T.; Yu, W. W.; Prakash, A.; Falkner, J. C.; Yean, S.; Cong, L.; Shipley, H. J.; Kan, A.; Tomson, M.; Natelson, D.; Colvin, V. L., *Science* **2006,** *314*, 964-967.

17. Szytuta, A.; Burewicz, A.; Dimitrijevic, Z.; Krasnicki, S.; Rzany, H.; Todorovic, J.; Wanic, A.; Wolski, W., *Phys. Status Solidi* **1968,** *26*, 429-434.

18. Sakurai, Y.; Arai, H.; Okada, S.; Yamaki, J.-i., *J. Power Sources* **1997,** *68*, 711-715.

19. Kosmulski, M.; Durand-Vidal, S.; Maczka, E.; Rosenholm, J. B., *J. Colloid Interface Sci.* **2004,** *271*, 261-269.

20. Villalobos, M.; Perez-Gallegos, A., *Journal of Colloid and Interface Science* **2008,** *326*, 307-323.

21. Post, J. E.; Heaney, P. J.; Dreele, R. B. V.; Hanson, J. C., *Am. Mineral.* **2003,** *88*, 782-788.

22. Cai, J.; Liu, J.; Gao, Z.; Navrotsky, A.; Suib, S. L., *Chem. Mater.* **2001,** *13*, 4595-4602.

23. Stahl, K.; Nielsen, K.; Jiang, J.; Lebech, B.; Hanson, J. C.; Norby, P.; van Lanschot, J., *Corros. Sci.* **2003,** *45*, 2563-2575.

24. Post, J. E.; Buchwald, V. F., *Am. Mineral.* **1991,** *76*, 272-277.

25. Kubicki, J., *personal communication*.

26. Paterson, R.; Rahman, H., *J. Colloid Interface Sci.* **1983,** *94*, 60-69.

27. Samsonov, G., *The Oxide Handbook*. IFI/Plenum: New York, 1973.

28. Johnson, C. S.; Dees, D. W.; Mansuetto, M. F.; Thackeray, M. M.; Vissers, D. R.; Argyriou, D.; Loong, C.-K.; Christensen, L., *J. Power Sources* **1997,** *68*, 570-577.

29. Zhukhlistov, A. P., *Crystallography Reports* **2001,** *46*, 730-733.

30. Ishikawa, T.; Nitta, S.; Kondo, S., *J. Chem. Soc., Faraday Trans. 1* **1986,** *82*, 2401-2410.

31. Kanno, R.; Shirane, T.; Kawamoto, Y., *J. Electrochem. Soc.* **1996,** *143*, 2435-2442.

32. Hiemstra, T.; Riemsdijk, W. H. V., *J. Colloid Interface Sci.* **2000,** *225*, 94-104.

33. Hohl, H.; Stumm, W., *J. Colloid Interface Sci.* **1976,** *55*, 281-288.

34. Schindler, P. W.; Kamber, H. R., *Helv. Chim. Acta* **1968,** *51*, 1781-1786.

35. Stumm, W.; Huang, C. P.; Jenkins, S. R., *Croatica Chem. Acta* **1970,** *42*, 223-245.

36. Hiemstra, T.; van Riemsdijk, W. H., *J. Colloid Interface Sci.* **1996,** *179*, 488-508.

37. Hiemstra, T.; van Riemsdijk, W. H., *Langmuir* **1999,** *15*, 8045-8051.

38. Hiemstra, T.; van Riemsdijk, W. H.; Bolt, G. H., *J. Colloid Interface Sci.* **1989,** *133*, 91-104.

39. Venema, P.; Hiemstra, T.; Weidler, P. G.; van Riemsdijk, W. H., *J. Colloid Interface Sci.* **1998,** *198*, 282-295.

40. Grey, C. P.; Phillips, B., NMR Course. In *CEMS NMR Workshop*, Interaction, C. D. a. S. L. M. D. S. B. R. T. Q., Ed. Stony Brook, 2003.

41. Laws, D. D.; Bitter, H.-M. L.; Jerschow, A., *Angew. Chem. Int. Ed.* **2002,** *41*, 3096-3129.

42. Duer, M. J., *Introduction to Solid-State NMR Spectroscopy*. Blackwell: 2004.

43. Canesson, L.; Boudeville, Y.; Tuel, A., *J. Am. Chem. Soc.* **1997,** *119*, 10754-10762.

44. Canesson, L.; Tuel, A., *Chem. Commun.* **1997**, 241-242.

45. Sananes, M. T.; Tuel, A.; Volta, J. C., *J. Catal.* **1994,** *145*, 251-255.

46. Sananes, M. T.; Tuel, A.; Volta, J. C., *J. Catal.* **1994,** *148*, 395-398.

47. Mali, G.; Ristic, A.; Kaucic, V., *J. Phys. Chem. B* **2005,** *109*, 10711-10716.

48. Iggo, J. A., *NMR: Spectroscopy in Inorganic Chemistry*. Oxford Science Publications: 2004.

49. Poplett, I. J. F.; Smith, J. A. S., *J. Chem. Soc., Faraday Trans. 2* **1978,** *74*, 1077-1087.

50. Cole, K. E.; Paik, Y.; Reeder, R. J.; Schoonen, M.; Grey, C. P., *J. Phys. Chem. B* **2004,** *108*, 6938-6940.

51. Paik, Y.; Osegovic, J. P.; Wang, F.; Bowden, W.; Grey, C. P., *J. Am. Chem. Soc.* **2001,** *123*, 9367-9377.

52. Grey, C. P.; Dupre, N., *Chem. Rev.* **2004,** *104*, 4493-4512.

53. Carlier, D.; Menetrier, M.; Grey, C. P.; Delmas, C.; Ceder, G., *Phys. Rev. B* **2003,** *67*, 174103.

54. Cheetham, A. K.; Dobson, C. M.; Grey, C. P.; Jakeman, R. J. B., *Nature* **1987,** *328*, 706-707.

55. Grey, C. P.; Smith, M. E.; Cheetham, A. K.; Dobson, C. M.; Dupree, R., *J. Am. Chem. Soc.* **1990,** *112*, 4670-4675.

56. Grey, C. P.; Lee, Y. J., *Solid State Sci.* **2003,** *5*, 883-894.

57. Brough, A. R.; Grey, C. P.; Bobson, C. M., *J. Chem. Soc., Chem. Commun.* **1992**, 742-743.

58. Kim, J.; Nielsen, U. G.; Grey, C. P., *J. Am. Chem. Soc.* **2008,** *130*, 1285-1295.

59. Nielsen, U. G.; Paik, Y.; Julmis, K.; Schoonen, M. A. A.; Reeder, R. J.; Grey, C. P., *J. Phys. Chem. B* **2005,** *109*, 18310-18315.

60. Schwertmann, U.; Cornell, R. M., *Iron Oxides in the Laboratory*. VCH: New York: 1991.

61. Weckler, B.; Lutz, H. D., *Eur. J. Solid State Inorg. Chem.* **1998,** *35*, 531-544.

62. West, A. R., *Solid state chemistry and its applications.* . WSE Wiley: 1998.

63. Sudakar, C.; Subbanna, G. N.; Kutty, T. R. N., *J. Phys. Chem. Solids* **2003,** *64*, 2337-2349.

64. Gupta, S. K. Univ. Bern, 1976.

65. Waite, T. D.; Morel, F. M. M., *J. Colloid Interface Sci.* **1984,** *102*, 121-137.

66. Zhang, Y.; Charlet, L.; Schindler, P. W., *Colloids Surf.* **1992,** *63*, 259-268.

67. Gehring, A. U.; Hofmeister, A. M., *Clays Clay Miner.* **1994,** *42*, 409-415.

68. Lee, G. H.; Kim, S. H.; Choi, B. J.; Huh, S. H., *J. Korean Phys. Soc.* **2004,** *45*, 1019-1024.

69. Ozdemir, O.; Dunlop, D. J., *Geophys. Res. Lett.* **1996,** *23*, 921-924.

70. Alla, M.; Lippmaa, E., *Chem. Phys. Lett* **1982,** *87*, 30-33.

71. Kanno, R.; Shirane, T.; Inada, Y.; Kawamoto, Y., *J. Power Sources* **1997,** *68*, 145-152.

72. Pan, C., *SUNY Stony Brook* **2000**.

73. Randall, S. R.; Sherman, D. M.; Ragnarsdottir, K. V.; Collins, C. R., *Geochim. Cosmochim. Acta* **1999,** *63*, 2971-2987.

74. Sherman, D. M.; Randall, S. R., *Geochim. Cosmochim. Acta* **2003,** *67*, 4223-4230.

75. Peacock, C. L.; Sherman, D. M., *Geochim. Cosmochim. Acta* **2004,** *68*, 2623-2637.

76. Manceau, A.; Nagy, K. L.; Spadini, L.; Ragnarsdottir, K. V., *J. Colloid Interface Sci.* **2000,** *228*, 306-316.

77. Mazeina, L.; Deore, S.; Navrotsky, A., *Chem. Mater.* **2006,** *18*, 1830-1838.

78. Music, S.; Saric, A.; Popovic, S., *J. Mol. Struct.* **1997,** *410-411*, 153-156.

79. Richmond, W. R.; Cowley, J. M.; Parkinson, G. M.; Saunders, M., *CrystEngComm* **2006,** *8*, 36-40.

80. Kanungo, S. B., *J. Colloid Interface Sci.* **1994,** *162*, 86-92.

81. Yuan, Z.-Y.; Su, B.-L., *Chem. Phys. Lett.* **2003,** *381*, 710-714.

82. Barrero, C. A.; Garcia, K. E.; Morales, A. L.; Kodjikian, S.; Greneche, J. M., *J. Phys.: Condens. Matter* **2006,** *18*, 6827-6840.

83. Kulgawczuk, D. S.; Obuszko, Z.; Szytuza, A., *Phys. Status Solidi* **1968,** *26*, K83-K85.

84. Chambaere, D.; Grave, E. D., *J. Magn. Magn. Mater* **1983,** *42*, 263-268.

85. Fan, H.; Song, B.; Yang, Z.; Li, Q., *Chem. Lett.* **2004,** *33*, 576-577.

86. Zhou, Q.; Gibson, C. E.; Zhu, Y., *Chemosphere* **2001,** *42*, 221-225.

87. Vaithiyanathan, P.; Correll, D. L., *J. Environ. Qual.* **1992,** *21*, 280-288.

88. Daou, T. J.; Begin-Colin, S.; Greneche, J. M.; Thomas, F.; Derory, A.; Bernhardt, P.; Legare, P.; Pourroy, G., *Chem. Mater.* **2007,** *19*, 4494-4505.

89. Nowack, B.; Stone, A. T., *Water Res.* **2006,** *40*, 2201-2209.

90. Lin, S.-H.; Kao, H.-C.; Cheng, C.-H.; Juang, R.-S., *Colloids Surf., A* **2004,** *234*, 71-75.

91. Strauss, R.; Brummer, G. W.; Barrow, N. J., *Eur. J. Soil Sci.* **1997,** *48*, 101-114.

92. Deliyanni, E. A.; Peleka, E. N.; Lazaridis, N. K., *Sep. Purif. Technol.* **2007,** *52*, 478-486.

93. Persson, P.; Nilsson, N.; Sjoberg, S., *J. Colloid Interface Sci.* **1996,** *177*, 263-275.

94. Tejedor-Tejedor, M. I.; Anderson, M. A., *Langmuir* **1990,** *6*, 602-611.

95. Arai, Y.; Sparks, D. L., *J. Colloid Interface Sci.* **2001,** *241*, 317-326.

96. Luengo, C.; Brigante, M.; Antelo, J.; Avena, M., *J. Colloid Interface Sci.* **2006,** *300*, 511-518.

97. Antelo, J.; Avena, M.; Fiol, S.; Lopez, R.; Arce, F., *J. Colloid Interface Sci.* **2005,** *285*, 476-486.

98. Li, L.; Stanforth, R., *J. Colloid Interface Sci.* **2000,** *230*, 12-21.

99. Khare, N.; Hesterberg, D.; Martin, J. D., *Environ. Sci. Technol.* **2005,** *39*, 2152-2160.

100. Kwon, K. D.; Kubicki, J. D., *Langmuir* **2004,** *20*, 9249-9254.

101. Rahnemaie, R.; Hiemstra, T.; Riemsdijk, W. H. v., *Langmuir* **2007,** *23*, 3680-3689.

102. Ler, A.; Stanforth, R., *Environ. Sci. Technol.* **2003,** *37*, 2694-2700.

103. Forsyth, J. B.; Hedley, I. G.; Johnson, C. E., *J. Phys. C (Proc. Phys. Soc.)* **1968,** *1*, 179-188.

104. Kim, J.; Middlemiss, D. S.; Masquelier, C.; Grey, C. P., *To be submitted*.

105. Cabana, J.; Shirakawa, J.; Cheng, G.; Richardson, T. J.; Grey, C. P., *Submitted*.

106. Rousse, G.; Rodriguez-Carvajal, J.; Patoux, S.; Masquelier, C., *Chem. Mater.* **2003,** *15*, 4082-4090.

107. Rousse, G.; Rodriguez-Carvajal, J.; Wurm, C.; Masquelier, C., *Chem. Mater.* **2001,** *13*, 4527-4536.

108. Song, Y.; Zavalij, P. Y.; Suzuki, M.; Whittingham, M. S., *Inorg. Chem.* **2002,** *41*, 5778-5786.

109. Riou, D.; Nguyen, N.; Benloucif, R.; Raveau, B., *Mater. Res. Bull.* **1990,** *25*, 1363-1369.

110. Omoike, A.; Chorover, J.; Kwon, K. D.; Kubicki, J. D., *Langmuir* **2004,** *20*, 11108-11114.

111. Jing, C.; Meng, X.; Liu, S.; Baidas, S.; Patraju, R.; Christodoulatos, C.; Korfiatis, G. P., *J. Colloid Interface Sci.* **2005,** *290*, 14-21.

112. Randall, S. R.; Sherman, D. M.; Ragnarsdottir, K. V., *Geochim. Cosmochim. Acta* **2001,** *65*, 1015-1023.

113. Waychunas, G. A.; Davis, J. A.; Fuller, C. C., *Geochim. Cosmochim. Acta* **1995,** *59*, 3655-3661.

114. Anderson, A. S.; Thomas, J. O., *J. Power Sources* **2001,** *97-98*, 498-502.

115. Padhi, A. K.; Nanjundaswamy, K. S.; Goodenough, J. B., *J. Electrochem. Soc.* **1997,** *144*, 1188-1194.

116. Yamada, A.; Chung, S. C.; Hinokuma, K., *J. Electrochem. Soc.* **2001,** *148*, A224-A229.

117. Reale, R.; Scrosati, B.; Delacourt, C.; Wurm, C.; Morcrette, M.; Masquelier, C., *Chem. Mater.* **2003,** *15*, 5051-5058.

118. Wurm, C.; Morcrette, M.; Rousse, G.; Dupont, L.; Masquelier, C., *Chem. Mater.* **2002,** *14*, 2701-2710.

119. Rousse, G.; Rodriguez-Carvajal, J.; Wurm, C.; Masquelier, C., *Solid State Sci.* **2002,** *4*, 973-978.

120. Patoux, S.; Wurm, C.; Morcerette, M.; Rousse, G.; Masquelier, C., *J. Power Sources* **2003,** *119-121*, 278-284.

121. Masquelier, C.; Wurm, C.; Rodriguez-Carvajal, J.; Gaubicher, J.; Nazar, L., *Chem. Mater.* **2000,** *12*, 525-532.

122. Zaghib, K.; Julien, C. M., *J. Power Sources* **2005,** *142*, 279-284.

123. Sananes, M. T.; Tuel, A., *J. Chem. Soc., Chem. Commun.* **1995**, 1323-1324.

124. Wilcke, S. L.; Lee, Y.-J.; Cairns, E. J.; Reimer, J. A., *Appl. Magn. Reson.* **2007,** *32*, 547-563.

125. Yamada, A.; Takei, Y.; Koizumi, H.; Sonoyama, N.; Kanno, R., *Chem. Mater.* **2006,** *18*, 804-813.

126. Andersson, A. S.; Kalska, B.; Jonsson, P.; Haggstrom, L.; Nordblad, P.; Tellgren, R.; Thomas, J. O., *J. Mater. Chem.* **2000,** *10*, 2542-2547.

127. Taxer, K.; Bartl, H., *Cryst. Res. Technol.* **2004,** *39*, 1080-1088.

128. Rousse, G.; Rodriguez-Carvajal, J.; Wurm, C.; Masquelier, C., *Appl. Phys. A* **2002,** *74* (S704-S706).

129. van Beek, J. D., *J. Magn. Reson.* **2007,** *187* (1), 19-26.

130. Dovesi, R.; Saunders, V. R.; Roetti, C.; Orlando, R.; Zicovich-Wilson, C. M.; Pascale, F.; Civalleri, B.; Doll, K.; Harrison, N. M.; Bush, I. J.; D'Arco, P.; Llunell, M. CRYSTAL06; University of Torino, Torino, Italy: 2006.

131. http://www.crystal.unito.it.

132. Corno, M.; Busco, C.; Civalleri, B.; Ugliengo, P., *Phys. Chem. Chem. Phys.* **2006,** *8*, 2464-2472.

133. Merawa, M.; Labeguerie, P.; Ugliengo, P.; Doll, K.; Dovesi, R., *Chem. Phys. Lett.* **2004,** *387*, 453-459

134. Becke, A. D., *J. Chem. Phys.* **1993,** *98*, 5648-5652.

135. Lee, C.; Yang, W.; Parr, R. G., *Phys. Rev. B* **1988,** *37*, 785.

136. Miehlich, B.; Savin, A.; Stoll, H.; Preuss, H., *Chem. Phys. Lett.* **1989,** *157*, 200-206.

137. Corà, F.; Alfredsson, M.; Mallia, G.; Middlemiss, D. S.; Mackrodt, W. C.; Dovesi, R.; Orlando, R., *Struct. Bond.* **2004,** *113*, 171-232.

138. Mackrodt, W. C.; Middlemiss, D. S.; Owens, T. G., *Phys. Rev. B* **2004,** *69*, 115119

139. Middlemiss, D. S.; Wilson, C. C., *Phys. Rev. B* **2008,** *77*, 155129.

140. Muscat, J.; Wander, A.; Harrison, N. M., *Chem. Phys. Lett.* **2001,** *342*, 397-401.

141. Cohen, M. J.; Chong, D. P., *Chem. Phys. Lett.* **1995,** *234*, 405-412